ABSTRACT

Title of Document: DISCOVERY, CHARACTERIZATION AND MECHANISTIC STUDY OF A NOVEL L-TYROSINE HYDROXYLASE IN THE BIOSYNTHESIS OF ANTHRAMYCIN

Katherine Lindsey Connor
Doctor of Philosophy, 2012

Directed By: Adjunct Associate Professor Barbara Gerratana
Professor Steven Rokita
Department of Chemistry and Biochemistry

A tyrosine hydroxylase coded by *orf13* of the anthramycin biosynthesis gene cluster is proposed to catalyze the *ortho*-hydroxylation of L-tyrosine to L-DOPA as the initial step of a unique transformation to the hydropyrrole moiety found in anthramycin. The sequence of Orf13 is not similar to any known characterized proteins, nor does it contain conserved domains or motifs characteristic of enzymes performing aromatic hydroxylation. The lack of information for this common enzymatic reaction suggests the identification of a new class of tyrosine hydroxylases which may have novel cofactor requirements, novel folds and/or chemical mechanisms.

Heme B has been identified in purified Orf13 and full heme B occupancy is achieved during expression with iron (III) citrate in *E. coli*. Maximal L-tyrosine to L-DOPA conversion is observed in the presence of hydrogen peroxide (H_2O_2). This confirmed heme B as the required catalytic cofactor and the putative function of Orf13 as a tyrosine hydroxylase. This information also classified Orf13 as a heme peroxidase. Spectroscopic data from a reduced-CO (g) spectrum of Orf13 and electron paramagnetic

resonance of ferric-heme Orf13 are consistent with histidyl-ligated heme peroxidases. The steady-state kinetics of L-tyrosine hydroxylation show similar catalytic efficiency for L-tyrosine and H_2O_2. Orf13 has a secondary tyrosine hydroxylation activity in the presence of molecular oxygen (O_2) and dihydroxyfumaric acid (DHFA), which is also found with histidyl-heme peroxidases.

Orf13 is substrate specific and stereoselective for L-tyrosine. Turnover is only observed with *para*-substituted phenols but not with D-tyrosine, implicating the *para*-phenol substituent is required for hydroxylation. Although the catalytic requirements of heme B and H_2O_2 are in agreement with heme peroxidases, the resulting hydroxylated product (L-DOPA) by a H_2O_2 dependent pathway is unprecedented. Heme dependent aromatic hydroxylation is typically catalyzed by cytochrome P450s through an O_2 dependent pathway. Mechanistic investigation of Orf13 revealed H_2O_2 as the oxygen source in a labeling study using $H_2{}^{18}O_2$. A proposed mechanism of L-tyrosine hydroxylation is suggested to proceed through an oxygen rebound mechanism similar to cytochrome P450 aromatic hydroxylation. Therefore, Orf13 represents a new class of heme-histidyl ligated H_2O_2 dependent hydroxylases and is the first identified bacterial tyrosine hydroxylase.

DISCOVERY, CHARACTERIZATION AND MECHANISTIC STUDY OF A NOVEL L-TYROSINE HYDROXYLASE IN THE BIOSYNTHESIS OF ANTHRAMYCIN

By

Katherine Lindsey Connor

Dissertation submitted to the Faculty of the Graduate School of the
University of Maryland, College Park, in partial fulfillment
of the requirements for the degree of
Doctor of Philosophy
2012

Advisory Committee:
Associate Professor Doug Julin, Chair
Adjunct Associate Professor Barbara Gerratana, Co-chair
Professor Steven Rokita
Associate Professor Iqbal Hamza
Assistant Professor Nicole LaRonde-LeBlanc

Dedication

To my parents, Lee and Gary – achieving this dream would not have been possible without your love and support.

Acknowledgements

I would like to thank my advisor, Dr. Barbara Gerratana, for her guidance, support and commitment to hard work and excellence. Thank you for providing the atmosphere that allowed me to develop into a strong scientific researcher and professional. I would like to thank my co-advisor, Professor Steven Rokita, for his support, thoughtful discussions and special assistance with providing continuity at the later stages of my dissertation research. I would also like to thank my committee members, Professor Doug Julin, Professor Nicole LaRonde-LeBlanc and Professor Iqbal Hamza, for their valuable feedback and suggestions throughout the course of my graduate career at the University of Maryland.

Special thanks to Drs. Zvi Kelman, Yue Li and Yan Wang for their assistance with different instrumentations. A special thank you to - Dr. Squire J. Booker (Penn State University) for providing specialized training in anaerobic protein purification; Drs. David Goldberg, Amanda McGown and Charles Long (Johns Hopkins University) for their assistance with EPR measurements; Dr. Michael Marletta (The Scripps Research Institute) for his interest and useful discussions about characterizing heme dependent enzymes. I thank our collaborator, Dr. Keri Colabroy (Muhlenberg College) and her undergraduate student, Roxanne Shovelar, for their work with LmbB2, an Orf13 homolog, and our discussions for the characterization of this unique class of tyrosine hydroxylases.

I wish to thank the Gerratana and Rokita group members, past and present. Thank you for the encouragement, interesting discussions and many laughs along the way. Special thanks to Dr. Watchalee Chuenchor for being a wonderful friend and teaching me

the fun, delicious and spicy art of cooking Thai cuisine. Dr. Jorge Cham, thank you for your wit and insight into the academic world. And a special thanks to Stewart Smalley.

Saving the best for last, a very special thank you to my family and closest friends – "Thank you" merely scratches the surface. I am truly grateful for your constant, unconditional love and awe-inspiring support while I pursued this dream. Thank you for being on "Team Katie."

Table of Contents

List of Tables

Chapter 1

Chapter 2

None

Chapter 3

Chapter 4

Chapter 5

None

List of Figures

Chapter 1

Chapter 2

Chapter 3

Chapter 4

Chapter 5

List of Schemes

List of Abbreviations (in alphabetical order)

3-HPPA	3-(4-hydroxyphenyl) propanoic acid
α-KG	alpha-ketoglutarate
δ-ALA	delta-aminolevulinic acid
ϵ_{240}	extinction coefficient at 240 nm
ϵ_{275}	extinction coefficient at 275 nm
ϵ_{280}	extinction coefficient at 280 nm
ϵ_{290}	extinction coefficient at 290 nm
λ_{EM}	fluorescence emission wavelength
λ_{EX}	fluorescence excitation wavelength
A_{280}	absorbance at 280 nm
amu	atomic mass units
BH_4	tetrahydrobiopterin
CD	circular dichroism
CID	collision induced dissociation
CO	carbon monoxide
CV	column volume
DHFA	dihydroxyfumaric acid
DTT	dithiothreitol
EPR	electron paramagnetic resonance
ESI-FT-MS	electrospray ionization Fourier transformation mass spectrometry
ESI-MS	electrospray ionization mass spectrometry
FAD	flavin adenine dinucleotide
FLD	fluorescence detection
H_2O_2	hydrogen peroxide

Heme B	iron protoporphyrin IX
HPLC	high performance liquid chromatography
HRP	horseradish peroxidase
ICP-MS	inductively coupled plasma mass spectrometry
k_{cat}	macroscopic catalytic rate constant
k_{obs}	turnover rate under defined specific activity conditions
K_D	dissociation constant
kD	kilodalton
K_m	Michaelis-Menten constant
LB	Luria Bertani
MALDI-TOF-MS	matrix-assisted laser desorption ionization mass spectrometry
MMO	monophenol monooxygenase
MPO	myeloperoxidase
MS/MS	tandem mass spectrometry
MWCO	molecular weight cut-off
NADPH	nicotinamide adenine dinucleotide phosphate
Ni-NTA	nickel-nitriloacetic acid
NP	natural product
OD_{600}	optical density at 600 nm
PBD	pyrrolo[1,4]benzodiazepine
PCR	polymerase chain reaction
PMSF	phenylmethanesulfonyl fluoride
PPIX	protoporphyrin IX
RZ	Reinheitszahl
SDS-PAGE	sodium dodecyl sulfate-polyacrylamide gel electrophoresis

SOD	superoxide dismutase
SUMO	small ubiquitin modifier
T_R	retention time
Tyr	tyrosine
WT	wild type

Chapter 1: Introduction to the discovery and proposed function of Orf13 as an L-tyrosine hydroxylase

1.1 Pyrrolo[1,4]benzodiazepines (PBDs) are natural products of pharmaceutical interest

The worldwide leading cause of death is cancer, accounting for 7.6 million deaths in 2008 (*1*). Nearly half of the currently approved drugs to treat cancer are natural products (NPs), such as taxol (generic name: paclitaxel), or have been derived from NPs (*2*). The discovery and development of new chemotherapies to treat cancer rely heavily on NP drug discovery, owing to the extraordinary chemical diversity and biological activities of NPs (*2*). However, fundamental challenges precluding the clinical use of NPs as potential chemotherapeutic agents include compound availability, target selectivity and specificity, and chemical potency relative to undesirable side effects and toxicity. Additionally, chemical synthesis of NPs or NP analogues is not always feasible with current synthetic methodologies due to chemically labile groups, achieving correct stereochemistry and/or the overall complexity of the compound itself. Alternative approaches to overcome these challenges in order to develop effective chemotherapeutic agents are available through biosynthetic engineering and mutasynthetic strategies with the identification of NP biosynthetic gene clusters.

A class of natural products of chemotherapeutic interest is the pyrrolo[1,4]benzodiazepines (PBDs). Produced by actinomyces as secondary metabolites, PBDs display anti-cancer biological activity through inhibition of transcription and replication processes by sequence selective alkylation of DNA (*3*). Since the discovery of

anthramycin in 1963 (*4*) (Figure 1-1A), 18 other naturally produced PBDs have been isolated and characterized, and more than 60 synthetic PBDs have been made (*3, 5*). A synthetic PBD noteworthy of mention is SJG-136 (Figure 1-1B). This PBD dimer has remarkable anti-cancer biological activity and is currently in Phase II trials for the treatment of ovarian cancer (*5, 6*).

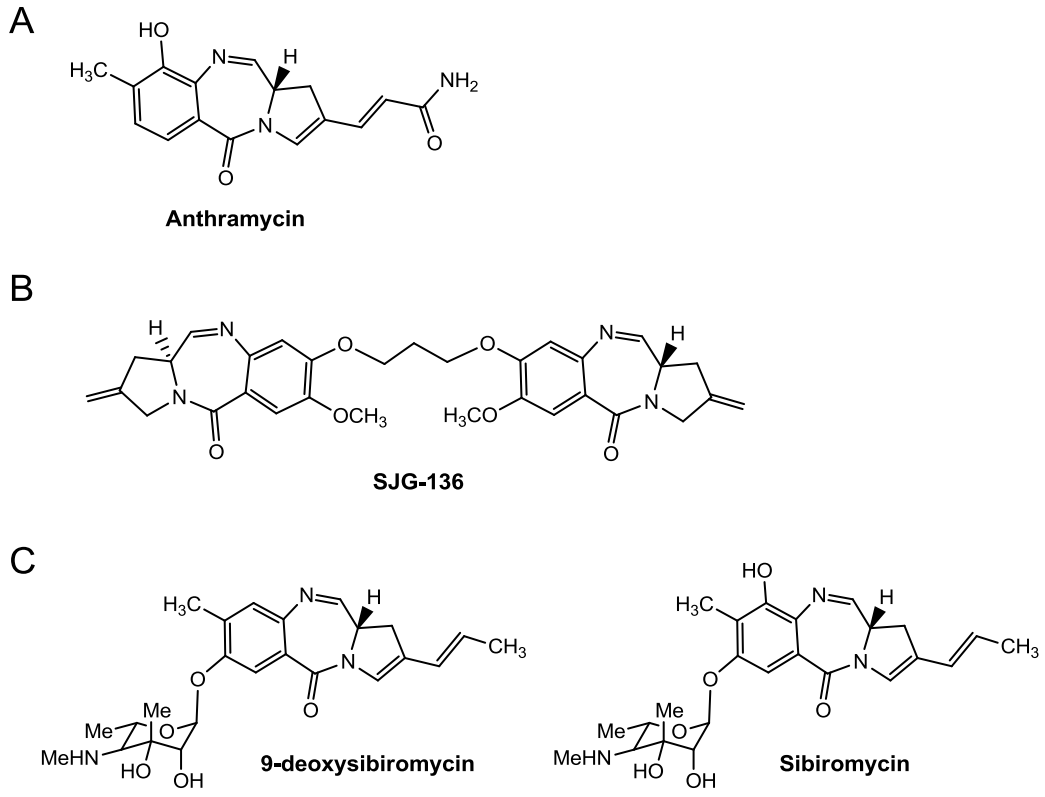

Figure 1-1. (A) The pyrrolo[1,4]benzodiazepine anthramycin; (B) the synthetic PBD dimer, SJG-136; (C) 9-deoxysibiromycin, a sibiromycin analogue, and the parent NP sibiromycin.

Interest and initiative to develop more potent PBD analogues as potential chemotherapeutic agents to treat cancer stem from current knowledge of PBD structural-activity relationships (*3, 5*) and the identification and characterization of the PBD

biosynthetic gene clusters of anthramycin (*7*), tomaymycin (*8*) and sibiromycin (*9*). A recent and encouraging example is the mutasynthesis of a sibiromycin analogue, 9-deoxysibiromycin (Figure 1-1C). This PBD analogue shows increased anti-tumor activity and reduced cardiotoxicity without the hydroxyl group at position 9 that is present in sibiromycin, the parent natural product (*10*).

The chemical scaffold of PBDs is a three ring system with two conserved features (Figure 1-2A): 1) an imine group at N10-C11, where DNA alkylation occurs at C11 and 2) *S*-stereochemistry at C11a that creates a right-handed twist to the PBD core structure. The right-handed twist of the PBD core matches the right-handed twist of B-DNA, allowing for suitable binding in the minor groove (*11*) with subsequent nucleophilic attack by the exocyclic nitrogen of a guanine base (*3*) (Figure 1-2B). The chemical substituents of rings A and C, and saturation of ring C, vary among naturally produced PBDs and relate to their overall antimicrobial and/or anti-tumor biological activities (*3*). However, the key chemical attributes of PBDs contributing to their anti-tumor chemotherapeutic properties and potency are:

1) The absence of chemical substituents at C9; bulky substitutions inhibit DNA binding and the C9 hydroxyl group has been attributed to cardiotoxicity (*3, 10, 12*).
2) The presence of electron donating groups at C7 and C8; donation of electron density to the benzodiazepine ring system favors the biologically active imine form over the inactive carbinolamine form (*3, 12*).
3) *O*-glycosylation at C7; enhancement of the DNA-binding affinity is the proposed interaction between the positively charged sibirosamine sugar moiety of sibiromycin and negatively charged phosphate backbone of DNA (*3, 12*).

4) C2-endo or exocyclic unsaturation; the internal or external double bond at C2 flattens ring C to improve the binding and fit of the PBDs into the minor groove of DNA and is observed in PBDs with the greatest anti-tumor potency (*12-15*).

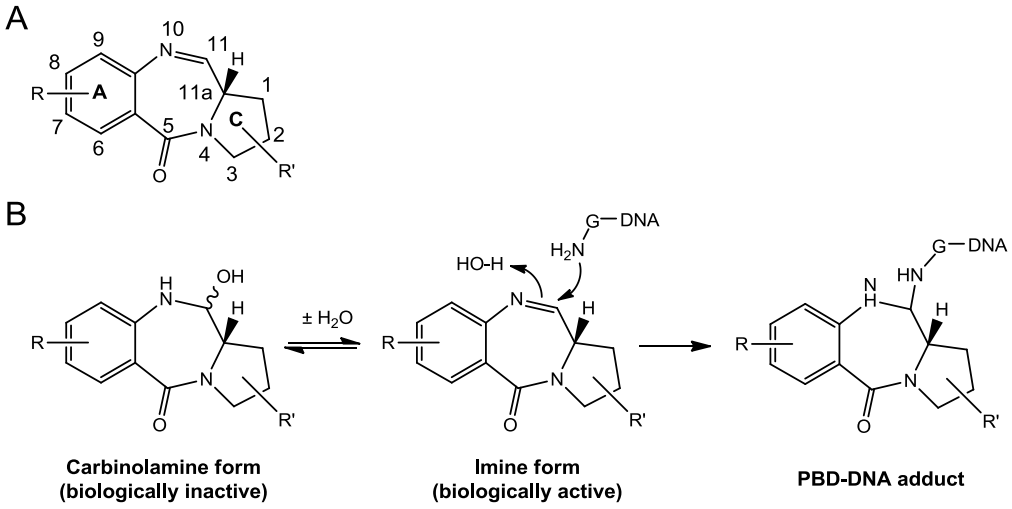

Figure 1-2. (A) Common ring structure of PBDs; (B) Mechanism of PBD-DNA complex formation.

1.2 Ring C of PBDs - a novel biosynthetic transformation of L-tyrosine to the hydropyrrole moiety.

L-Tryptophan, L-tyrosine and L-methionine are the metabolic precursors and biosynthetic origins of anthramycin, tomaymycin and sibiromycin (Figure 1-3) (*16, 17*). The biosynthetic assembly of the PBD scaffold occurs by a nonribosomal peptide synthetase (NRPS) that links together an anthranilic acid moiety derived from L-tryptophan (or chorismate for tomaymycin) and a hydropyrrole moiety derived from L-tyrosine (*7-9*).

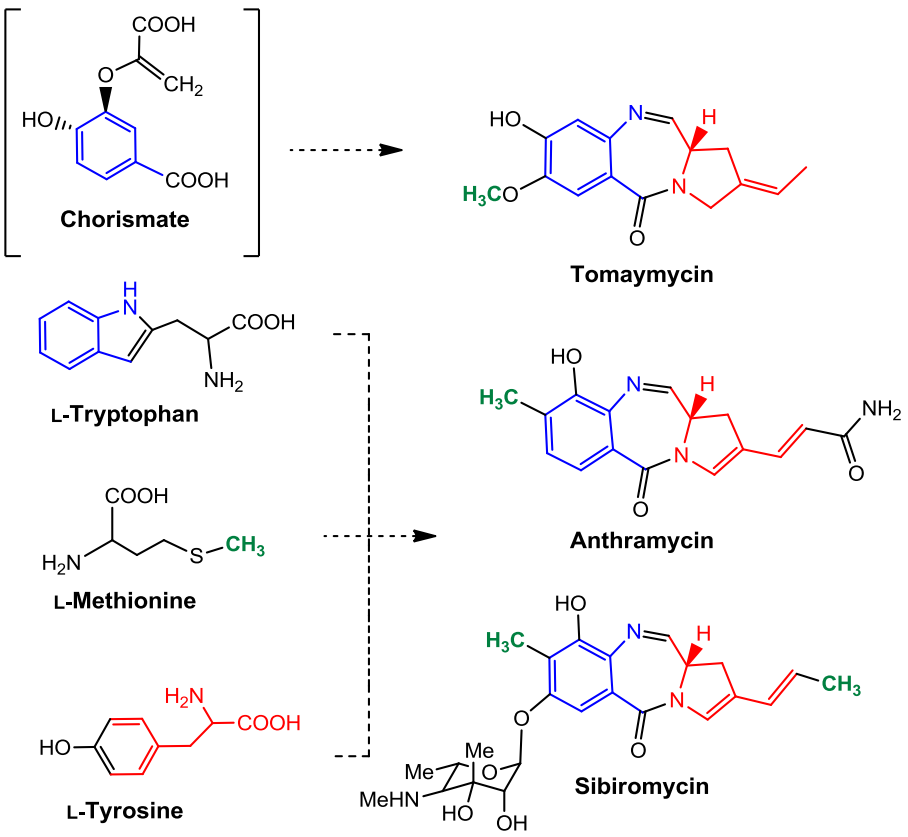

Figure 1-3. Labeling pattern of atoms in the metabolic precursors L-tryptophan (blue), L-methionine (green) and L-tyrosine (red) found in the natural products of anthramycin, tomamycin and sibiromycin. Chorismate is the chemical precursor of the anthranilate moiety in tomamycin.

The biosynthetic pathway for the unusual transformation of L-tyrosine to the hydropyrrole moiety has not been well characterized beyond establishing its metabolic origins, and to date is unique to the biosynthesis of PBDs (*18, 19*), lincosamides (*20, 21*) and hormaomycin (*22*). Similar to PBDs, lincosamides and hormaomycin are also natural products from actinomyces and have different biological activities based upon their chemical properties (Figure 1-4A). Lincosamides disrupt and inhibit protein synthesis (*23*) and hormaomycin is a despeptide with potent narrow-spectrum antibiotic activity (*24*). The final hydropyrrole moiety incorporated into PBDs, lincomycin A and

hormaomycin is varied due to the enzymes present in the respective biosynthetic pathways (*7-9, 22, 25*). However, the starting point of this pathway begins with the same metabolic precursor, L-tyrosine, in which the biosynthesis of the hydropyrrole moiety is proposed to proceed through L-DOPA by hydroxylation of L-tyrosine (Figure 1-4B).

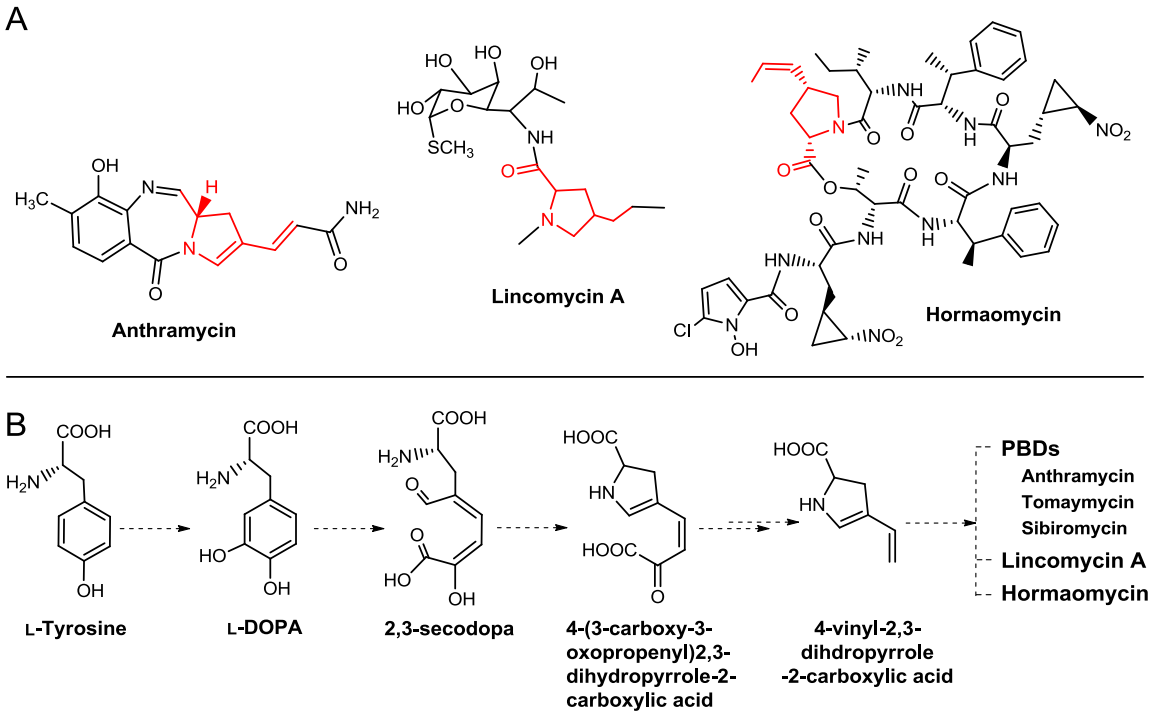

Figure 1-4. (A) The natural products anthramycin (a PBD), lincomycin A (a lincosamide), and hormaomycin with the hydropyrrole moiety highlighted red; (B) The proposed biosynthetic pathway for the hydropyrrole moiety found in PBDs, lincomycin A and hormaomycin.

1.3 Precedence for the putative function of Orf13 as an L-tyrosine hydroxylase

The first proposed step in the hydropyrrole moiety biosynthesis is L-tyrosine hydroxylation. Prior to the identification of PBD biosynthetic gene clusters (*7-9*), initial studies were performed to identify the function of enzymes in the hydropyrrole moiety biosynthetic pathway of lincomycin A (*26, 27*). The tyrosine hydroxylase function of

LmbB2 was first suggested from cell free extract studies with LmbB2 and LmbB1, a putative 2,3-extradiol dioxygenase (Figure 1-5) (*27*). Formation of a yellow product with an absorbance at 414 nm, later assigned to the cyclized imine 4-(3-carboxy-3-oxopropenyl)2,3-dihydrophyrrole-2-carboxylic acid (*26*), was observed when the cell free extract of co-expressed LmbB2 and LmbB1 was provided L-tyrosine as the substrate. However, no conversion of L-tyrosine to the cyclized imine was observed with cell free extract containing only LmbB1. Additional study of purified LmbB1 only showed L-DOPA conversion to the cyclized imine which confirmed the 2,3-extradiol dioxygenase function of LmbB1, and indicated LmbB2 to be the putative tyrosine hydroxylase (*27*).

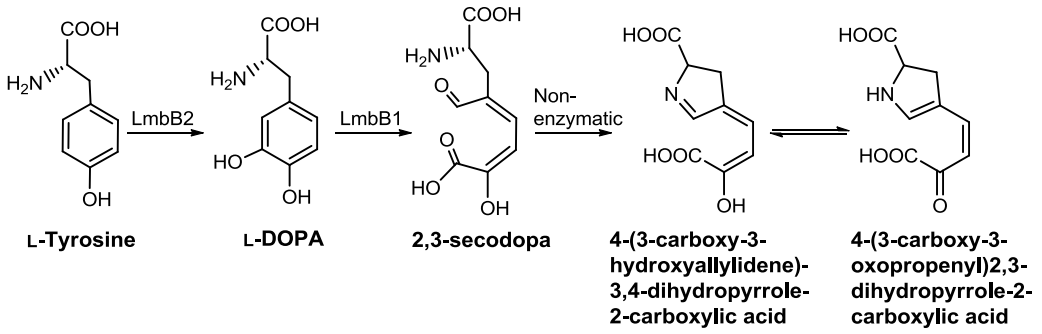

Figure 1-5. Initial biosynthetic steps of the hydropyrrole moiety in lincomycin A.

Orf13, from the anthramycin biosynthetic gene cluster, is proposed to catalyze L-tyrosine hydroxylation based on sequence homology with LmbB2 (*7*). This putative tyrosine hydroxylase also shares sequence homology with TomI and SibU from the PBD biosynthetic pathways of tomaymycin and sibiromycin, respectively, as well as HrmE from the hormaomycin biosynthetic pathway. Additional homologues were identified by searching the NCBI protein databank in a BLAST search using Orf13 as the protein query sequence (Table 1-1). However, no other similar proteins or conserved domains

resulted from the BLAST query to indicate that the function for this group of proteins is tyrosine hydroxylation. No further information is reported in the literature relating to the characterization of the identified homologues other than the preliminary studies with LmbB2 proposing the tyrosine hydroxylase function. The limited information available beyond the putative functional assignment of these tyrosine hydroxylases sparks interest in their characterization as they have the potential to define a new class of tyrosine hydroxylases.

Table 1-1. Sequence Homology of the Putative Tyrosine Hydroxylase Orf13[a]

Tyrosine Hydroxylase	Producer	Natural Product	% Identity/ Similarity[b]	NCBI Accession No.
LmbB2	*Streptomyces lincolnesis*	Lincomycin A	34/44	CAA55748
SibU	*Streptosporangium sibiricum*	Sibiromycin	38/48	ACN39744
TomI	*Streptomyces achromogenes* ATCC 3143	Tomaymycin	34/45	ACN39022
HrmE	*Streptomyces griseoflavus*	Hormaomycin	34/46	AEH41783
AMED_5527	*Amycolatopsis mediterranei*	Unknown[d]	33/43	YP_003767687
O3I_32261	*Nocardia brasiliensis* ATCC 700358	Unknown[d]	64/76	ZP_09842397
S_W007[c]	*Streptomyces sp. W007*	Unknown[d]	37/47	ZP_09407229
Shyg_5008[c]	*Streptomyces hygroscopicus jinggangensis* 5008	Unknown[d]	35/45	AEY93897

[a] Orf13 of the anthramycin biosynthetic gene cluster (*Streptomyces refuineus thermotolerans* NRRL 3143; Accession No. ABW71844).
[b] Sequence analysis performed with Needleman-Wunsch Global Alignment; NCBI BLAST (*28*).
[c] Designated abbreviation of putative tyrosine hydroxylase to indicate producer in this thesis.
[d] The natural product biosynthetic gene cluster has not been reported.

1.4 Enzymes catalyzing L-tyrosine hydroxylation and/or aromatic hydroxylation

The chemical reaction of L-tyrosine to L-DOPA is an *ortho*-hydroxylation of an aromatic ring. Enzymes responsible for this type of reaction include tyrosinases and aromatic hydroxylases, which are considered monophenol monooxygenases (MMOs) catalyzing an oxygen transfer reaction in which 1 atom of molecular oxygen (O_2) is inserted into an aromatic substrate. There are 5 distinct classes of MMOs defined primarily by their cofactor requirement (*29*) (Table 1-2). These are the heme dependent cytochrome P450 enzymes (*30*) and heme peroxidases (*29, 31*), the di-iron hydroxylases (*32*), the non-heme iron pterin or α-ketoglutarate dependent monooxygenases (*33*), the type III copper dependent monooxygenases (*34*), and the metal free flavin dependent monooxygenases (*29*). Within the 5 classes of MMOs, the non-heme iron pterin and α-ketoglutarate dependent enzymes are specific for the *ortho*-hydroxylation of L-tyrosine to L-DOPA and have a highly conserved 2-His-1-carboxylate triad catalytic motif (*35*). While on the other hand, aromatic hydroxylation observed with heme peroxidases is a secondary pathway dependent on molecular oxygen and dihydroxyfumaric acid (*36, 37*) that is separate from their main catalytic function of 2-sequential 1-electron oxidization reactions with hydrogen peroxide (*29, 31*).

Table 1-2. Classes of Monophenol Monooxygenases (MMOs)

Enzyme Class	Enzyme Type	Cofactor/ Cosubstrate [a]	Active Site/ Catalytic Motif
Heme dependent	Cytochrome P450	Heme A, B or C	Thiolate-ligated heme; $FX_2GX_bX_3C_pXG$
	Heme Peroxidases	Heme B/ DHFA	Histidyl-ligated heme; Active site: $RX_2F(W)H$
Dinuclear non-heme iron	Di-iron hydroxylases	Fe^{3+}-OH- Fe^{3+}	Carboxylate-bridged di-iron center
Mononuclear non-heme iron	Pterin dependent	Fe^{2+}/BH_4	$HX_4HX_{39}E(D)$; $HXE(D)X_{39}H$
	α-KG dependent	Fe^{2+}/α-KG	$HXDX_{48\text{-}153}H$
Copper dependent	Type III copper	Cu^{2+}	$Cu^{+/2+}$ - $Cu^{+/2+}$ Conserved histidines
Flavin dependent		FAD/NAD(P)H	Flavin, metal free

[a] Abbreviations: Dihydroxyfumaric acid (DHFA), tetrahydrobiopterin (BH_4), alpha-ketoglutarate (α-KG), flavin adenine dinucleotide (FAD), nicotinamide adenine dinucleotide (phosphate) (NAD(P)H).

An initial indication of a possible cofactor requirement was not evident after analysis of the conserved residues in Orf13 from a multiple sequence alignment with its known homologues (Figure 1-6) compared against the 5 classes of MMOs. This poses an intriguing question as to the cofactor requirement for this putative tyrosine hydroxylase. The enzyme may require an already established cofactor for MMOs, a new cofactor or have no cofactor requirement at all. For all cases, this enzyme represents a new class performing tyrosine and aromatic hydroxylation.

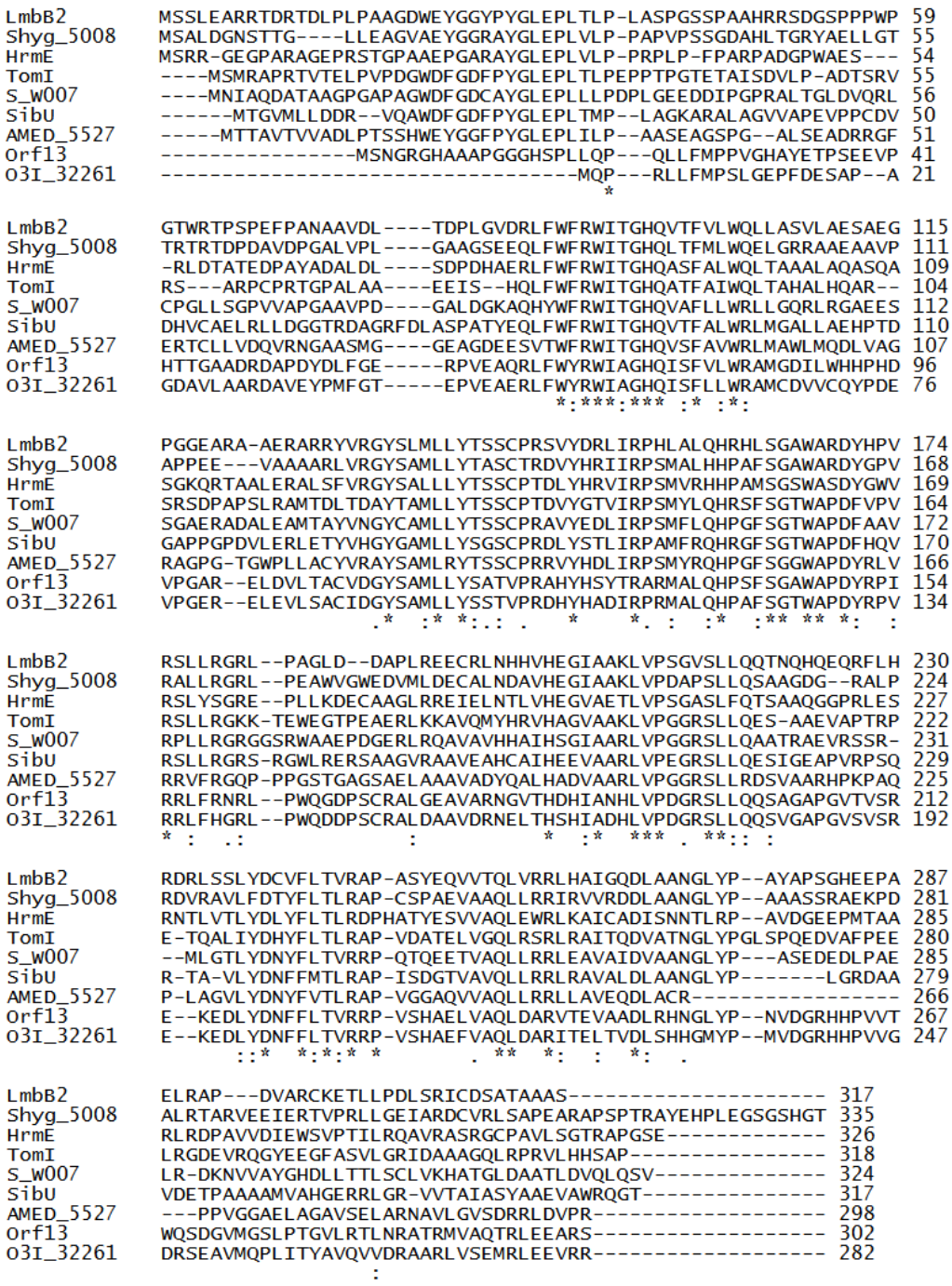

Figure 1-6. Multiple sequence alignment of the putative tyrosine hydroxylases from actinomyces; Orf13 (*S. refuineus*; anthramycin), TomI (*S. achromogenes*; tomamycin), SibU (*Streptosporangium sibiricum*; sibiromycin), LmbB2 (*S. lincolnesis*; lincomycin A), HrmE (*S. griseoflavus*; hormaomycin), AMED_5527 (*Amycolatopsis mediterranei*; unknown NP), Shyg_5008 (*S. hygroscopicus jinggangensis*; unknown NP) and S_W007 (*S. sp.W007*; unknown NP), and O3I_32261 (*Norcardia brasiliensis*; unknown NP).

1.5 Specific Aims

The intrigue and impetus to characterize the tyrosine hydroxylase involved in the first step of hydropyrrole biosynthesis in PBDs are centered on the possibility of identifying the first class of bacterial tyrosine hydroxylases and defining a new MMO class based on its resulting cofactor requirement, chemical mechanism and/or structural fold. The putative tyrosine hydroxylases available for characterization are SibU (*Streptosporangium sibiricum*), TomI (*Streptomyces achromogenes*) and Orf13 (*Streptomyces refuineus thermotolerans*). Of these three, only Orf13 was selected for characterization since it originates from a thermophile and would likely be a more stable enzyme than SibU and TomI. The goal of my research was to characterize Orf13, the putative tyrosine hydroxylase from the anthramycin biosynthetic gene cluster, in order to determine the enzyme cofactor requirement for catalysis, confirm enzymatic function for L-tyrosine hydroxylation, perform steady-state kinetic analysis and begin initial mechanistic investigation of L-tyrosine hydroxylation based on the assigned enzyme classification. This dissertation specifically addresses the following:

1) Enzyme purification of Orf13 and cofactor identification. This includes initial cloning and purification methods to obtain and maintain stable and active enzyme, while also describing the identification of a bound heme B cofactor.
2) Functional characterization of Orf13 and classification as a heme peroxidase. Assessment of heme B as a catalytically required cofactor for tyrosine hydroxylation is addressed, in addition to the classification of Orf13 as a heme peroxidase based on reaction requirements, spectroscopic evidence and steady-state kinetic analysis.

3) Additional characterization of Orf13 as a heme peroxidase and initial investigation of the chemical mechanism of L-tyrosine hydroxylation. Further experimentation is described to define substrate specificity for aromatic hydroxylation, to identify the proximal (5^{th}) heme-iron ligand and to identify the oxygen source for tyrosine hydroxylation.

Chapter 2: Enzyme purification of Orf13 and cofactor identification

2.1 Introduction

Orf13 (*S. refuineus*) is the proposed tyrosine hydroxylase from the anthramycin biosynthetic gene cluster. Protein purification must first be performed in order to identify the presence of a cofactor. The initial cloning, expression and purification of Orf13 is described. Alongside the development of the protein purification process, a bound cofactor was discovered and identified as heme B. The stoichiometry of heme B was evaluated and expression conditions were optimized to obtain fully occupied enzyme containing heme B.

2.2 Experimental Procedures

Materials. The pSMT3 vector was generously provided by Dr. Christopher D. Lima (Memorial Sloan-Kettering Cancer Center) (*38*), the pET24a vector was purchased from Novagen (Darmstadt, Germany) and the pCW vector and RP523 *E. coli* strain were generously donated by Professor Michael A. Marletta (University of California at Berkeley). Molecular cloning materials: restriction enzymes NdeI and HindIII were purchased from New England Biolabs (Ipswich, MA); dNTPs, Pfu DNA Polymerase, T4 ligase and DNA molecular weight ladder were purchased from Fermentas (Ontario, Canada). All purification resins and protein molecular weight standards for the quaternary structure determination were purchased from G.E. Healthcare (Piscataway, NJ). Sodium phosphate, imidazole, sodium chloride, and D-lactose were purchased with

the highest purity from ThermoFisher Scientific (Fair Lawn, NJ). Dithiothreitol (DTT) and phenylmethanesulfonylfluoride (PMSF) were purchased from American Bioanalytical Inc. (Natick, MA). Glycerol, heme B, protoporphyrin IX (PPIX) and all other chemicals were purchased with the highest purity from Sigma Aldrich (St. Louis, MO).

General Methods. DNA isolation was performed using the Fermentas GeneJet Plasmid Miniprep kit (Glen Burnie, MD). PCR amplifications were carried out using a PTC-200 DNA Engine Cycler (Bio-Rad). All DNA agarose gel electrophoresis was performed at 100 V using 1% (w/v) agarose gels with GeneRuler 1 Kb Plus DNA Ladder (Fermentas). All DNA restriction digestion and ligation reactions were performed according to the manufacturer's protocol. All DNA sequencing was performed at the Institute for Bioscience & Biotechnology Research (IBBR) DNA Sequencing Facility (University of Maryland, College Park, MD). Bacterial transformations of plasmid constructs into *E. coli* were carried out with a MicroPulser Electroporator (Bio-Rad; 2500 V, 1 mm gap cuvette) and plated on LB agar with kanamycin (50 μg/mL) antibiotic selectivity. Protein concentrations of Orf13 were determined at A_{280} nm using an experimental extinction coefficient (ε_{280} 2.8 ± 0.2 mL mg^{-1} cm^{-1} (pH 8.0, 25 °C)) that was calculated by quantitative amino acid analysis (AAA Service Laboratory; Damascus, Oregon). All protein electrophoresis was performed at 200 V with the Mini Protean 3 Cell gel electrophoresis system (Bio-Rad) using denaturing sodium dodecyl sulfate-polyacrylamide gel electrophoresis (SDS-PAGE) gels (12% acrylamide resolving and 4% stacking) with a PageRuler Prestained Protein Ladder (Fermentas) in 1X SDS-PAGE running buffer (25 mM Tris-base, 190 mM glycine and 0.1% (w/v) SDS). All protein

gels were stained with Coomassie Brilliant Blue and destained with 10-20% (v/v) acetic acid.

All UV-visible absorption spectra or measurements were obtained with a Varian UV-vis Cary100 Spectrophotometer with Temperature Controller (Walnut Creek, CA). High performance liquid chromatography was performed with an Agilent 1000 Series HPLC (Foster City, CA) equipped with 1100 Series multiple wavelength detector and 1200 Series fluorescence detector. Electrospray ionization mass spectrometry with tandem mass spectrometry (ESI-MS/MS) was performed with an LTQ Orbitrap XL (Thermo Scientific; San José, CA) in the Proteomic Core Facility at the University of Maryland (College Park, MD). Metal analysis of Orf13 by inductively coupled plasma mass spectrometry (ICP-MS) was performed in Department of Geological Sciences at Michigan State University (East Lansing, MI). Anaerobic experiments were performed in an 830-ABC series compact glovebox (PLAS-LABS, Inc; Lansing, MI) equipped with a Model 10 Gas Analyzer and Digital Heated Fan Box with palladium catalyst bed (Coy Laboratory Products, Inc; Grass Lake, MI).

Cloning of His_6SUMO-Orf13 and native Orf13. The gene encoding Orf13 was amplified by PCR from the p-ANT-1 cosmid containing the anthramycin gene cluster that was constructed by Dr. Wei Li in our laboratory (unpublished results). NdeI and HindIII restriction sites (underlined) were incorporated into the primers for insertion into the pSMT3 and pET24a vectors; forward primer 5'-GGTGGTCATATGAGCAACGGCCGAGG-3' and reverse primer 5'-GGTGGTAAGCTTTCATGACCGGGCTTCC-3'. Amplified *orf13* was isolated by QIAquick gel extraction kit (Qiagen), digested with NdeI and HindIII, ligated into the

pSMT3 and pET24a vectors, and transformed into GeneHogs (Invitrogen; Carlsbad, CA). DNA sequencing confirmed correct construction of the pSMT3/*orf13* and pET24a/*orf13* plasmids for the recombinant expression of His_6SUMO-Orf13 and native Orf13, respectively, in BL21(DE3) *E. coli*.

Expression of Orf13 constructs in BL21(DE3) *E. coli.* Individual constructs of Orf13 plasmids (pSMT3/*orf13* or pET24a/*orf13*) (50-100 ng) were incubated with 40 µL of electro-competent BL21(DE3) *E. coli* cells for 2 min on ice, transformed by electroporation at 2500 V, transferred to 1 mL of LB medium and were allowed to recover for 1 hr at 37 °C. After recovery, 10-20 µL of cells were plated on LB agar containing kanamycin (50 µg/mL) and incubated for 10-12 hr at 37 °C. One colony per seed (starter) culture of LB medium (50 mL in 250 mL Erlenmeyer flask) with 50 µg/mL kanamycin antibiotic selectivity was selected and grown to oversaturation for 12-15 hr at 37 °C at 250 rpm. An aliquot of the seed culture (20 mL) was used to inoculate an expression culture of LB medium (2 Liters in a 4 Liter Erlenmeyer flask) with 50 µg/mL kanamycin antibiotic selectivity and protein expression was induced with D-lactose (0.2% w/v) when the optical density of the cells at 600 nm (OD_{600}) reached 0.8 – 1.0. Protein expression occurred for 8 hr at 37 °C with a rotation speed of 250 rpm. Cells were harvested 8 hr after induction by centrifugation at 5,000 rpm for 10 min at 4 °C. The cell pellets were flash frozen in liquid nitrogen and stored at -80 °C until purification. Optimized expression conditions for native Orf13 are as previously described with only the addition of ferric iron (III) citrate (500 µM final) in the expression culture. In the preparation of the expression culture, solid iron (III) citrate is added to the media and

autoclaved (Note: this iron salt form is only soluble when added to boiling solutions or media which is then autoclaved).

Cloning and expression of native Orf13 for RP523 *E. coli*. The *orf13* gene was also cloned into the pCW vector for recombinant expression in RP523 *E. coli* by digestion of pET24a/*orf13* with HindIII and NdeI and insertion into the pCW vector cut with the same restriction enzymes. DNA sequencing confirmed the correct construction of pCW/*orf13*. This construct was transformed into RP523 *E. coli* cells as described for BL21(DE3) *E. coli*. However, all cells were grown in Terrific Broth (TB) media with ampicillin (75 μg/mL) antibiotic selectivity in the presence of hemin (30 μg/mL).

Purification of His_6SUMO-Orf13. One gram of cells expressing His_6SUMO-Orf13 was chemically lysed with 1X BugBuster® (Novagen) and lysozyme (0.5 mg/mL) by mild inversion in buffer A (50 mM Tris-HCl (pH 8.0), 300 mM NaCl, 25 mM ascorbate, 1 mM DTT and 1 mM PMSF) and centrifuged at 15,000 rpm for 30 min at 4 °C. The cell free extract was loaded onto a 2 mL column of Ni-NTA (Qiagen) pre-equilibrated with buffer A. The column was washed at 1 mL/min at 4 °C in the following sequence with buffer A: 20 column volumes (CV) of buffer A only, 10 CV with 20 mM imidazole, a 10 CV linear gradient from 20 to 50 mM imidazole, 10 CV with 50 mM imidazole, a 10 CV linear gradient from 50 to 100 mM imidazole, and 10 CV with 100 mM imidazole. Fractions containing His_6SUMO-Orf13, assessed by SDS-PAGE, eluted at 100 mM imidazole and were pooled and concentrated using a filtration chamber under nitrogen gas with an Amicon membrane (30 kDa MWCO; Millipore, Billerica, MA) to ~1 mg/mL. Cleavage to remove the His_6SUMO fusion tag was performed using the Ulp1 Sumo protease at a mass ratio of 1:50 (Ulp1:His_6SUMO-Orf13) for 12 hr during dialysis

against buffer A at 4 °C. The protein solution was then re-loaded onto the Ni-NTA column re-equilibrated with buffer A, but finally eluted with 200 mM imidazole (See Results and Discussion).

Purification of native Orf13. Six grams of cells expressing native Orf13 were lysed by French press (4 passes at 10,000 psi) and the cell free extract was loaded onto a 6 mL column of Ni-Sepharose pre-equilibrated with buffer A (50 mM sodium phosphate (pH 8.0), 300 mM NaCl and 1 mM DTT). The column was washed with 20 column volumes of buffer A containing 20 mM imidazole at 1 mL/min at 4 °C. Orf13 was eluted with 3 column volumes of buffer A containing 80 mM imidazole and fractions containing the enzyme were pooled and concentrated using a filtration membrane Amicon (30 kDa MWCO) by centrifugation (Millipore; Billerica, MA) to a concentration of 15-20 mg/mL. The concentrated enzyme solution was then loaded onto a S-200 HR column (2.5 x 40 cm; 196 mL CV) pre-equilibrated with buffer B (10 mM imidazole, 50 mM sodium phosphate (pH 8.0), 300 mM NaCl and 10% glycerol) and eluted at 0.4 mL/min at 4 °C. Fractions containing Orf13 were pooled and concentrated to at least 10 mg/mL as previously described, flash frozen by liquid nitrogen in droplet form and stored at -80 °C. Purity of Orf13 was greater than 95% as judged by SDS-PAGE (Figure 2-2D). The protein concentration was determined using the experimentally determined extinction coefficient ε_{280} 2.8 ± 0.2 mL mg^{-1} cm^{-1} (pH 8.0, 25 °C) with final purification yields of 2-3 mg of Orf13 per gram of cell lysed.

An alternative purification method for native Orf13 by anionic exchange chromatography was also developed. Six grams of cells were lysed by French press and the cell free extract was loaded onto a Q-Sepharose column (2.5 x 49 cm; 240 mL CV)

pre-equilibrated with buffer A (50 mM sodium phosphate (pH 8.0), 30 mM NaCl, 50 mM DTT and 10% glycerol). The column was washed with 3 CV of buffer A at 2 mL/min at 4 °C, followed by a salt gradient of 30 mM – 600 mM NaCl within 1.2 Liters. Orf13 eluted between 120 – 150 mM NaCl of the linear gradient and fractions containing the enzyme were pooled and concentrated to 10 mg/mL as previously described. Gel filtration S-200HR chromatography was performed as described before with buffer containing 50 mM sodium phosphate (pH 8.0), 300 mM NaCl, 50 mM DTT and 10% glycerol. Orf13 was obtained with similar yield and purity as with the Ni-Sepharose purification method.

An optimized purification system was developed for native Orf13. This involved the final gel filtration step to be carried out in an anaerobic glove box to obtain stable Orf13 without the presence of imidazole. Cell lysis and the Ni-Sepharose purification steps for native Orf13 were performed as described above. The concentrated protein solution in an open conical tube (15 mL) was brought into an anaerobic glove box after 4 cycles of high vacuum degassing (-70 kPa) and N_2 (g) purge in the antechamber, and allowed to equilibrate in the anaerobic glove box for 10 minutes. The protein solution was loaded onto an anaerobic S-200 HR column (2.5 x 40 cm; 196 mL CV) pre-equilibrated with anaerobic buffer C (20 mM sodium phosphate (pH 8.0), 80 mM NaCl and 10% glycerol) and eluted at 0.4 mL/min at 25 °C. Fractions containing Orf13 were pooled and concentrated to at least 10 mg/mL as previously described, but with the important exception that the centrifugation membrane filter used for concentration had been stored in the glove box 1 week prior to purification and was sealed with pressure sensitive tape (vinyl plastic delineator tape; Fisher Scientific) prior to removal from the

glove box to maintain anaerobic conditions. The concentrated protein solution in the sealed centrifugation membrane filter was brought back into the glove box after 4 cycles of high vacuum degassing (-70 kPa) and N_2 (g) purge in the antechamber, and the protein was flash frozen by liquid nitrogen in droplet form within the glove box. The frozen enzyme droplets were quickly transferred to a storage tube, removed from the glove box and stored at -80 °C. Anaerobic Orf13 was obtained with similar yield, purity and stability (Figure 2-2E) as the aerobic Ni-Sepharose and gel filtration purification method initially described.

Quaternary structure determination by gel filtration. The oligomeric state of purified native Orf13 was determined using a Superdex200 column (1 x 30 cm; 24 mL CV) pre-equilibrated at 4 °C with 50 mM sodium phosphate (pH 8.0), 150 mM NaCl and 50 mM DTT at 0.4 mL/min. Molecular weight standards used were ribonuclease A (13.7 kDa), ovalbumin (44 kDa), conalbumin (75 kDa) and aldolase (158 kDa).

High performance liquid chromatography and mass spectrometry for porphyrin detection and identification. An HPLC method to detect porphyrins was performed as previously described (*39*). Samples (110 µL) of Orf13 and/or standards of heme B (iron protoporphyrin IX) or protoporphyrin IX (PPIX) were incubated at room temperature for 1 hr in 2% (w/v) SDS. Porphyrins were detected at 405 nm. Heme B and PPIX standards had average retention times of 42 and 44 minutes, respectively. The peaks observed at 42 and 44 minutes from the Orf13 sample were collected, treated with formic acid (1%, v/v) and injected at 25 µL/min into an LTQ Orbitrap XL mass spectrometer. The parent ions of 616.3 m/z and 563.5 m/z observed for the 42 and 44

minute samples, respectively, were selected for fragmentation by Collision Induced Dissociation (CID). Heme B and PPIX standards were treated and analyzed accordingly.

Heme B quantitation and stoichiometry. The pyridine hemochromagen method was performed as described (*40*) with a UV-vis Cary100 Spectrophotometer. A basic pyridine solution containing 50% (v/v) pyridine and 200 mM NaOH was prepared fresh for all analyses. The concentration of heme B from Orf13 samples is calculated with the extinction coefficient 22.1 mM^{-1} cm^{-1} and the stoichiometric ratio of heme B determined by the molar ratio of heme B to Orf13. All analyses were performed in triplicate.

Circular dichroism measurements of Orf13. Far-UV CD measurements were performed on a Jasco J-810 Spectropolarimeter (Easton, MD) at 25 °C using rectangular quartz cells with a path length of 1.0 mm. The protein concentration of Orf13 with 100% heme B occupancy was 4 μM in 20 mM sodium phosphate (pH 8.0). The spectra were recorded with a 1 nm wavelength step at a scanning speed of 50 nm/min. Each spectrum was averaged from three continuous scans and corrected by subtraction of a blank run containing 20 mM sodium phosphate (pH 8.0).

2.3 Results and Discussion

Purification and enzyme stability of Orf13. Cell pellets after over expression of Orf13 are red in color and the color of the expression media becomes dark brown or black when expression is continued for more than 8 hours. The red cell color was the first indication of a cofactor likely bound to Orf13, while production of the black pigment suggested the enzyme to be active since this has been observed for the oxidative polymerization of L-DOPA (*41*). The first pilot purification of Orf13 with His_6SUMO-

Orf13 (pSMT3/*orf13*) revealed an intrinsic binding affinity of the native, non-fusion tagged protein with the Ni-NTA resin. This was observed after treatment with the Ulp1 protease had successfully cleaved the His_6SUMO fusion tag from Orf13, but the non-fusion tagged protein remained bound to the resin during the 2nd Ni-NTA purification step when washed with buffer A (Figure 2-1).

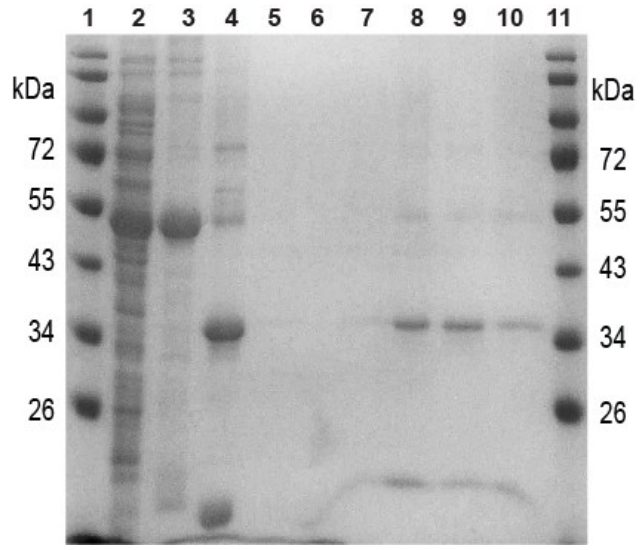

Figure 2-1. SDS-PAGE of His_6SUMO-Orf13 purification. Lanes 1 and 11 – Fermentas pre-stained protein ladder; lane 2 – cell free extract of soluble His_6SUMO-Orf13 (MW 47.4 kDa); lane 3 – pooled His_6SUMO-Orf13 after 1st Ni-NTA step; lane 4 – pooled His_6SUMO-Orf13 after the Ulp1 cleavage reaction; lanes 5-7 – 2nd Ni-NTA fractions washed with buffer A; lanes 8-10 – fractions of non-fusion tagged Orf13 (MW 33.6 kDa) from 2nd Ni-NTA washed with buffer A containing 200 mM imidazole.

The strategy for performing the 2nd Ni-NTA step after the Ulp1 cleavage reaction is to easily separate the native protein from the cleaved His_6SUMO tag. The His_6SUMO fusion tag will remain bound to the Ni-NTA resin re-equilibrated with buffer lacking imidazole while the native protein elutes from the column (*38*). This method has been successfully employed in our laboratory (*42*); however, this was not the case for Orf13.

The red colored protein eluted from the resin with 200 mM imidazole and SDS-PAGE of selected fractions during the first purification attempt had confirmed the removal of the His_6SUMO fusion tag (Figure 2-1, lanes 4 and 8-10).

The intrinsic binding affinity of Orf13 to the Ni-NTA resin was further explored with expression and purification of native, non-fusion tagged Orf13 (pET24a/*orf13*). Overall, native Orf13 binds more effectively to Ni-Sepharose (G.E. Healthcare) than Ni-NTA (Qiagen) resin, is retained on the resin bed with buffers containing 20 mM imidazole and completely elutes with 80 mM imidazole. This allowed for optimization of the Ni-Sepharose purification step (See General Methods) which consistently results in highly pure Orf13 (Figure 2-2A-E, lane 4). A final gel filtration step was added to the purification process to ensure homogeneity of the purified protein sample for all future studies, including assessment of cofactor stoichiometry, protein crystallization and steady-state kinetic analysis of Orf13. However, gel filtration of Orf13 proved to be a significant challenge as protein instability and degradation occurs readily (Figure 2-2A, lane 5). Protease activity as the source of the protein degradation was ruled out when similar degradation patterns were observed after performing gel filtration in the presence of a protease inhibitor cocktail (Sigma) (result not shown; refer to Figure 2-2A, lane 5).

The consistent protein degradation pattern of Orf13 following gel filtration always included degradation below the monomeric band (33.6 kDa) and the appearance of a MW band corresponding to a covalent dimer (~68 kDa) in denaturing SDS-PAGE gels. It was hypothesized that the protein instability and degradation is auto-oxidative in nature, relating to its oxygen sensitivity that is most likely promoted by some type of bound metal cofactor.

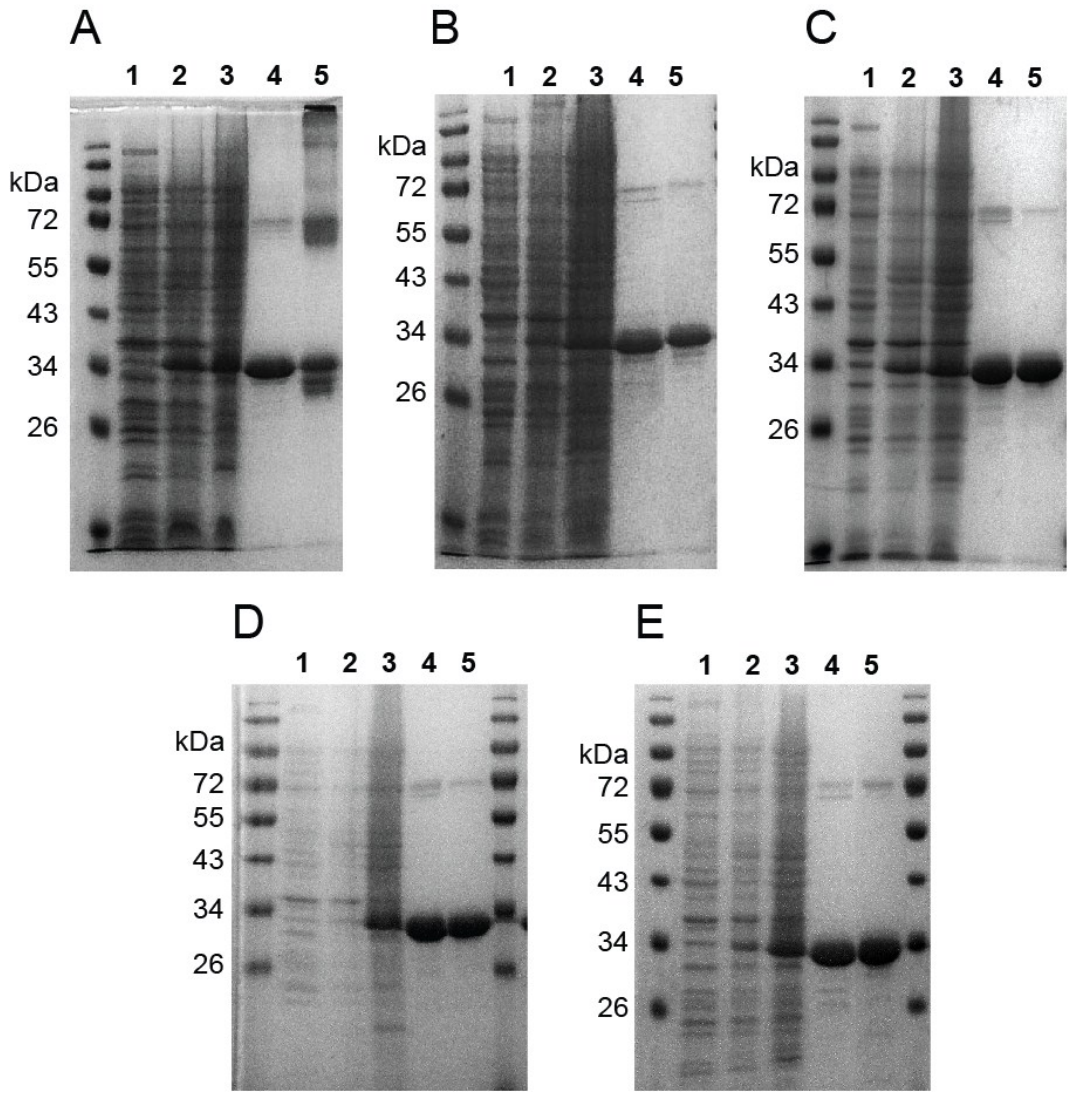

Figure 2-2. SDS-PAGE gels of native Orf13 purification without oxidative protection (A), with oxidative protection in the presence of 50 mM ascorbate (B), 50 mM DTT (C), 10 mM imidazole (D), or in a glove box under anaerobic conditions (E) during gel filtration. Lane 1 – un-induced pET24a/orf13 in BL21(DE3) *E. coli*; lane 2 – induced native Orf13 (MW 33.6 kDa); lane 3 – cell free extract; lane 4 – Pooled Orf13 after Ni-Sepharose step; and lane 5 – Pooled Orf13 after S-200 HR gel filtration.

Various gel filtration buffer conditions were assessed to obtain stable and active Orf13. Overall, the auto-oxidative damage of the protein is preventable when gel filtration is performed in the presence of reducing agents, such as ascorbate (50 mM) (Figure 2-2B) or DTT (50 mM) (Figure 2-2C), in the presence of imidazole (10 mM)

(Figure 2-2D), or under anaerobic conditions in a glove box without any chemical protectant (Figure 2-2E). Protein stabilization observed in the presence of reducing agents or in the absence of oxygen supported the proposed auto-oxidative degradation behavior. With the ability to successfully protect Orf13 from oxidative damage, the quaternary structure in solution was determined by gel filtration. Orf13 exists as a monomer in solution with an experimentally observed molecular weight of 37.9 kDa consistent with the predicted monomeric weight of 33.6 kDa (See Appendix A-1). Additionally, the experimental monomeric mass of Orf13 by MALDI-TOF-MS has an average monoisotopic peak of m/*z* 33,676 ± 58 Da that is also similar to the predicted value (See Appendix A-2).

Identification of heme B bound to Orf13. The visible red color of Orf13 indicated a bound cofactor. Characteristic absorbance bands of a heme moiety were observed in a UV-visible absorption spectrum of purified Orf13 (Figure 2-3). The Soret band at 408 nm indicated a ferric heme-iron in a penta-coordinate state based on the presence of a Q-band at 630 nm. The position of the Soret band in Orf13 is generally observed between 403-405 nm when purified anaerobically, 407 – 410 nm in the presence of ascorbate or imidazole, and 420-425 nm in the presence of DTT. Heme B was identified as the heme moiety non-covalently bound to Orf13 by co-elution with standard heme B by HPLC (Figure 2-4).

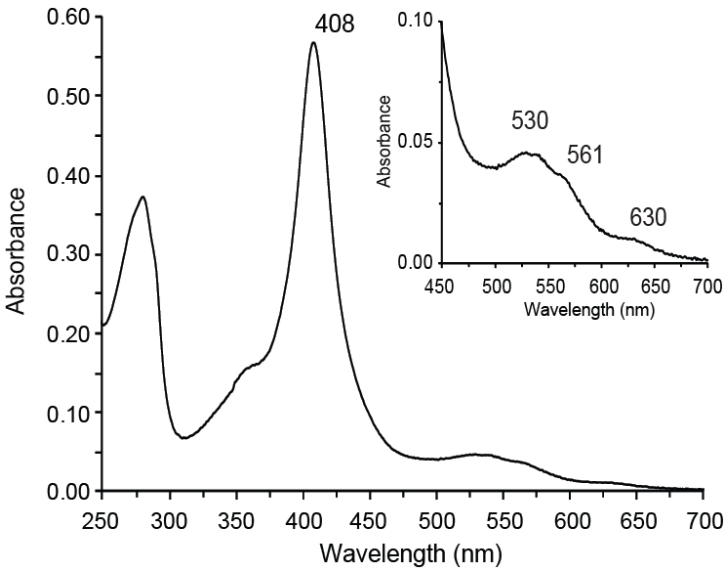

Figure 2-3. UV-visible absorption spectrum of purified Orf13 (100% heme B occupancy) in 20 mM Tris-HCl (pH 8.0), 10 mM imidazole and 10% glycerol. Soret band of heme B is observed at 408 nm and Q-bands at 530 nm, 561 nm and 630 nm (inset). Figure was modified from Connor, KL et al (*43*).

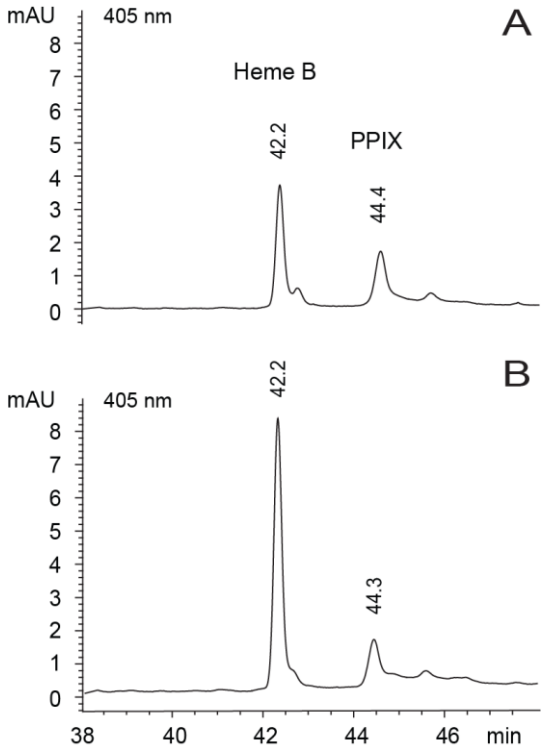

Figure 2-4. HPLC chromatograms for porphyrin detection: (A) Supernatant of denatured Orf13 sample; (B) Co-injection of the sample shown in A with heme B standard. Figure was modified from Connor, KL et al (*43*).

The HPLC peak at 42 minutes from the supernatant of denatured Orf13 was confirmed as heme B with subsequent ESI-MS/MS analysis (Figure 2-5). The precursor ion of 616.3 m/*z* is the same m/*z* observed in the heme B standard sample collected by HPLC at 42 minutes. It appears at exactly its molecular weight due to a radical porphyrin cation (*44*). ESI-MS/MS fragmentation of the precursor ion (616.3 m/*z*) generated a product ion peak at 557.2 m/*z*. The 59 amu difference in the product ion corresponded to the loss of $-CH_2COOH$ from one of the propanoic acid groups of heme B (*45*). This same fragmentation pattern was observed with the heme B standard sample.

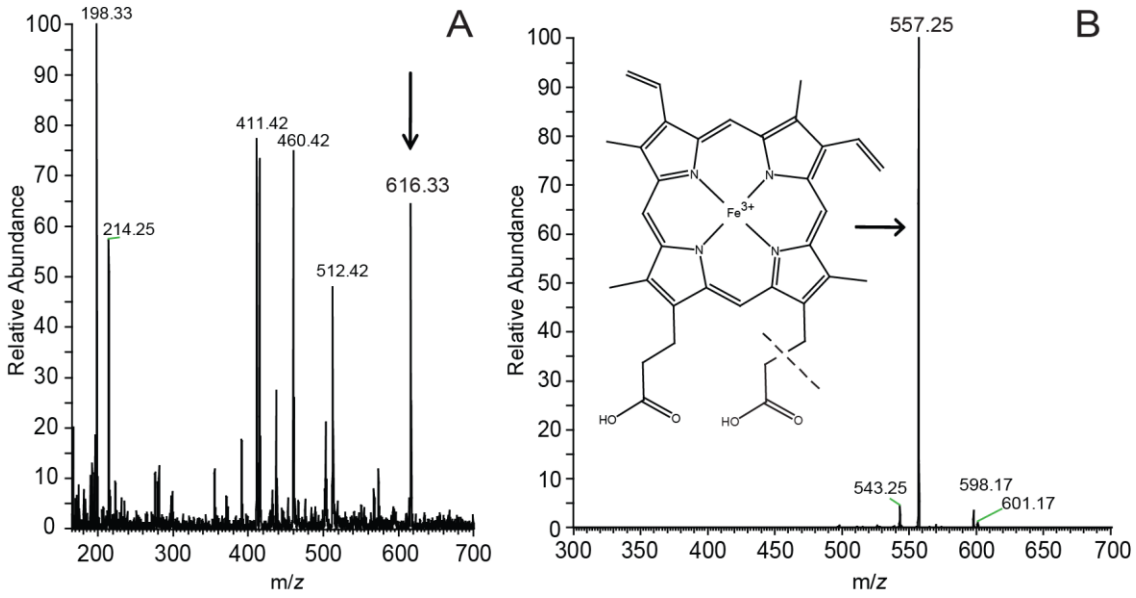

Figure 2-5. (A) ESI-MS of peak (T_R 42 min, Figure 2-4A) collected from HPLC of the supernatant from denatured Orf13; (B) ESI-MS/MS fragmentation of the precursor ion at 616.3 m/*z* generated a product ion peak at 557.2 m/*z*. Figure was modified from Connor, KL et al (*43*).

The stoichiometry of heme B in Orf13. Quantitation of heme B in Orf13 using the pyridine hemochromagen method (See Appendix A-3) showed a wide range of occupancy from 10% to 100% with Orf13 purified under conditions protecting the

enzyme from degradation. Orf13 with 100% heme B occupancy has a Reinheitszahl (RZ) value of 1.8, which is defined as the ratio of the Soret band absorbance (selected at 408 nm for Orf13) to the protein absorbance at 280 nm (Note: 100% heme B occupancy is defined as 1 heme B moiety per monomer of enzyme). Indications of second porphyrin species bound to Orf13 were first evident when the enzyme was purified in the presence of DTT and sub-stoichiometric amounts of heme B were measured. Two different Soret band species at 409 nm and 420 nm were commonly observed (Figure 2-6), where the latter species at 420 nm is heme B in a ferrous heme-iron state due to the presence of DTT. Auto-oxidation of ferrous heme-iron to ferric heme-iron was observed by a shift in the Soret band position from 420 nm to 404 nm, respectively, after buffer exchange to remove DTT and substitute with imidazole to protect Orf13 from degradation. The presence of the second porphyrin species had been initially masked by the Soret band of heme B in the ferric oxidation state.

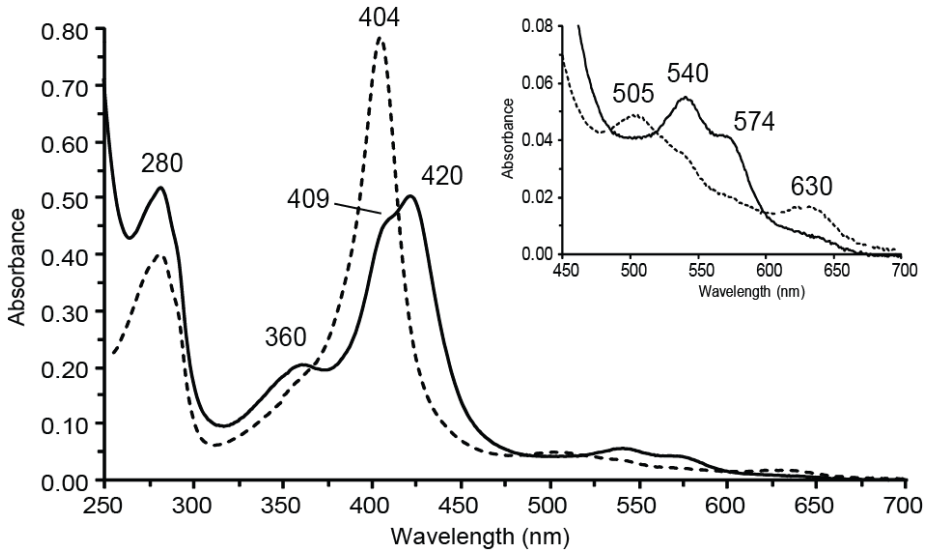

Figure 2-6. UV-visible absorption spectrum of Orf13 containing 75% heme B and 25% protoporphyrin IX (PPIX) before (solid line) and after (dashed line) buffer exchange to remove DTT (50 mM) and replace with imidazole (10 mM) in the storage buffer. Figure was modified from Connor, KL et al (*43*).

The Soret band species at 409 nm (Figure 2-6) was identified as protoporphyrin IX (PPIX), which remained unaffected by reducing agents as it lacks an iron center. The presence of PPIX bound to Orf13 was confirmed by co-injection of PPIX with Orf13 that showed an increase in the peak height of the compound observed at 44 minutes by HPLC (Refer to Figure 2-4; See Appendix A-4), and ESI-MS/MS analysis (See Appendix A-5). The amount of PPIX bound to Orf13 was determined by a calibration curve using HPLC and spectrophotometrically quantified PPIX (ε_{408nm} = 262 mM^{-1} cm^{-1} in 2.7 M HCl (*46*)) from which the stoichiometry was calculated by the molar ratio of PPIX and Orf13. Overall, the amount of PPIX bound to Orf13 made up the occupancy difference when sub-stoichiometric amounts of heme B were measured in purified enzyme (i.e. 75% heme B and 25% PPIX). No other organic cofactors were identified with Orf13 and no other metals, other than iron originating from heme B, were found by ICP-MS.

This is the first reported case in which a heme containing enzyme has been found to be fully occupied with a heterogeneous mixture of heme B and PPIX. Dissociation constants of heme B for enzymes utilizing the heme moiety in different capacities show a range of heme binding affinities; myoglobin for oxygen transport (1.3 x 10^{-14} M) (*47*), bovine serum albumin for transport (4.6 x 10^{-9} M) (*48*), *pa*-HO, a heme oxygenase, for heme degradation (0.6 x 10^{-6} M) and PhuS involved in heme binding, trafficking and transfer (0.2 x 10^{-6} M) (*49*). The dissociation constant of PPIX for ferrochelatase (1.5 x 10^{-6} M) (*50*) is similar to the heme B binding affinity for *pa*-HO and PhuS. Heme B and PPIX are tightly bound to Orf13 as there is no exchange or loss during dialysis unless the enzyme is denatured with 6 M guanidinium hydrochloride or 2% SDS to remove either species. The occupancy ranges of heme B and PPIX with Orf13 may indicate this enzyme

to have similar binding affinities for both porphyrin moieties. The lack of *in vivo* binding discrimination between heme B and PPIX may also suggest stronger binding interactions with protein residues and substituents of porphyrin ring (i.e. the propanoic acid or vinyl groups) than the axial residue(s) coordinating the heme-iron.

The extensive variability in heme B occupancy for Orf13 was observed in expression batches from the same seed culture, prepared in the same liquid media, and grown and expressed on the same shaker using identical flasks. Heme dependent enzymes obtained from *E. coli* expression systems that require a non-covalently bound heme exist largely in an apo-form with partial heme occupancy and without the presence of PPIX (*51-53*). Complete heme occupancy can be readily achieved by addition of heme to the enzyme by titration without the need for protein denaturation and refolding. *In vitro* titration of heme B to purified Orf13 did not exchange the bound PPIX and the enzyme remained fully occupied with a heterogeneous mixture of both porphyrin species. Attempts to obtain an apo-form of Orf13 for *in vitro* heme titration was also unsuccessful since the enzyme failed to express when 1,10-phenanthroline, a metal chelating agent, was added to the growth medium. In an effort to increase and control the *in vivo* incorporation of heme B in Orf13, δ-aminolevulinic acid (δ-ALA, a heme biosynthetic precursor (*54*)), exogenous non-heme iron (such as iron (II) sulfate ($FeSO_4$) or ammonium iron (II) sulfate, Mohr's salt ($(NH_4)_2Fe(SO_4)_2{\cdot}6H_2O$)) with or without δ-ALA, or exogenous hemin were added to the medium for expression in BL21(DE3) *E. coli*. This strategy was ineffective as similar results in heme B occupancy (30-100%) were observed compared to Orf13 expression without any additives. It was also determined that the range in heme B and PPIX occupancies with Orf13 is independent of the

purification method. Purification of Orf13 by anionic exchange (Q-Sepharose) in the presence of excess DTT (50 mM) to protect Orf13 from auto-oxidative degradation showed the same variable heme B occupancies as the metal affinity method (Ni-Sepharose). This confirmed that heme B bound to Orf13 was not compromised, lost or competed out due to the enzyme's ability to intrinsically bind to the Ni-Sepharose resin.

An alternative *E. coli* expression system for *in vivo* incorporation of heme B in Orf13 was also tried using RP523 *E. coli* with exogenous hemin. RP523 is a porphyrin permeable strain of *E. coli* with a mutation in the *hemB* gene of the heme biosynthetic pathway that disrupts the normal biosynthesis of heme B. Therefore, RP523 cells are dependent on the uptake of exogenous heme B for survival (*55*). This expression system has been established for substituting nitric oxide synthase (NOX), a heme dependent enzyme, with different metalloporphyrins (*39, 56*). The advantage in utilizing this system for Orf13 expression is that these cells lack the ability to synthesize porphyrin and are only viable in the presence of heme B, thus eliminating the presence of PPIX with Orf13. RP523 *E. coli* cells expressing Orf13 using the pCW/*orf13* construct were red in color as observed with Orf13 expression in BL21(DE3) *E. coli*. However, it was difficult to obtain stable Orf13 using the developed purification methods previously described. Severe degradation of Orf13 was evident after the Ni-Sepharose method in the presence of imidazole. Orf13 eluted as a brownish-yellow enzyme and showed auto-oxidative degradation by SDS-PAGE with a predominant protein band at double the monomeric weight of Orf13 that was commonly observed in purifications of Orf13 from BL21(DE3) *E. coli* without oxidative protection (Refer to Figure 2-2A, lane 5). Repeating the Ni-Sepharose purification under anaerobic conditions in a glove box prevented dimerization

of Orf13 and the enzyme retained its red color. The visible absorption spectrum of heme B bound to Orf13 was similar to Orf13 purified from BL21(DE3) *E. coli* (Refer to Figure 2-3). However, the overall yield and purity were very poor. Purification by the Q-Sepharose method with excess DTT (50 mM) prevented covalent dimerization and improved the purity of the protein sample. However, Orf13 eluted as a bright yellow enzyme with an unusual visible absorption spectrum of the heme displaying a broad Soret band at 420 nm without distinguishable Q-bands. In addition, the heme species bound to Orf13 could not be reduced by dithionite to assess its heme B stoichiometry by the pyridine hemochromagen method. Overall, the feasibility of obtaining sufficient amounts of highly pure and stable Orf13 fully occupied with heme B from RP523 *E. coli* was unsuccessful and proved more challenging than the purification of Orf13 expressed in BL21(DE3) *E. coli*.

Full heme B incorporation into native Orf13 was finally achieved with BL21(DE3) *E. coli* expression of the protein in the presence of ferric iron (III) citrate. Use of this iron chelate as an additive during expression consistently results in Orf13 with an average heme B occupancy of 102 ± 11%. This is a outstanding result compared to the previous attempts with other exogenous non-heme iron additives which had produced variable heme B occupancies (30-100%). The success of ferric iron (III) citrate over other iron chelate forms is directly related to the iron metabolism of *E. coli*. There is an intrinsic ferric iron citrate transport mechanism in *E. coli* that is one of several pathways for exogenous iron uptake essential for iron metabolism (*57*). Iron (III) citrate acts as its own signaling molecule and is taken up by the bacteria, increasing the effective concentration of iron in the cell that can be utilized by other metabolic pathways. Thus, it

is plausible that more iron is available for the final step of heme biosynthesis when ferrochelatase inserts an iron atom into PPIX to produce heme B. The resulting outcome is the complete occupation of native Orf13 with heme B. The BL21(DE3) *E. coli* cells transformed with pET24a/*orf13* are grown in the presence of iron (III) citrate in the expression media; after inoculation from the seed culture and all the way through until the cells are harvested after induction with D-lactose. All other expression conditions and observations, including the average cell growth rate, remain the same as previously described. Moreover, expression of native Orf13 in the presence of iron (III) citrate allows full *in vivo* incorporation of heme B. The predominant secondary structure conformation of Orf13 with 100% heme B is alpha-helical with an absorbance maximum at +190 nm and minima at -210 nm and -222 nm (Figure 2-7). This is common among heme containing proteins (*58, 59*).

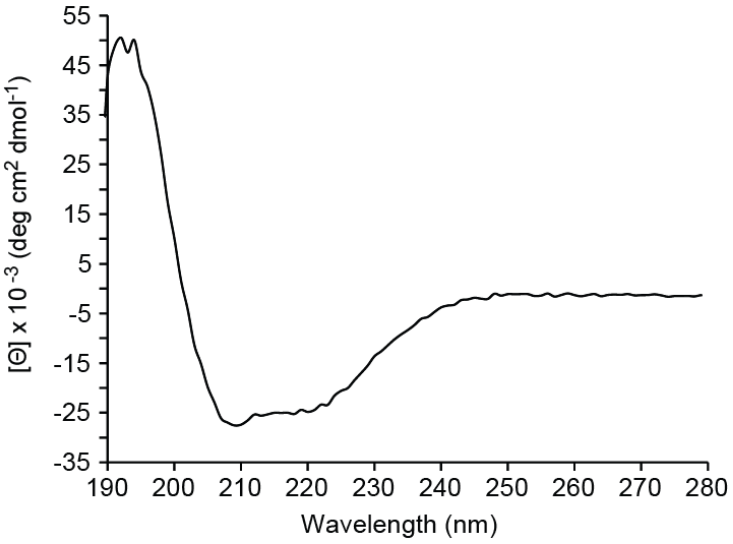

Figure 2-7. Far-UV circular dichroism spectrum of Orf13 (100% heme B) in 20 mM sodium phosphate (pH 8.0) at 25 °C.

Chapter 3: Functional characterization of Orf13 and classification as a heme peroxidase

3.1 Introduction

The identification of heme B with purified native Orf13 suggests that this enzyme may be a heme dependent tyrosine hydroxylase. No other organic cofactors were identified with Orf13 and no other metals, other than iron originating from heme B, had been found by ICP-MS. This information excludes classification of Orf13 as any of the non-heme dependent MMOs, in particular, the non-heme iron pterin or α-KG dependent enzymes and the copper dependent tyrosinases that catalyze the *ortho*-hydroxylation of L-tyrosine to L-DOPA (*33, 34*). The heme dependent MMO class includes two types of enzymes; the cytochrome P450 enzymes and heme peroxidases. To assess the catalytic requirement of heme B for Orf13 as a putative tyrosine hydroxylase, the reaction requirements and catalytic cycles of cytochrome P450s and heme peroxidases were considered.

Cytochrome P450 enzymes catalyze aromatic hydroxylation by the transfer and insertion of an oxygen atom into an aromatic substrate, where the oxygen source is dioxygen (O_2; molecular oxygen) (Figure 3-1) (*29, 59*). Binding and activation of dioxygen during the catalytic cycle only occurs after an aromatic substrate binds to the enzyme in the ferric resting state and the ferric heme-iron is reduced by 1-electron to the ferrous state. This first electron originates from NAD(P)H that is supplied through a

flavin ferredoxin domain or by a FMN reductase (*60, 61*). The ferrous-dioxygen complex can accept a second electron from NAD(P)H through an electron transfer system to produce a ferric peroxy-anion species which is protonated to form Compound 0, the ferric hydroperoxy complex. Heterolytic cleavage between the oxygen atoms generates Compound I, a radical oxo-ferryl intermediate, which then inserts the oxygen atom into the aromatic substrate by a proposed oxygen rebound mechanism (*62-64*). This returns the heme-iron to the ferric resting state and the hydroxylated product dissociates to complete the catalytic cycle.

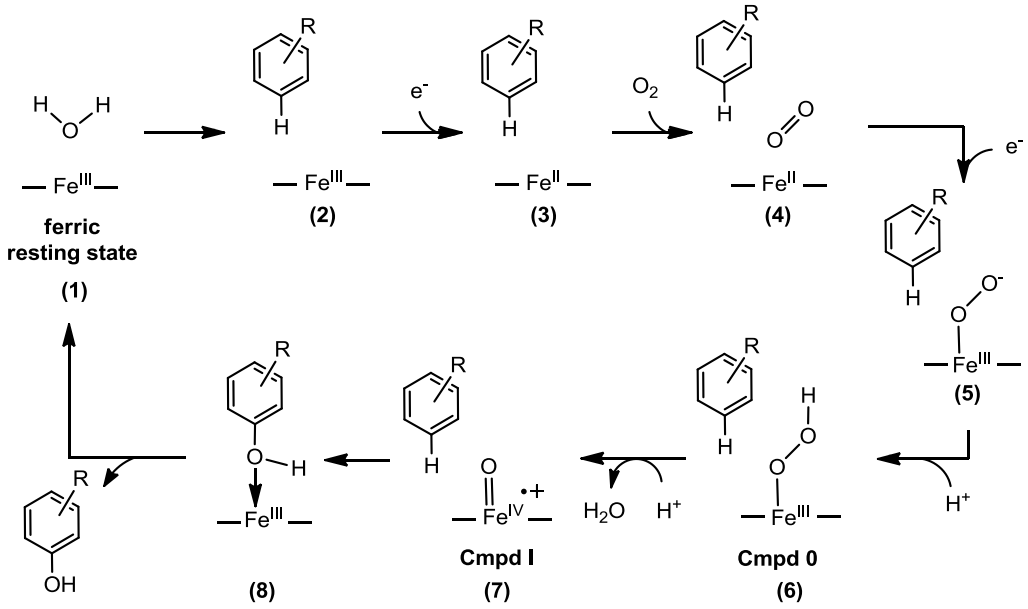

Figure 3-1. The consensus mechanism of aromatic hydroxylation for cytochrome P450 catalysis; (1) native ferric enzyme resting state occupied with water, (2) ferric heme-substrate complex, (3) ferrous heme-substrate complex, (4) ferrous-dioxygen complex, (5) ferric peroxy-anion complex, (6) ferric hydroperoxy complex (Compound 0), (7) oxo-ferryl radical complex (Compound I), (8) product-ferric complex.

The main catalytic function of heme peroxidases is the oxidation of aromatic substrates by 2-sequential 1-electron transfer reactions with hydrogen peroxide (Figure 3-2) (*29, 31, 65*). In the catalytic cycle, hydrogen peroxide is used directly to generate

Compound 0 from the ferric resting state. It is not obligatory for an aromatic substrate to bind prior to hydrogen peroxide in order to generate this intermediate. Heterolytic cleavage of the O-O bond generates Compound I, a radical oxo-ferryl intermediate, which can complete the first 1-electron transfer reaction to an aromatic substrate to generate a radical product. Compound I is converted to Compound II, an oxo-ferryl intermediate, which can react with a second aromatic substrate to generate another radical product to complete the second 1-electron transfer reaction and return the enzyme to the ferric resting state. Overall, one reaction cycle produces two 1-electron oxidized aromatic products without the transfer of oxygen, and hydrogen peroxide is converted into 2 water molecules. While both heme peroxidases and cytochrome P450s are classified as oxidoreductases (EC 1.x.x.x) (*66*) and show similarities in their catalytic cycles, heme peroxidases do not catalyze aromatic hydroxylation with hydrogen peroxide.

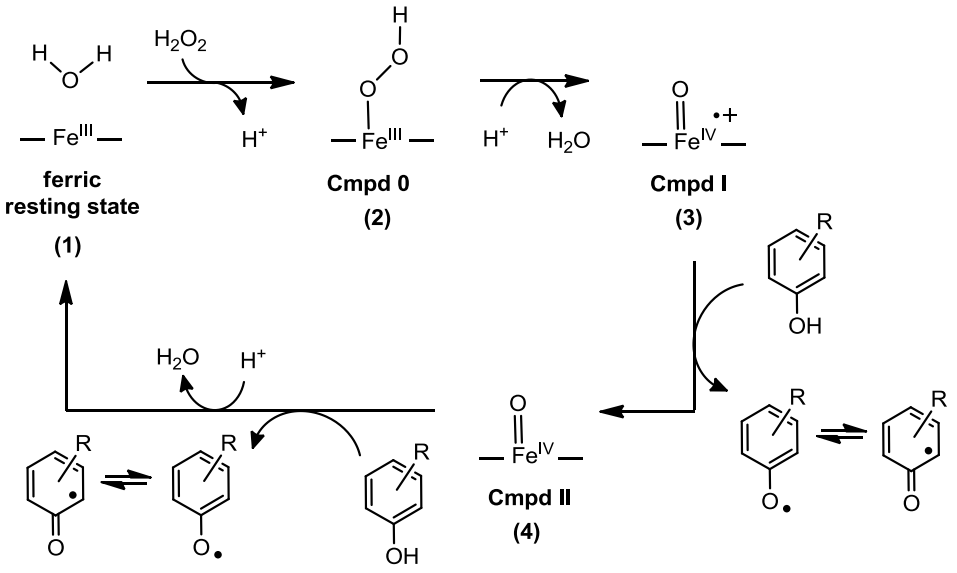

Figure 3-2. The catalytic cycle of heme peroxidase for the oxidation of phenol; (1) native ferric enzyme resting state occupied with water, (2) ferric hydroperoxy complex (Compound 0), (3) oxo-ferryl radical complex (Compound I), (4) oxo-ferryl complex (Compound II).

Another important feature that generally distinguishes cytochrome P450s and heme peroxidases is the residue that coordinates the heme-iron in the axial position. This residue is known as the proximal or 5th ligand and is highly conserved. The proximal (5th) ligand in cytochrome P450s is a cysteine (most common) or methionine residue, where the heme-iron coordination is referred to as thiolate-ligated (*29, 59*). Classical heme peroxidases are histidyl-ligated where a histidine residue acts as the proximal (5th) ligand (*29, 31, 65, 67*).

Knowledge of the reaction requirements and catalytic cycles of cytochrome P450s and heme peroxidases provided the initial conditions in which to assess the catalytic requirement of heme B in Orf13. The key sequence of objectives in the functional characterization of Orf13 was 1) to determine whether the enzyme is active and catalyzes L-tyrosine hydroxylation, 2) to determine the reaction conditions needed for catalysis, and 3) assign the classification of the enzyme based on the reaction requirements.

3.2 Experimental Procedures

Materials. Sodium phosphate, imidazole, sodium dithionite, and hydrogen peroxide (30% solution) were purchased with the highest purity from ThermoFisher Scientific (Fair Lawn, NJ). Dithiothreitol (DTT) was purchased from American Bioanalytical Inc. (Natick, MA). Catalase, superoxide dismutase (SOD) and all other chemicals were purchased with the highest purity from Sigma Aldrich (St. Louis, MO). Carbon monoxide gas, CO (g), was kindly provided by the laboratory of Professor Eichhorn (University of Maryland, College Park, MD).

General Methods. All UV-visible absorption spectra or measurement of catechol-nitrite complexes for kinetic assays were obtained with a Varian UV-vis Cary100 Spectrophotometer with Temperature Controller (Walnut Creek, CA). High performance liquid chromatography was performed with an Agilent 1000 Series HPLC (Foster City, CA) equipped with an 1100 Series multiple wavelength detector and 1200 Series fluorescence detector. Anaerobic experiments were performed in an 830-ABC series compact glovebox (PLAS-LABS, Inc; Lansing, MI) equipped with a Model 10 Gas Analyzer and Digital Heated Fan Box with palladium catalyst bed (Coy Laboratory Products, Inc; Grass Lake, MI).

Orf13 activity assays by HPLC-FLD for the detection of L-tyrosine and L-DOPA. For assays assessing molecular oxygen dependent tyrosine hydroxylation, Orf13 (2.5 μM) was pre-incubated in 50 mM sodium phosphate (pH 8.0) containing 15 mM DTT or 15 mM dithionite for 5 min on ice and then incubated for 5 min at 37 °C before addition of L-tyrosine (1 mM final) to start the reaction. In assays testing the requirement of hydrogen peroxide, Orf13 was pre-incubated with L-tyrosine (1 mM final) for 5 min on ice, 5 min at 37 °C and then hydrogen peroxide (0.1 mM final) was added to initiate the reaction. All assays were performed at 37 °C up to 15 min in triplicate. Four time point aliquots (75 μL) were quenched with 2.5 M HCl (10 μL) and chloroform (40 μL) was added to the quenched samples, spun at 3,400 rpm for 2 min at room temperature. The aqueous layer (65 μL) was transferred to new tube containing 2.5 M NaOH (10 μL). Each sample (20 μL) was analyzed by HPLC-FLD as described for the detection of L-tyrosine and L-DOPA (*68*). L-Tyrosine and L-DOPA stocks were quantified spectrophotometrically at ε_{275} = 1.4 mM^{-1} cm^{-1} (*69*) and ε_{280} = 2.63 mM^{-1} cm^{-1} (*70*),

respectively. L-DOPA and L-tyrosine standards had average retention times of 4.5 and 5.5 minutes, respectively. The amount of L-DOPA produced by Orf13 was determined based on a calibration curve of L-DOPA made with standard samples quantified spectrophotometrically and treated under the same sample work up condition described. In Orf13 specific activity assays for the dihydroxyfumaric acid (DHFA) or L-ascorbate dependent reactions, Orf13 (2.5 μM) was pre-incubated with DHFA (2 mM) or L-ascorbate (25 mM) for 5 min on ice and then 5 min at 37 °C in 100 mM sodium phosphate (pH 8.0). The reaction was initiated by addition of L-tyrosine (5 mM) and carried out for 15 min with time point aliquots quenched, prepared and analyzed as described above. These assays were performed in triplicate with or without catalase (75 μg/mL) or superoxide dismutase (SOD) (100 μg/ml), or were performed in an anaerobic glove box. L-Ascorbate stocks were quantified spectrophotometrically at $\varepsilon_{290} = 2.8\ mM^{-1}\ cm^{-1}$ (*71*).

Steady-state kinetics of L-tyrosine hydroxylation by Orf13. A discontinuous assay was developed to monitor formation of L-DOPA in the hydrogen peroxide dependent reaction of Orf13 using a colorimetric method previously described (*72, 73*). Orf13 (0.3 – 1 μM; 75% heme B occupancy) was incubated with L-tyrosine for 5 minutes at 37 °C in 100 mM sodium phosphate (pH 8.0), followed by addition of hydrogen peroxide to initiate the reaction. Assays were performed in triplicate at 37 °C for 4 min with time points taken at 1, 2, 3, and 4 min in 90 μL aliquots quenched with 2.5 M HCl (10 μL). A solution containing 12.5% (w/v) sodium nitrite and 12.5% (w/v) sodium molybdate (35 μL) was added to the quenched samples and incubated for 10 min at room temperature. NaOH (10 μL, 3 M) was added to the sample and the L-DOPA-nitrite

complex was measured at 500 nm within 10-15 seconds. A standard curve of L-DOPA from 1 to 100 μM was prepared the same day for each set of assays. L-tyrosine and L-DOPA stocks were quantified as previously described (*69, 70*). Hydrogen peroxide stocks were prepared fresh and quantified spectrophotometrically at $\varepsilon_{240} = 43.6\ M^{-1}\ cm^{-1}$ (*71*). Fixed variable concentrations of L-tyrosine (125 μM to 5 mM) at a fixed concentration of hydrogen peroxide (500 μM) were used to determine the steady-state kinetic parameters for L-tyrosine. Fixed variable concentrations of hydrogen peroxide (100 μM to 1 mM) at a fixed concentration of L-tyrosine (2 mM) were used to determine the steady-state kinetic parameters for hydrogen peroxide. The steady-state data for both L-tyrosine and hydrogen peroxide were fit to the Michaelis-Menten equation (Equation 3-1) using the software program Prism 4 (GraphPad) to obtain the steady-state rate constants; $v_o/[E_t]$ is the initial velocity of an enzyme normalized by the total enzyme concentration, $[E_t]$, in the steady-state assays, k_{cat} is the maximal velocity macroscopic and catalytic rate constant, [S] is the concentration of the fixed varied substrate, and K_m is the Michaelis-Menten constant which represents the concentration of the fixed varied substrate required to reach half-maximal velocity.

Equation 3-1.

$$v_o/[E_t] = k_{cat}[S]/K_m + [S]$$

Assay controls with a blank solution without Orf13 were used to correct for background. Orf13 background control assays were carried out with the same concentration of enzyme in the absence of substrates. No enzyme background at 500 nm was observed with 1.5 μM Orf13 or less. All controls were run in triplicate and in parallel with assay samples, and underwent the same colorimetric workup described above. For

all described specific activity and steady-state kinetic data, Orf13 was purified and stored in buffer B (10 mM imidazole, 50 mM sodium phosphate (pH 8.0), 300 mM NaCl and 10% glycerol) to maintain stable enzyme with a ferric heme-iron oxidation state. Orf13 purified and stored in the presence of 50 mM DTT was buffer exchanged into buffer B at 4 °C using a G-50 column (1 x 5 cm; 4 mL CV) to remove DTT prior to enzyme assays. Auto-oxidation of the heme-iron to the ferric state upon buffer exchange was observed by a shift of the Soret band from 420 nm to 405 nm (Refer to Figure 2-6).

Reduced-CO (g) spectrum of Orf13. A visible spectrum of Orf13 (4 μM) with 100% heme B occupancy in 20 mM Tris-HCl (pH 8.0), 10 mM imidazole and 10% glycerol was initially measured to obtain a spectrum of the enzyme in the ferric resting state. Sodium dithionite (1-3 grains) was directly added to the sample; the quartz cuvette was sealed immediately with a small rubber stopper and then gently mixed. In a chemical fume hood, a syringe attached to a balloon filled with carbon monoxide gas (CO (g)) and a syringe to vent the sample were attached to the sealed cuvette. The sample was purged with CO (g) for 3 min and then a visible spectrum was measured to obtain the reduced-CO (g) spectrum of Orf13. Note: a visible spectrum of the reduced sample after addition of dithionite was measured for comparison with the reduced-CO (g) spectrum to ensure sufficient CO (g) was present and bound to the reduced heme-iron.

X-band Electron Paramagnetic Resonance (EPR) of ferric Orf13. Orf13 with 50% heme B occupancy purified and stored in the presence of 50 mM DTT was buffer exchanged into 20 mM sodium phosphate (pH 8.0) at 4 °C using a G-50 column (1 x 5 cm; 4 mL CV). Auto-oxidation of heme B to the ferric state was observed after removal of DTT; however, ferricyanide (5 mM) was also added to Orf13 to ensure complete

oxidization of the heme-iron to the ferric state. The ferricyanide was removed from the sample by a second G-50 column (1 x 5 cm; 4 mL CV) pre-equilibrated with 20 mM sodium phosphate (pH 8.0) at 4 °C. The final Orf13 sample was concentrated to 6 mg/mL, diluted 1:1 (v/v) in 100% glycerol (300 µL final volume), transferred to an EPR quartz tube (250 mm length, 0.5 mm thickness, 4 mm O.D., Wilmad Lab Glass; Vineland, NJ) and flash frozen slowly in liquid nitrogen. This sample was stored at -80 °C until EPR analysis. The EPR spectrum of Orf13 was obtained in the Department of Chemistry at Johns Hopkins University using a Bruker EMX EPR spectrometer controlled with a Bruker ER 041 X G microwave bridge at 15 K. The instrument was equipped with a continuous-flow liquid helium cryostat (ESR900) coupled to a temperature controller (TC503) made by Oxford Instruments, Inc.

3.3 Results and Discussion

Catalytic assessment of heme B in Orf13 for L-tyrosine hydroxylation. Orf13 was not expected to be a heme dependent cytochrome P450-like enzyme since there are no conserved cysteine or methionine residues found in the multiple sequence alignment with its homologues (Figure 1-6). This was confirmed when DTT or dithionite reduced Orf13 in the presence of L-tyrosine did not produce L-DOPA. The production of L-DOPA was observed by HPLC-FLD when hydrogen peroxide was added to Orf13 in the presence of L-tyrosine (See Appendix A-6). This implicated the catalytic requirement of heme B. The HPLC-FLD assay method provided initial clues for catalytic activity, but was not used to further evaluate the hydrogen peroxide dependent reaction due to the limited sensitivity of the HPLC-FLD analysis. A modified discontinuous assay for spectrophotometric detection of L-DOPA in a DOPA-nitrite colorimetric complex (*72,*

73) was utilized to measure the specific activity and steady-state kinetics of Orf13. As part of the assay optimization process to observe turnover, the substrate order was evaluated under 3 different pre-incubation and reaction initiation conditions (Figure 3-3). Two important observations were made from this pre-incubation study: 1) maximal turnover occurs when Orf13 is pre-incubated with L-tyrosine followed with reaction initiation by addition of hydrogen peroxide, and 2) product formation begins to plateau after 3 minutes during the time course under the initial conditions tested.

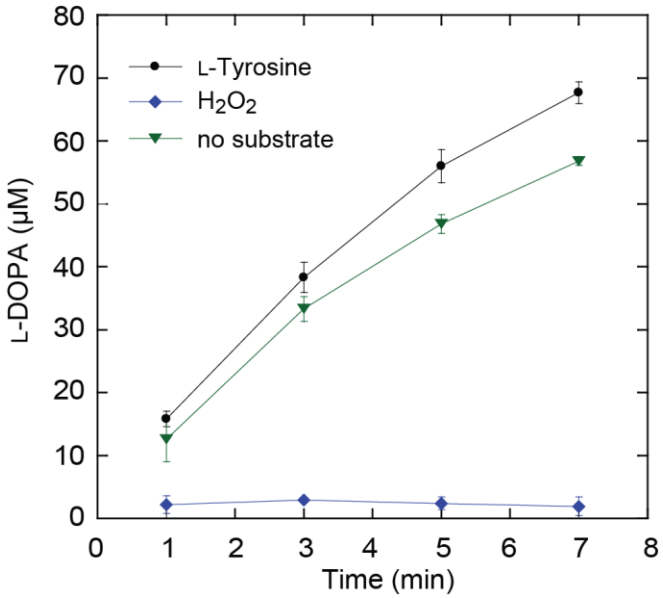

Figure 3-3. Progress curves of the L-tyrosine hydroxylation reaction by Orf13 under different substrate pre-incubation conditions. Assay conditions: 0.5 μM Orf13, 1 mM L-tyrosine, and 400 μM H_2O_2 in 100 mM sodium phosphate (pH 8.0) at 37 °C. Orf13 (75% heme B) was pre-incubated 5 min at 37 °C with L-tyrosine (●), hydrogen peroxide (♦) or alone (▼). Reactions were initiated by addition of the substrate(s) not included during pre-incubation. L-DOPA formation was measured by the L-DOPA colorimetric assay. Data interpolation is shown beyond the time range for initial rate measurements. Figure was modified from Connor, KL et al (*43*).

The optimized enzyme assay conditions to measure the specific activity of Orf13 for the production of L-DOPA include 5 mM L-tyrosine, 500 μM H_2O_2 in 100 mM

sodium phosphate (pH 8.0) with a 4 min time course at 37 °C (See Methods). The specific activity of Orf13 correlated with the stoichiometry of heme B where maximal turnover of ferric-heme Orf13 (100% heme B) is 32 ± 2 min^{-1} compared to 21 ± 1 min^{-1} with ferric-heme Orf13 (48% heme B). The specific activity is also dependent on the heme-iron oxidation state where ferric-heme Orf13 (48% heme B) had greater catalytic activity (21 ± 1 min^{-1}) than Orf13 with ferrous-heme in the presence of 50 mM DTT (9 ± 1 min^{-1}). These data are in agreement with a catalytic starting state of ferric heme-iron for heme peroxidases (*31*) (Figure 3-2). Moreover, these results establish heme B as the cofactor required for catalysis and classify Orf13 as a heme dependent peroxidase catalyzing the *ortho*-hydroxylation of L-tyrosine to L-DOPA.

Steady-state kinetics of Orf13. The steady-state kinetic parameters for L-tyrosine and hydrogen peroxide were determined using the L-DOPA colorimetric assay and the pre-incubation condition of Orf13 with L-tyrosine prior to reaction initiation by addition of hydrogen peroxide (Table 3-1; See Appendix A-7 and A-8 for Michaelis-Menten analysis). The steady-state rate constants for hydrogen peroxide were also determined at two other fixed concentrations of L-tyrosine (5 mM and 0.45 mM) since saturation of hydrogen peroxide could not be achieved within the limits of the colorimetric assay (See Appendix A-9). Hydrogen peroxide at concentrations greater than 1 mM affects the stability and reactivity of the molybdenum-nitrite colorimetric solution and also degrades L-DOPA, the product detected in the assay. The Michaelis-Menten analysis for the steady-state rate constants of hydrogen peroxide at the fixed concentrations of L-tyrosine listed above were within error of the original steady-state analysis at 2 mM L-tyrosine, which is reported in Table 3-1.

Table 3-1. Steady-State Kinetic Parameters for L-Tyrosine Hydroxylation by Orf13[a]

Variable Substrate	Fixed Substrate	K_m[b] (mM)	k_{cat} (s^{-1})	k_{cat}/K_m (s^{-1} M^{-1})
L-Tyrosine	H_2O_2	0.45 ± 0.04	0.576 ± 0.005	(1.2 ± 0.1) x 10^3
H_2O_2	L-Tyrosine	1.0 ± 0.3	1.5 ± 0.3	(1.5 ± 0.2) x 10^3

[a]Assays were performed at 37 °C with 0.3 – 1 μM Orf13 (75% heme B occupancy) in 100 mM sodium phosphate (pH 8.0). L-DOPA formation was measured using the L-DOPA colorimetric assay. Data are not normalized to heme B occupancy.
[b]These values are apparent K_m constants at a partially saturating concentration of hydrogen peroxide (500 μM) and saturating concentrations of L-tyrosine (2 mM).

The steady-state kinetic parameters for L-tyrosine hydroxylation by Orf13 fit to the Michaelis-Menten model are within the range of values reported for other heme peroxidases (*74*) and the catalytic efficiency for both substrates is similar. While comparison of the steady-state rate constants can be made to some extent based on use of a common cofactor (heme B) and requirement of hydrogen peroxide for catalysis, the overall products of these reactions are different. Orf13 hydroxylates L-tyrosine to L-DOPA whereas classical heme peroxidases perform 2-sequential 1-electron oxidizations of aromatic substrates. Orf13 is the first heme peroxidase known to perform hydrogen peroxide dependent aromatic hydroxylation (*43*), and has the potential to establish a different mechanism.

Reaction dependent behavior of Orf13 for L-tyrosine hydroxylation. Tyrosine hydroxylation to L-DOPA by Orf13 is also observed in the presence of L-ascorbate or dihydroxyfumaric acid (DHFA) (See Appendix A-10). The ascorbate and DHFA dependent reactions require molecular oxygen and have similar k_{obs} that are 48 and 58 fold less than the k_{obs} of the hydrogen peroxide dependent reaction, respectively (Table 3-2). Aromatic hydroxylation by the DHFA dependent reaction was abolished in the

presence of SOD, a superoxide scavenging enzyme, and was not observed with catalase. The ascorbate dependent reaction was not affected by SOD and decreased 4 fold in the presence of catalase. Interestingly, hydroxylation of phenols has been reported for horseradish peroxidase (HRP) in the presence of DHFA as an oxygen transfer reaction similar to cytochrome P450 enzymes (*36, 37*). The peroxygenase activity of HRP is promoted by non-enzymatic production of superoxide by DHFA and molecular oxygen, which then causes the formation of Compound III, an oxyferrous heme-iron state, when superoxide binds to the heme. Hydroxylation of phenol only occurs when substrate and additional reducing equivalents of DHFA are present with HRP-Compound III (*36*). Hydroxylation of L-tyrosine to L-DOPA by Orf13 in the presence of DHFA is in agreement with the HRP peroxygenase activity for aromatic hydroxylation. Although molecular oxygen dependent hydroxylation of L-tyrosine by Orf13 in the presence of ascorbate or DHFA is observed, it does not appear to be the primary catalytic pathway for L-tyrosine hydroxylation since turnover is enhanced 48 and 58 fold, respectively, when hydrogen peroxide is provided as a substrate for the hydroxylation reaction (Table 3-2). Additionally, similar rate enhancement is observed with hydrogen peroxide in the absence of molecular oxygen under anaerobic conditions.

Table 3-2. Reaction Dependent Behavior of Orf13 for L-Tyrosine Hydroxylation

Assay Condition[a,b]	k_{obs} (min^{-1})[c]	Rel Percentage[d]
Orf13	None	0
Orf13 + H_2O_2	34 ± 4	100
Orf13 + H_2O_2 - O_2	33 ± 3	98
Orf13 + H_2O_2 + catalase (75 μg/mL)	1.6 ± 0.2	5
Orf13 + H_2O_2 + SOD (100 μg/mL)	26.5 ± 0.6	78
Orf13 + AscA	0.58 ± 0.01	1.7
Orf13 + AscA - O_2	None	0
Orf13 + AscA + catalase (75 μg/mL)	0.15 ± 0.01	0.5
Orf13 + AscA + SOD (100 μg/mL)	0.6 ± 0.1	1.7
Orf13 + DHFA	0.69 ± 0.06	2
Orf13 + DHFA - O_2	None	0
Orf13 + DHFA + catalase (75 μg/mL)	None	0
Orf13 + DHFA + SOD (100 μg/mL)	None	0

[a]Abbreviations: Tyrosine Hydroxylase (Orf13), hydrogen peroxide (H_2O_2), molecular oxygen (O_2), L-ascorbate (AscA), dihydroxyfumaric acid (DHFA), superoxide dismutase (SOD).
[b]Final assay concentrations: 0.5 or 2.5 μM Orf13 (75% heme B occupancy), 5 mM L-tyrosine in 100 mM sodium phosphate (pH 8.0) at 37°C; 25 mM AscA, 2 mM DHFA or 500 μM H_2O_2 as indicated by assay condition. L-DOPA detected by L-DOPA colorimetric assay for H_2O_2 dependent reactions and by HPLC-FLD for AscA and DHFA dependent reactions.
[c]k_{obs} measured as μmol of L-DOPA min^{-1}; mean and standard deviation reported.
[d]Relative percentage is based on Orf13 + H_2O_2 condition where maximal turnover is observed.

Substrate order for catalysis and inactivation by hydrogen peroxide. Heme peroxidases typically bind hydrogen peroxide first, although the heme-iron can become trapped in a non-productive oxyferrous state (Compound III) during the catalytic cycle (*31*). Characteristic bands for Compound III in HRP include a Soret band at 417 nm and Q-bands at 544 nm and 580 nm (*75*). For Orf13, reversed substrate order of addition is necessary for catalysis with maximal tyrosine hydroxylation occurring by pre-incubation with L-tyrosine prior to the addition of hydrogen peroxide (Figure 3-3). No turnover is observed if hydrogen peroxide is incubated with Orf13 before the addition of L-tyrosine. UV-visible absorption scans of Orf13 were taken before and after addition of hydrogen

peroxide in the absence of L-tyrosine to investigate whether the lack of catalysis by the hydrogen peroxide Orf13 complex is due to formation of Compound III (Figure 3-4). The spectrum measured in the presence of hydrogen peroxide shows a significant decrease in the Soret band intensity and disappearance of the Q-bands at 503 nm and 630 nm that is unlike the characteristic spectrum of HRP-Compound III. Although the formation of Compound III has been shown to be stable in HRP for at least five minutes (*75*), this heme-iron species may be transient with Orf13. This may suggest a different hydrogen peroxide inactivation mechanism for Orf13.

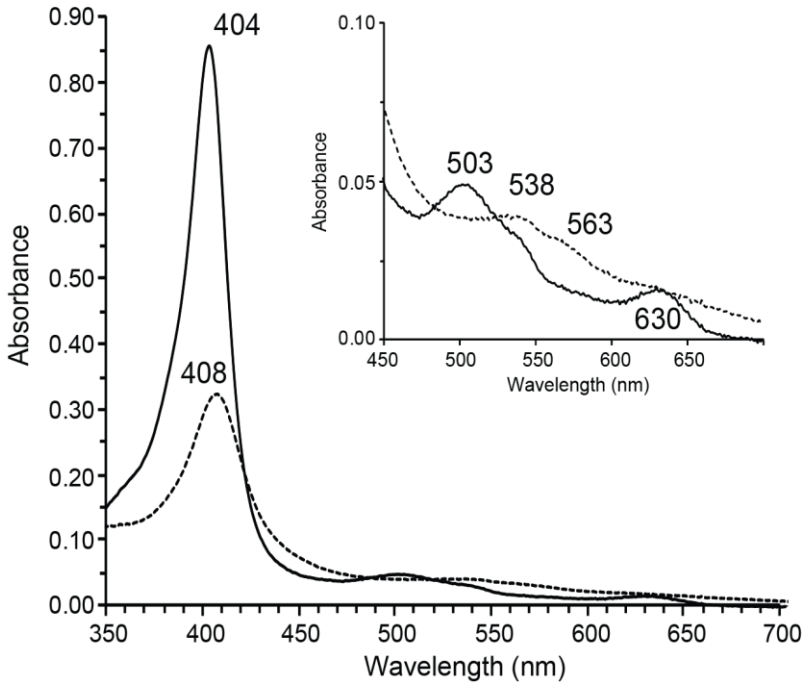

Figure 3-4. UV-visible absorption spectra of Orf13 (4 μM; 100% heme B) in the absence (solid line) and presence (dashed line) of 500 μM H_2O_2 in 100 mM sodium phosphate (pH 8.0) at room temperature. Figure was modified from Connor, KL et al (*43*).

No changes in the heme spectrum were observed by addition of L-tyrosine to Orf13. This may indicate that the role of L-tyrosine as the first substrate added is simply

to protect Orf13 from hydrogen peroxide inactivation since it does not affect the coordination of the heme-iron as observed by the retention of the Q-band at 630 nm (Figure 3-5). Interaction of L-tyrosine at the heme edge is consistent as there are no changes in the heme spectrum and is evident in heme spectra during catalysis after the addition of hydrogen peroxide to Orf13 pre-incubated with L-tyrosine (Figure 3-5).

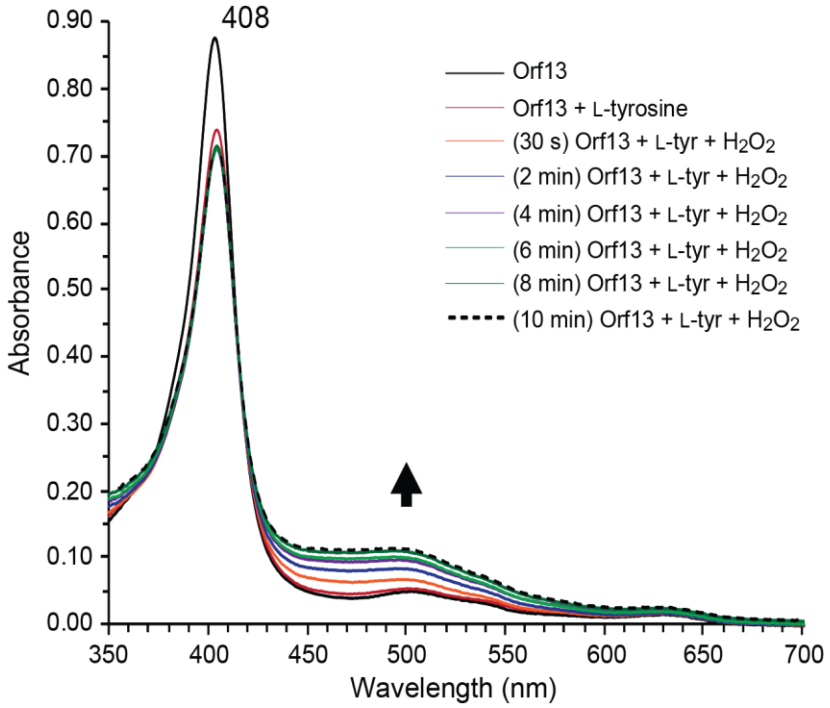

Figure 3-5. UV-visible absorption spectra of Orf13 (100% heme B) with L-tyrosine followed by the addition of hydrogen peroxide. Final experimental conditions: 4 µM Orf13, 5 mM L-tyrosine, 500 µM H_2O_2 in 100 mM sodium phosphate (pH 8.0) at room temperature. The sample was scanned at 2 minute intervals for 10 minutes after the addition of H_2O_2. Figure was modified from Connor, KL et al (*43*).

During catalysis the absorbance intensity from 450 nm to 600 nm, most notable in the Q-band at 503 nm, increased over time up to 6 minutes, after which no more changes were observed. The pattern of absorbance change at 503 nm is similar to what is observed for L-DOPA production by the colorimetric assay when Orf13 is pre-incubated with L-

tyrosine and the reaction initiated with hydrogen peroxide (Figure 3-3). The increase in the 503 nm Q-band is similar to a dehaloperoxidase bound complex with 2,4-dichloroquinone product (*76*) and may indicate an Orf13 product-complex with L-DOPA.

Overall, the severe heme bleaching observed with Orf13 indicates a lack of enzyme stability due to the high reactivity of the heme-iron when in the presence of hydrogen peroxide alone. Inactivation of enzyme activity and/or heme bleaching is not uncommon for heme peroxidases (*71, 77, 78*). Reversed order of substrate addition by pre-incubation of Orf13 with L-tyrosine prior to adding hydrogen peroxide prevents heme bleaching and is necessary for tyrosine hydroxylation, but does not likely reflect a substrate order that is dependent on its catalytic mechanism. While a reversed order of substrate addition may be required to limit enzyme inactivation, as found with heme peroxidases (*71, 77, 78*), the catalytic cycle may occur with the normal peroxidase order of addition with hydrogen peroxide followed by the aromatic substrate (*31, 79*).

Spectroscopy of heme B moiety supports heme peroxidase classification. Additional spectroscopic data to characterize the heme B moiety of Orf13 also provide support in its classification as a heme peroxidase. This is evident by a Soret band position at 421 nm in a reduced-CO (g) spectrum of Orf13 (Figure 3-6). The Soret band position in a reduced-CO (g) spectrum is directly related to redox potential of the heme due to the interaction between the heme-iron and the proximal (5^{th}) ligand that follows the hard-soft acid-base (HSAB) principle (*80, 81*). Historically, this experiment provided the cytochrome P450 name originates since the Soret band is observed at or near 450 nm (*59*). This is due to the soft ligand chemistry between the sulfur atom of cysteine and the heme-iron. However, heme peroxidases have a histidyl-ligated heme-iron and there is

hard ligand chemistry between a nitrogen atom of histidine and the heme-iron. This causes the Soret band to be typically observed at or near 420 nm (*82*). This suggests that Orf13 may have a histidyl-ligated heme-iron, especially since no conserved cysteine or methionine residues are present in the multiple sequence alignment (Refer to Figure 1-6). Furthermore, a low temperature electron paramagnetic resonance (EPR) spectrum of ferric-heme Orf13 shows a predominant high spin heme-iron with a g-value centered at 5.8 (Figure 3-7). Heme peroxidases characteristically have a high spin heme-iron in the ferric resting state with the g-values observed between 4.0 and 6.0 (*83, 84*).

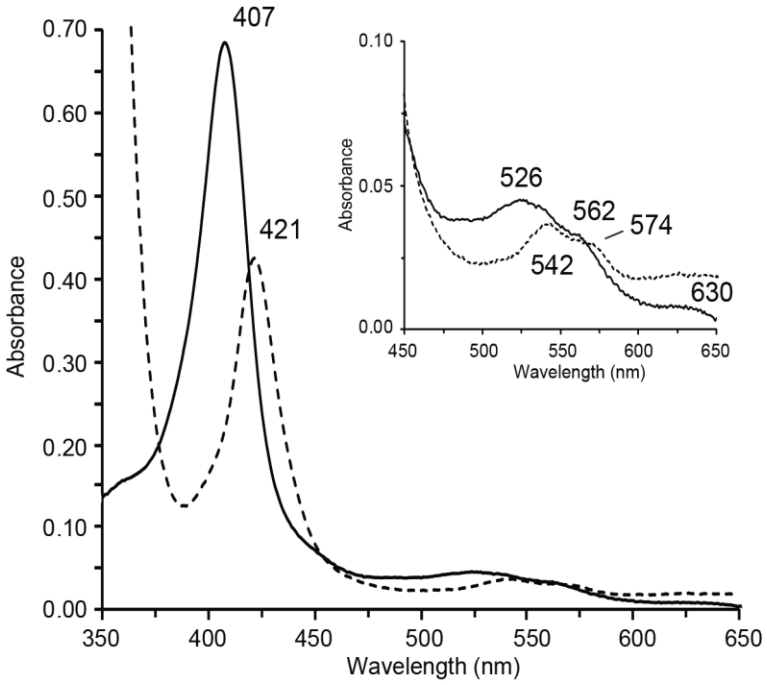

Figure 3-6. UV-visible absorption spectrum of ferric-heme Orf13 (solid line) and ferrous-CO-heme (g) Orf13 (dashed line) with 100% heme B occupancy in 20 mM Tris-HCl (pH 8.0), 10 mM imidazole and 10% glycerol. Figure was modified from Connor, KL et al (*43*).

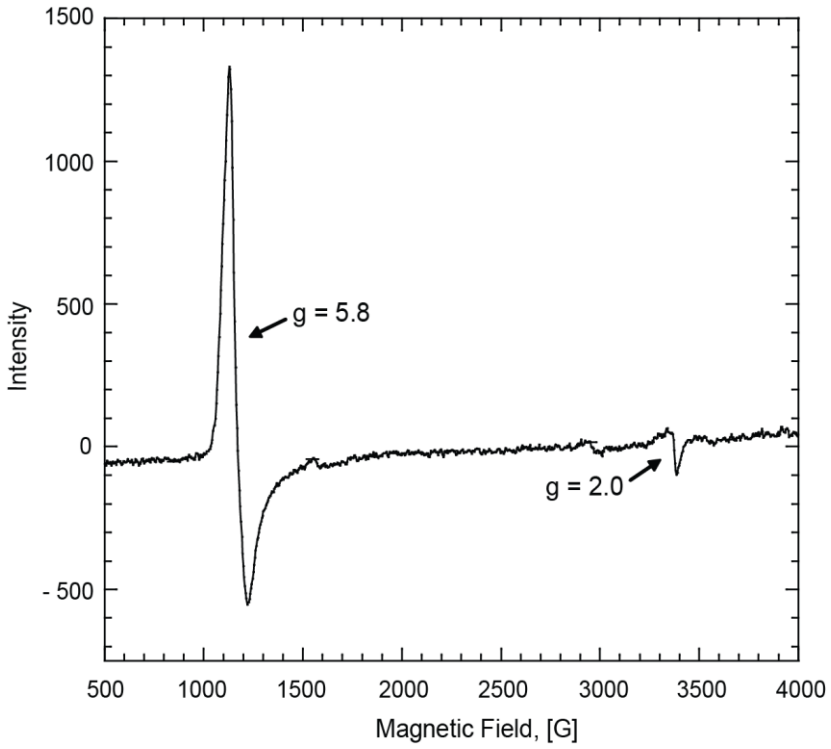

Figure 3-7. X-band EPR spectrum of ferric-heme Orf13 at 15 K. Experimental conditions: 90 μM Orf13 with 50% heme B occupancy (45 μM heme B) in 10 mM sodium phosphate (pH 8.0) and 50% glycerol; frequency, 9.478 GHz; microwave power, 201 μW; modulation frequency, 100 kHz; modulation amplitude, 10.0 G; receiver gain, 5 x 10^3. Figure was modified from Connor, KL et al (*43*).

Conclusion. The identified heme B moiety bound to Orf13 has been established as the required cofactor for catalysis with maximal L-tyrosine conversion to L-DOPA observed in the presence of hydrogen peroxide. The enzyme catalyzes the *ortho*-hydroxylation of L-tyrosine to L-DOPA and has been classified as a heme peroxidase based on the requirements of heme B and hydrogen peroxide. This confirms the putative role of Orf13 as an L-tyrosine hydroxylase catalyzing the first step in the hydropyrrole biosynthetic pathway of the anthramycin (*S. refuineus*). Pre-incubation of L-tyrosine with Orf13 prior to the addition of hydrogen peroxide is required for L-DOPA production. However, the enzyme is inactivated by hydrogen peroxide during catalysis. Steady-state

kinetic analysis of L-tyrosine hydroxylation revealed similar catalytic efficiency for both L-tyrosine and hydrogen peroxide. Similar to heme peroxidases, Orf13 also displays a secondary hydroxylation activity of aromatic substrates in the presence of molecular oxygen and L-ascorbate or DHFA. This behavior is consistent with peroxygenase activity reported with horseradish peroxidase for the hydroxylation of phenol. Spectroscopic data from a reduced-CO (g) UV-visible spectrum of Orf13 and EPR of ferric-heme Orf13 are consistent with heme peroxidases that have a histidyl-ligated heme-iron. Overall, Orf13 establishes the first bacterial class of tyrosine hydroxylases and is the first reported heme peroxidase to perform hydrogen peroxide dependent aromatic hydroxylation. The novelty of this enzyme to catalyze hydrogen peroxide dependent aromatic amino acid hydroxylation has the potential to establish a different mechanism.

Chapter 4: Additional characterization of Orf13 as a novel heme peroxidase and initial investigation of the chemical mechanism of L-tyrosine hydroxylation

4.1 Introduction

Orf13 is a heme dependent enzyme that catalyzes the *ortho*-hydroxylation of L-tyrosine to L-DOPA in the presence of hydrogen peroxide (Figure 4-1A). Its classification as a heme peroxidase is based on the catalytic requirements of heme B and hydrogen peroxide. However, the resulting hydroxylated product of L-DOPA is not in agreement with the 1-electron oxidized products expected for heme peroxidases. The unprecedented novelty of Orf13 to catalyze hydrogen peroxide dependent aromatic amino acid hydroxylation presents the potential to establish a different chemical mechanism than the mechanisms established for cytochrome P450 enzymes (*29, 30, 59, 62*) and heme peroxidases (*29, 31*). Cytochrome P450s catalyze oxygen dependent aromatic hydroxylation (Figure 4-1B) while heme peroxidases catalyze hydrogen peroxide dependent 2-sequential 1-electron transfer reactions (Figure 4-1C). Comparing the net reactions and use of the oxygen source by these two distinct types of heme dependent monophenol monooxygenases suggest that the tyrosine hydroxylation mechanism for Orf13 may fall somewhere in between. The classification of Orf13 as a heme peroxidase begs the question - How similar or dissimilar is this enzyme relative to heme peroxidases?

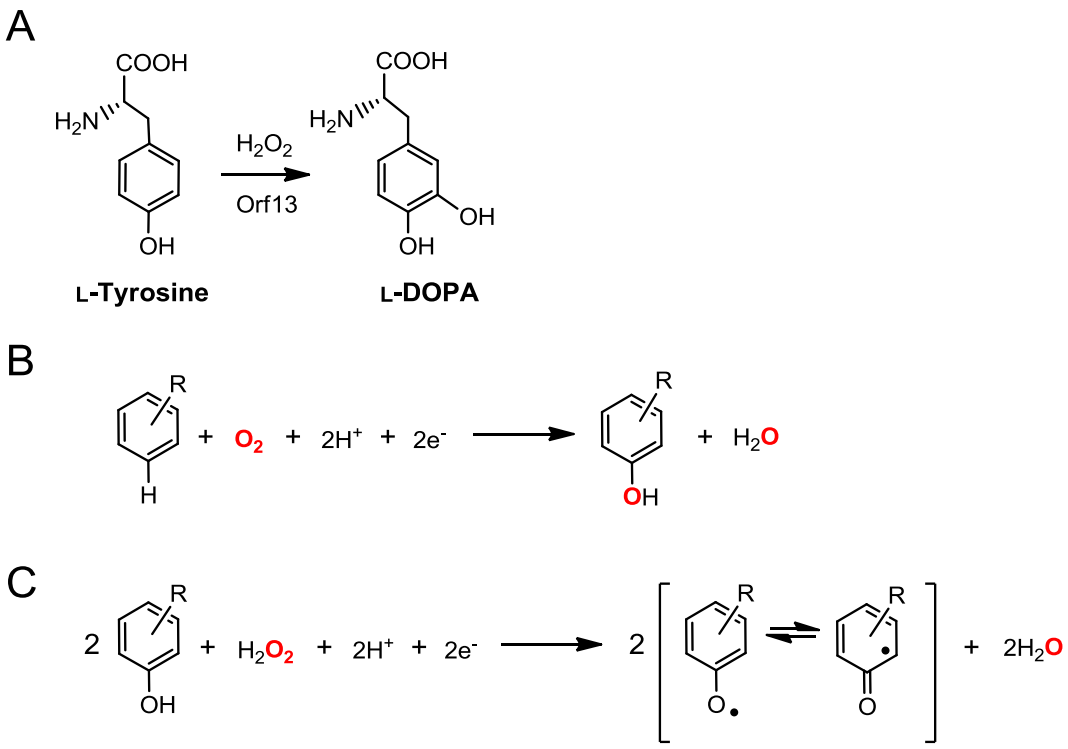

Figure 4-1. (A) L-Tyrosine hydroxylation catalyzed by Orf13 (*S. refuineus*). The net reactions of (B) cytochrome P450s catalyzing aromatic hydroxylation and (C) heme peroxidases catalyzing 2-sequential 1-electron transfer reactions. The oxygen atoms are colored red to indicate their use in the respective heme dependent oxidation reaction pathways.

Comparative sequence analysis of the highly conserved residues in Orf13 to other heme peroxidases based on the spectroscopic data described in Chapter 3, suggests a histidyl-ligated heme-iron. However, Orf13 and its homologs were not initially identified as heme dependent peroxidases by BLAST (*blastp*) analysis nor by the PeroxiBase database (*85*) (http://peroxidase.isb-sib.ch/). Reassessment of the conserved residues in the multiple sequence alignment of Orf13 and its homologs (Figure 4-2) reveals some similarity to the conserved distal site motif $RX_2F(W)H$ characteristic of Class I, II and III peroxidases, which are represented by ascorbate peroxidase, *Arthromyces ramosus* peroxidase and HRP, respectively (*86-89*). The proximal (5^{th}) ligand for these heme

peroxidases is a highly conserved histidine between 120 to 138 residues away from the conserved distal histidine in the $RX_2F(W)H$ motif (*86-89*).

In Orf13, a highly conserved region containing $R^{71}W^{72}X_3H^{76}$ has the same conserved residues as the distal site $RX_2F(W)H$ motif of Class I, II and III heme peroxidases. The similarity in these motifs between unrelated enzymes suggests the evolutionary adaptation for the utilization of hydrogen peroxide for oxidative reactions by heme dependent enzymes. However, residue spacing is different between W72 and H76 for Orf13 than the R and F/W of the heme peroxidase distal site motif. Also, two highly conserved histidine residues (H140 and H184), one of which may act as the proximal (5^{th}) ligand for the heme-iron, are closer in sequence to H76 of the potential distal site by 63 and 107 residues, respectively. These differences in sequence spacing within the potential distal site motif and the proximal histidine may explain why Orf13 was not recognized as a heme peroxidase and might be required for the different reactivity of Orf13 compared to Class I, II and III peroxidases, revealing the existence of a new class of bacterial heme peroxidases.

The overall goal of the work described in this chapter is to establish and define the structural features and chemical mechanism of Orf13 by way of 1) identifying important residues in the heme active site through crystallography and site-directed mutagenesis, 2) evaluating the substrate specificity for aromatic hydroxylation by chemical substituent requirements and 3) identifying the oxygen source for catalysis.

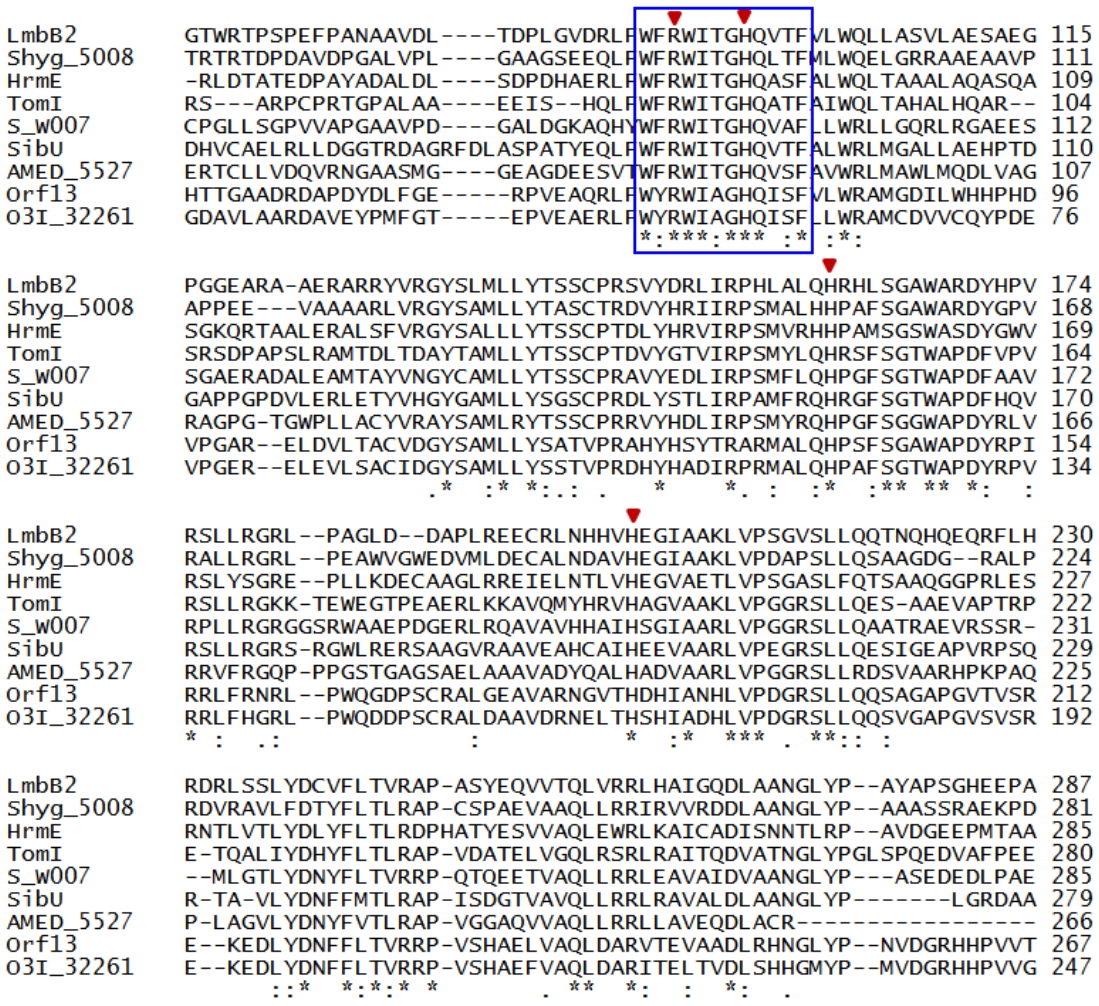

Figure 4-2. Multiple sequence alignment of the Orf13 (residues 42-267) with tyrosine hydroxylase homologues from actinomyces. The highly conserved and potential catalytic residues R71 and H76 are indicated within the proposed distal site motif $R^{71}W^{72}X_3H^{76}$ outlined by a blue box. The proposed proximal (5^{th}) ligand candidates, H140 and H184, are marked by a red diamond.

4.2 Experimental Procedures

Materials. Oligonucleotide primers for site-directed mutagenesis were purchased from Integrated DNA Technologies (San Diego, CA). Protein crystallization kits for screening included Wizard I/II and III/IV (Emerald BioSystems; Bedford, MA), Cryos Suite (Qiagen; Valencia, CA), PEG II Suite (Qiagen; Valencia, CA) and Index HR2-144

(Hampton Research; Aliso Viejo, CA). Carbon monoxide gas, CO (g), was kindly provided by the laboratory of Professor Eichhorn (University of Maryland, College Park, MD). Substrate analogues (L-phenylalanine, D-tyrosine, DL-*m*-tyrosine, tyramine, 3-(4-hydroxyphenyl) propanoic acid and *p*-cresol), catechol product analogues (dopamine, 3-(3,4-hydroxyphenyl) propanoic acid and 4-methylcatechol) and all other chemicals were purchased with the highest purity from Sigma Aldrich (St. Louis, MO). ^{18}O-labeled hydrogen peroxide ($H_2{}^{18}O_2$; 0.27% solution (w/w) with 90% ^{18}O atom incorporation) was purchased from Icon Isotope Services (Summit, NJ).

General Methods. Hydrogen peroxide stocks were prepared fresh and quantified spectrophotometrically at $\varepsilon_{240} = 43.6\ M^{-1}\ cm^{-1}$ (*71*). L-Tyrosine and L-DOPA stocks were quantified spectrophotometrically at $\varepsilon_{275} = 1.4\ mM^{-1}\ cm^{-1}$ (*69*) and $\varepsilon_{280} = 2.63\ mM^{-1}\ cm^{-1}$ (*70*), respectively. All UV-visible absorption spectra or measurement of catechol-nitrite complexes for kinetic assays were obtained with a Varian UV-vis Cary100 Spectrophotometer with Temperature Controller (Walnut Creek, CA). All fluorescence spectra or measurements were obtained with a Hitachi F-4500 fluorescence spectrophotometer (Hitachi High Technologies Corporation; Tokyo, Japan) using NSG precision cell cuvettes (Type 4; 5 mm light path, 5 x 5 mm dimension) and cell mount (A23). High performance liquid chromatography was performed with an Agilent 1000 Series HPLC (Foster City, CA) equipped with a 1100 Series multiple wavelength detector and 1200 Series fluorescence detector. Electrospray Ionization Fourier Transform Mass Spectrometry (ESI-FT-MS) was performed with an LTQ Orbitrap XL (Thermo Scientific; San José, CA) in the Proteomic Core Facility at the University of Maryland (College Park, MD). Anaerobic experiments were performed in an 830-ABC

series compact glovebox (PLAS-LABS, Inc; Lansing, MI) equipped with a Model 10 Gas Analyzer and Digital Heated Fan Box with palladium catalyst bed (Coy Laboratory Products, Inc; Grass Lake, MI).

Equilibrium binding experiments with native WT Orf13. The ligand binding assay for imidazole was performed by monitoring a change in the absorbance of the heme Soret band (3 μM Orf13 with 100% heme B occupancy in 20 mM sodium phosphate (pH 8.0) at 25 °C). Ligand binding assays for L-tyrosine, L-DOPA and L-phenylalanine were performed by monitoring a change in the heme fluorescence emission of Orf13 (2.5 μM Orf13 with 100% heme B occupancy in 20 mM sodium phosphate (pH 8.0) at 25 °C) using an excitation wavelength (λ_{EX}) at 400 nm and emission wavelength (λ_{EM}) at 625 nm (*90*). An excitation slit of 1 nm and emission slit of 20 nm were used to prevent the loss of the fluorescence emission signal of the heme from irradiation and heme bleaching. All equilibrium binding experiments were performed in triplicate for each ligand. The fractional saturation of each equilibrium binding experiment was determined by Equation 4-1, where Θ is the fractional saturation of the ligand, X_o is the measured signal (λ_{EM} at 625 nm or absorbance maximum of the Soret band, as indicated) for the unbound state of Orf13 in the absence of ligand, X_b is the measured signal for the completely bound state and X is the measured signal at a given ligand concentration. The dissociation constants (K_D) of each ligand were calculated by the best fit to the simple binding model (Equation 4-2) (*91*) using the software program Prism 4 (GraphPad); Θ is the fractional saturation of the ligand, [L] is the concentration of ligand, B_{max} is the maximal binding constant (limitation: $0 \leq B_{max} \leq 1$) and K_D is concentration of ligand required to reach half maximal binding.

Equation 4-1.

$\Theta = (X - X_o)/(X_b - X_o)$

Equation 4-2.

$\Theta = B_{max}\, x\, [L]/(K_D + [L])$

Crystallization trials with native WT Orf13. Orf13 (8.9 mg/mL with 100% heme B occupancy; 20 mM Tris-HCl (pH 8.0), 10 mM imidazole and 10% glycerol) was screened against 5 crystallization kits (Wizard I/II and III/IV (Emerald), Cryos Suite (Qiagen), PEG II Suite (Qiagen) and HR2-144 (Hampton Research)) using a Crystal Phoenix instrument (*ARI, Art Robbins Instruments*). Each screen of Orf13 was performed using 96 well crystallization trays with 3 enzyme to precipitant solution ratios (1:2, 1:1, and 2:1) per well. Trays were sealed and incubated at 20 °C for 1 week before checking crystal growth by microscope. Anaerobic screening was performed by the microbatch method in an anaerobic glove box. All solutions (oil and kits) were degassed and stored within the glove box for 1 week prior to screening. Orf13 purified anaerobically (15.2 mg/mL with 87% heme B occupancy; 20 mM sodium phosphate (pH 8.0), 80 mM sodium chloride and 10% glycerol) was manually screened (1:1; enzyme to precipitant solution) per well containing baby oil (10 µL; Johnson & Johnson®). The screening conditions included Cryos Suite (A1-F12), Index HR2-144 (A1-F12), Wizard III (A1-C12) and Wizard IV (A1-C12). Plates were placed in a small box containing a wet paper towel and incubated for 2 weeks under anaerobic conditions at 25 °C. The plates were removed from the glove box to evaluate crystallization under a microscope.

Site-directed mutagenesis of native Orf13. Mutagenesis of the native Orf13 construct (pET24a/*orf13*) for expression in BL21(DE3) *E. coli* was performed according

to the Statagene QuikChange® Site-Directed Mutagenesis Kit protocol (Agilent Technologies, Inc; Wilmington, DE). The oligonucleotides to generate variants for the proposed distal site motif ($R^{71}W^{72}X_3H^{76}$) and the potential proximal (5^{th}) ligands (H140 and H184) are listed in Table 4-1. The QuikChange® reactions were digested with DpnI for 12 hr at 37 °C and transformed (10 µL aliquot) into GeneHogs (60 µL) (Invitrogen; Carlsbad, CA). DNA was isolated by miniprep (Fermentas; Glen Burnie, MD) from selected colonies that were resistant to kanamycin and DNA sequencing confirmed correct construction of the variants (Table 4-1). Expression of each variant in BL21(DE3) *E. coli* was performed in the presence of ferric iron (III) citrate (500 µM final) under the same optimized conditions previously described for native WT Orf13 in Chapter 2.

Table 4-1. Orf13 Variants Generated by Site-Directed Mutagenesis

Orf13 Variant[a]	Proposed Role	Oligonucleotide Primers (5' – 3')[b]
H76A	Catalytic	CGAACGAGATCTGCGCGCCGGCGATCCAGC
		GCTGGATCGCCGGCGCGCAGATCTCGTTCG
H76C	Catalytic	CGAACGAGATCTGGCAGCCGGCGATCCAGC
		GCTGGATCGCCGGCTGCCAGATCTCGTTCG
R71A	Catalytic	GCCGGCGATCCACGCGTACCAGAACAGCCG
		CGGCTGTTCTGGTACGCGTGGATCGCCGGC
R71K	Catalytic	GGCCGGCGATCCATTTGTACCAGAACAGCCGC
		GCGGCTGTTCTGGTACAAATGGATCGCCGGCC
H140C	Proximal (5^{th})	GCTGAACGACGGGCACTGCAGCGCCATGC
	Ligand	GCATGGCGCTGCAGTGCCCGTCGTTCAGC
H184C	Proximal (5^{th})	GGCGATGTGGTCGCAGGTCACGCCGTTGC
	Ligand	GCAACGGCGTGACCTGCGACCACATCGCC

[a]Variants constructed with the non-fusion tagged Orf13 vector (pET24a/*orf13*).
[b]Nucleotide mutations are underlined for each variant.

Purification and reduced-CO (g) spectra of Orf13 variants H140C and H184C. Three grams of cells expressing Orf13 variant H140C or H184C were purified as described for native WT Orf13 using the Ni-Sepharose method (Refer to Chapter 2). The

Ni-Sepharose pooled enzyme variants (50 mM sodium phosphate (pH 8.0), 300 mM NaCl, 80 mM imidazole and 1 mM DTT) were concentrated to 15 mg/mL, flash frozen by liquid nitrogen in droplet form and stored at -80 °C. Purity of the Orf13 H140C and H184C variants were greater than 90% as judged by SDS-PAGE. The protein concentration was determined using the experimentally determined extinction coefficient for WT Orf13 (ε_{280} 2.8 ± 0.2 mL mg^{-1} cm^{-1} (pH 8.0, 25 °C)), the heme B quantitation and stoichiometry was measured by the pyridine hemochromagen method (*40*), and the specific activity of Orf13 H140C and H184C was measured using the L-DOPA colorimetric assay protocol. The reduced-CO (g) spectrum of the Orf13 H140C variant (4.6 μM) with 100% heme B occupancy or the Orf13 H184C variant (17.8 μM) with 36% heme B occupancy in 50 mM sodium phosphate (pH 8.0) was measured as described in Chapter 3.

Chemical synthesis, purification and quantitation of dityrosine. Dityrosine was chemically synthesized from L-tyrosine as described (*92, 93*) with a slightly modified procedure. A reaction mixture (5 mL) containing L-tyrosine (13 mM), nickel (II) acetate ($Ni(OAc)_2$; 26 mM) and potassium monopersulfate (oxone; 12 mM final containing 6 mM of potassium peroxymonosulfate, $KHSO_5$) in 10 mM sodium borate buffer (pH 10) was stirred for 30 min at room temperature in a glass vial. Sodium hydroxide (120 mM final) was added at the start of the reaction to maintain the basicity of the solution at pH 10. The reaction mixture was filtered through a MCE filter disc (0.45 μm, Millipore; Billerica, MA) to remove solid particles and clarify the reaction solution prior to HPLC analysis and purification of dityrosine. An HPLC method to separate L-tyrosine and dityrosine was performed as described (*94*) with direct detection

of dityrosine by HPLC-FLD (λ_{EX} 325 nm, λ_{EM} 410 nm). Reaction aliquots (525 µL) from the filtered mixture were treated with 99% TFA (5 µL) and analyzed by HPLC-FLD. Dityrosine had an average retention time of 9.9 min and was confirmed by ESI-FT-MS with a singly charged mass of 361.13 m/*z* (exact mass: 360.12). Aliquots of purified dityrosine were pooled (~ 4 mL) and lyophilized. The yellowish-orange resin was solubilized in deionized water (150 µL) and the final dityrosine concentration was quantified spectrophotometrically at ε_{315} = 5.2 mM^{-1} cm^{-1} in 25 mM sodium phosphate (pH 8.0) (*95*).

Dityrosine production assay with native WT Orf13. Two reaction conditions were tested to assess the enzymatic production of dityrosine: 1) Orf13 pre-incubation in the presence of H_2O_2 followed by addition of L-tyrosine, and 2) Orf13 pre-incubation with L-tyrosine followed by reaction initiation with H_2O_2. The final assay conditions included Orf13 (3 µM; 100% heme B occupancy), L-tyrosine (5 mM final) and H_2O_2 (500 µM final) in 100 mM sodium phosphate (pH 8.0). Orf13 was pre-incubated with L-tyrosine or H_2O_2 for 5 min at 37 °C followed by addition of the other substrate not included during pre-incubation. All assays were performed at 37 °C up to 30 minutes with aliquots (525 µL) quenched with 99% TFA (5 µL) at time zero and 30 min. Each sample (500 µL) was analyzed by HPLC-FLD as described for detection of dityrosine (*94*). The amount of dityrosine produced by Orf13 was determined based on a calibration curve (2 to 20 µM) of chemically synthesized and purified dityrosine. The dityrosine standard samples were quantified spectrophotometrically and treated under the same assay conditions and sample work up described. The average retention times of the chemical standards: L-DOPA (7.3 min), L-tyrosine (8.5 min) and dityrosine (9.9 min).

Assay controls included the same concentrations as the assay samples; 1) Orf13 only, 2) Orf13 and L-tyrosine, 3) L-tyrosine with H_2O_2.

Aromatic hydroxylation by native WT Orf13 with substrate analogues. Production of L-tyrosine was monitored by HPLC-FLD as described (*68*) for assays with L-phenylalanine as the substrate. Orf13 (1.5 μM) was incubated with L-phenylalanine (5 mM final) for 5 min at 37 °C in 100 mM sodium phosphate (pH 8.0) followed by addition of H_2O_2 (500 μM final) to initiate the reaction. Assays were performed in triplicate at 37 °C for 4 min with time points taken at 1, 2, 3, and 4 min. Each aliquot was treated as described for the HPLC-FLD method to detect the formation of L-tyrosine (Refer to Chapter 3). Assay controls included the same concentrations as the activity assay sample in 100 mM sodium phosphate (pH 8.0); 1) Orf13 only, 2) Orf13 and L-phenylalanine, 3) L-phenylalanine, 4) L-phenylalanine with H_2O_2, 5) L-tyrosine, and 6) L-tyrosine (100 μM) with H_2O_2. All controls were run in triplicate the same day as the assay samples containing Orf13, L-phenylalanine and H_2O_2, and underwent the same method workup described.

Assays using the substrate analogues DL-*m*-tyrosine, tyramine, 3-(4-hydroxylphenyl) propanoic acid and *p*-cresol were monitored by the L-DOPA colorimetric assay for their respective catechol products; L-DOPA, dopamine, 3-(3,4-hydroxyphenyl) propanoic acid and 4-methylcatechol. Orf13 (1.5 μM) was incubated with L-tyrosine (5 mM final) or substrate analogue (5 mM final) for 5 min at 37 °C in 100 mM sodium phosphate (pH 8.0), followed by addition of H_2O_2 (500 μM final) to initiate the reaction. An aliquot from each substrate analogue reaction was quenched at 2 minutes, treated under the same colorimetric workup described in Chapter 3 and scanned

to obtain a UV-visible absorption spectrum to confirm formation of a catechol-nitrite complex. In assays to assess the relative specific activity for substrate selectivity, Orf13 (1.5 μM) was incubated with L-tyrosine (5 mM final) or substrate analogue (5 mM final) for 5 min at room temperature in 100 mM sodium phosphate (pH 8.0), followed by addition of H_2O_2 (250 μM final) to initiate the reaction. Assays were performed in triplicate with each substrate at room temperature for 11 min with time aliquots taken at 1, 3, 6, and 11 min.

Assays to assess substrate stereoselectivity were performed under normal Orf13 specific activity conditions: Orf13 (0.75 μM) was incubated with L-tyrosine (5 mM final) or D-tyrosine (5 mM final; 99% optical purity) for 5 min at 37 °C in 100 mM sodium phosphate (pH 8.0), followed by addition of H_2O_2 (500 μM final) to initiate the reaction. Assays were performed in triplicate at 37 °C for 4 min with time points taken at 1, 2, 3, and 4 min. Standard curves of the respective catechol products from 1 to 100 μM were prepared the same day for each set of assays. These substrate analogues and catechol products were quantified spectrophotometrically at ε_{275} = 1.4 mM^{-1} cm^{-1} (*69*) and ε_{280} = 2.63 mM^{-1} cm^{-1} (*70*), respectively. Assay controls with a blank solution without Orf13 were used to correct for background. Orf13 background control assays were carried out with the same concentration of enzyme in the absence of substrates. No enzyme background at 500 nm was observed with 1.5 μM Orf13 or less. All controls were run in triplicate and in parallel with assay samples and underwent the same colorimetric workup described in Chapter 3.

Identification of the oxygen source for tyrosine hydroxylation. Native WT Orf13 (3 μM; 48% heme B occupancy) was pre-incubated in 100 mM sodium phosphate

(pH 8.0) with L-tyrosine (5 mM) for 5 min at 37 °C. Hydrogen peroxide (H_2O_2) or ^{18}O-labeled hydrogen peroxide ($H_2{}^{18}O_2$; 90% ^{18}O atom incorporation) (500 μM final) was added to initiate the reaction. All assays were performed at 37 °C for 8 min, at which time the entire assay sample (520 μL) was injected into the HPLC instrument and analyzed as described for the detection of L-tyrosine and L-DOPA by HPLC-FLD (*68*). L-DOPA and L-tyrosine standards had an average retention time of 4.5 and 5.5 minutes, respectively. The L-DOPA product from each assay was collected (T_R 4.5 min), treated with formic acid (1%, v/v) and injected into an ESI-FT-MS to analyze the singly charged mass ion of the DOPA product. L-DOPA standard was treated and analyzed accordingly, and had an observed singly charged mass of 198.07 m/*z* (exact mass: 197.07).

4.3 Results and Discussion

Equilibrium binding experiments. The dissociation constants (K_D) of L-tyrosine, L-DOPA and L-phenylalanine were determined by equilibrium binding titration using the fluorescence properties of heme B bound to Orf13. Typically, the intrinsic tryptophan fluorescence of an enzyme (λ_{EX} 270 – 290 nm; λ_{EM} 340 nm) allows for the measurement of ligand dissociation constants. However, this approach could not be used since the ligands have similar aromatic structure and fluorescence properties that masked the enzyme fluorescence emission signal. Fluorescence properties of heme have been used to measure ligand binding by excitation of the Soret band wavelength at 400 nm with emission detected at 625 nm (*90*). Application of this experimental approach to Orf13 showed similar excitation and emission spectra of the bound heme B to the reported spectra for horseradish peroxidase (*90*) (See Appendix A-11). Addition of phenolic ligands, such as L-tyrosine, to ferric Orf13 quenches the fluorescence emission

maxima at 625 nm and 680 nm, but with greater signal change at 625 nm (Figure 4-3A). The fluorescence emission maximum at 625 nm was selected to monitor the change in emission intensity relative to the amount of titrated ligand (Figure 4-3B) to determine the dissociation constant.

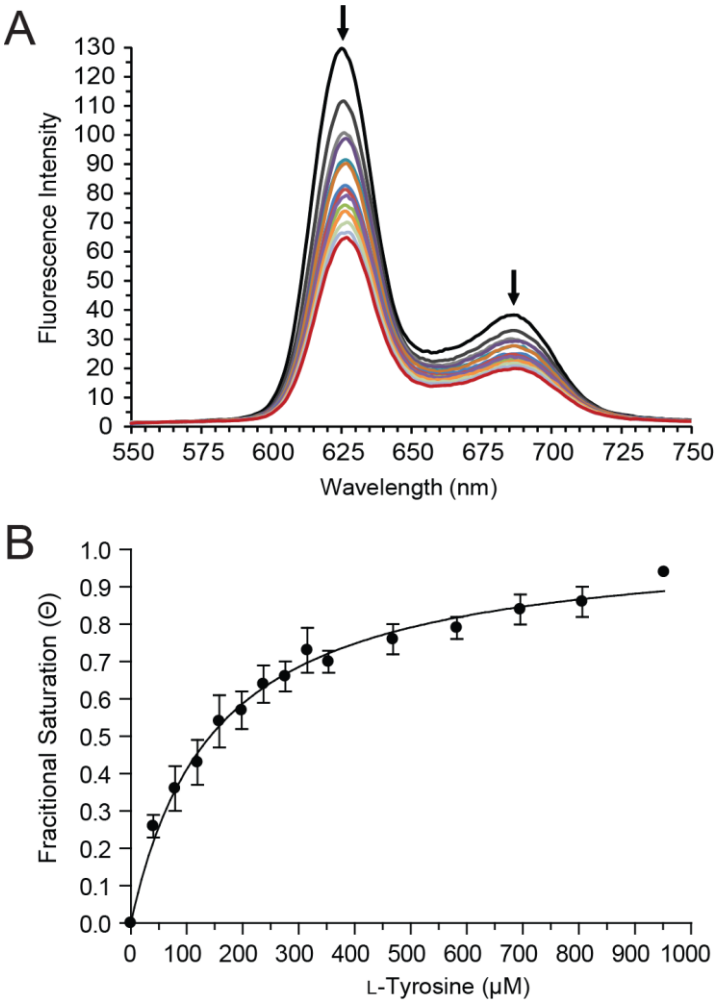

Figure 4-3. Equilibrium ligand binding experiment for L-tyrosine with Orf13 (100% heme B) in 20 mM sodium phosphate (pH 8.0) at 25 °C; (A) The fluorescence emission spectra of heme B bound to Orf13 upon titration of L-tyrosine. (B) Direct plot of the average fractional saturation for L-tyrosine with Orf13 from the change of λ_{EM} at 625 nm.

The dissociation constants for L-tyrosine, L-DOPA, L-phenylalanine and imidazole were calculated using the equilibrium titration analysis for simple one site binding (Table 4-2; See Appendices A-12 to A-15) (*91*). The dissociation constant of L-tyrosine (150 ± 11 μM) is 3 fold lower than the apparent K_m (450 ± 40 μM). The binding behavior of L-DOPA was poor as it did not display a rectangular hyperbolic curve expected for the simple binding model with a calculated dissociation constant of 750 ± 110 μM (See Appendix A-13). This is 5-fold greater than L-tyrosine and is expected since it is the product of the reaction and the heme-iron of Orf13 is in the ferric resting state. The dissociation constant of L-phenylalanine (500 ± 160 μM) is 3-fold greater than L-tyrosine. However, this ligand also did not bind well and displayed a fractional saturation curve that deviates from the simple one site binding model (See Appendix A-14).

Table 4-2. Ligand Dissociation Constants for Native WT Orf13

Ligand	K_D (μM)[a]
L-Tyrosine	150 ± 11
L-DOPA	750 ± 110
L-Phenylalanine	500 ± 160
Imidazole[b]	1500 ± 100

[a]Dissociation constants were calculated by the best fit line to the simple one site binding model (Equation 4-2) (*91*).
[b]Equilibrium binding assessed by change in Soret band absorbance of heme B.

Imidazole does not quench the heme fluorescence signal but induces a change in the absorbance of Soret band. The effect of imidazole on the absorption properties of the heme was used to measure its dissociation constant. The resulting binding of this ligand causes a decrease in the Soret band absorbance and a positional change from 403 nm to

406 nm, and changes the relative absorbance intensity of the Q-bands at 543 nm and 567 nm (Figure 4-4A). This indicates that imidazole is binding in or near the heme active site. Imidazole (10 mM) protecting Orf13 during aerobic purification is at a saturating concentration approximately 7-fold greater than the imidazole dissociation constant (1.5 ± 0.1 mM) (Figure 4-4B; See Appendix A-15). Orf13 purified in the presence of imidazole is dark red while in its absence (protected anaerobically) is dark brown. The qualitative color changes of Orf13 in the presence or absence of imidazole are directly related to characteristic changes in the heme spectra (Figure 4-4A). These results explain the observed chemical protection of Orf13 against auto-oxidative degradation during aerobic purification when in the presence of imidazole. The inhibition constant (K_I) of imidazole for tyrosine hydroxylation by Orf13 was not determined. However, the amount of imidazole present in the specific activity assays and steady-state kinetic measurements was 40 to 150-fold less (10 to 40 μM final) than the dissociation constant. Therefore, inhibition of turnover due to the presence of imidazole is not likely. Overall, the dissociation constants for L-tyrosine, L-DOPA, L-phenylalanine and imidazole provide useful information for crystallography work involving co-crystallization or crystal soaking experiments to obtain a structure of Orf13 with a ligand bound.

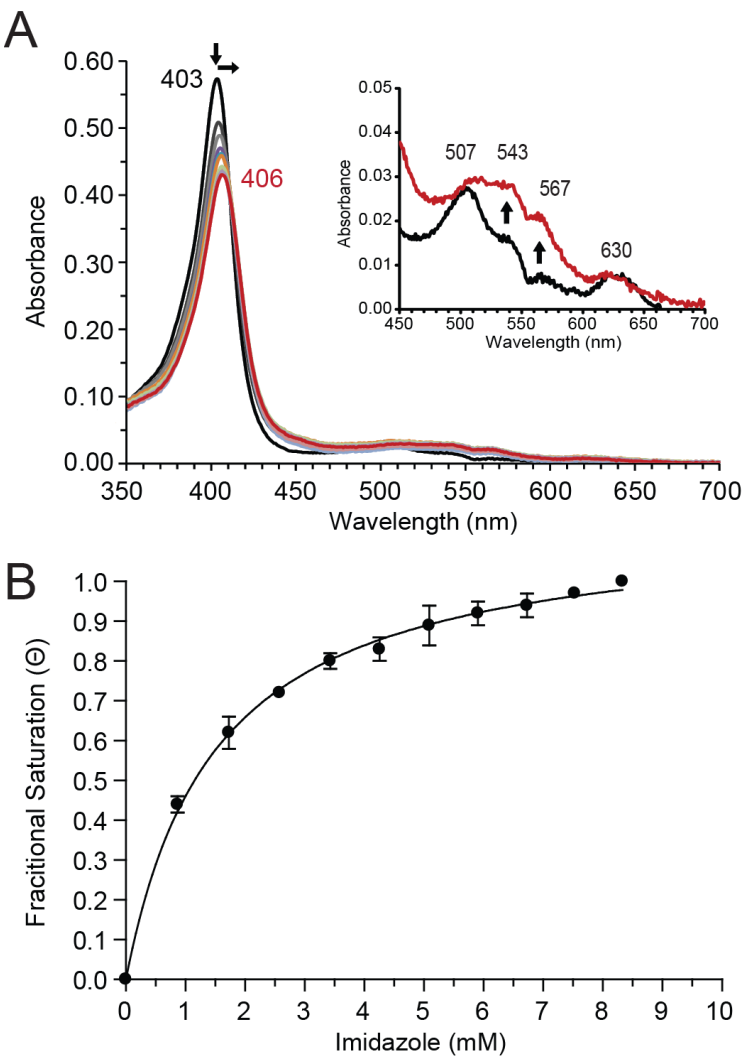

Figure 4-4. Equilibrium ligand binding experiment for imidazole with Orf13 (100% heme B) in 20 mM sodium phosphate (pH 8.0) at 25 °C; (A) Visible absorption spectra of heme B bound to Orf13 upon titration of imidazole. Inset: visible absorption spectra of the Q-bands in the absence (black trace) or presence of imidazole (red trace; 8.3 mM final); (B) Direct plot of the average fractional saturation for imidazole with Orf13 from the absorbance maximum of the Soret band (403 nm to 406 nm).

Crystallization of native WT Orf13. Crystallization of Orf13 is critical for the identification of active site residues and the proximal (5^{th}) heme-iron ligand, as well as to determine the overall structural fold of the enzyme. No crystallization conditions were found after aerobic screening of the enzyme with 100% heme B. Only a heavy reddish-brown precipitant was observed. This indicates that a lack of enzyme stability

exacerbated by auto-oxidative degradation is likely preventing crystallization. The oxidative degradation of Orf13 has already been well observed and documented since the start of its characterization (Refer to Chapter 2). Severe protein degradation is most likely related to the reactivity of the heme-iron; however, this auto-oxidative process is not completely understood as there is no structural information for this enzyme. Orf13 was initially protected by imidazole (10 mM) in the storage condition; however, the final concentrations of imidazole during screening fell below saturating levels after mixing with the crystallization precipitant (3.3, 5 or 6.6 mM final imidazole at 2, 3 and 4-fold, respectively, of its K_D). Non-saturating concentrations of imidazole would have likely made Orf13 susceptible to auto-oxidative damage, in addition to adding heterogeneity to the sample which can prevent crystallization. Specifically, the heterogeneity is within the heme active site since imidazole can bind to the heme-iron (Figure 4-4A). This causes a slight red shift of the Soret band (from 403 nm to 406 nm) which indicates a change in coordination state of the heme-iron. Since stable and active Orf13 can be maintained in the absence of oxygen without chemical protectants, anaerobic screening was pursued to limit any additional heterogeneity in the sample. However, these efforts also did not result in finding a crystallization condition for Orf13. A more rigorous effort will need to be pursued to crystallize this difficult enzyme. The key conditions which may prove useful in future crystallography work include 1) repeating the aerobic screening with saturating amounts of imidazole (30-40 mM) and 2) to anaerobically re-screen and co-crystallize Orf13 with L-tyrosine (2 mM), particularly if initial crystallization conditions are observed from aerobic screening.

Mutagenesis of the proposed catalytic residues R71 and H76. The chemical mechanism for the heterolytic cleavage of hydrogen peroxide by heme peroxidases involves acid/base chemistry between a highly conserved arginine and histidine residue located in the active site on the distal side of the heme (*31*). In Orf13, R71 and H76 are two highly conserved residues in a proposed distal site motif ($R^{71}W^{72}X_3H^{76}$) that is similar to the distal site motif found in heme peroxidases ($RX_2F(W)H$). If R71 and H76 in Orf13 are involved in the heterolytic cleavage of hydrogen peroxide, then catalysis should be disrupted with variants of these residues. The proposed catalytic role of R71 and H76 could not be established since neither set of variants were soluble after expression. The harvested cells for Orf13 variants H76A, H76C, R71A and R71K expressed in BL21(DE3) *E. coli* with iron (III) citrate were yellow, which indicated the absence of bound heme B. Expression of each variant was observed by SDS-PAGE; however, all were insoluble after cell lysis by French press. This prevented further characterization to assess their proposed catalytic role for the heterolytic cleavage of hydrogen peroxide. The lack of red color and protein solubility indicate these variants are unable to bind heme B, which was likely due to protein mis-folding from a site-directed mutation in a highly conserved region (Figure 4-2).

Evaluation of the proposed proximal (5^{th}) ligand residues H140 and H184. The enzyme residue in Orf13 that coordinates the heme-iron may likely be a histidine residue based on 1) the high spin state of the heme-iron in ferric Orf13 observed by low temperature EPR, 2) the Soret maximum shift to 421 nm in a reduced-CO (g) UV-visible absorption spectrum of Orf13 and 3) the identification of two other highly conserved histidine residues (H140 and H184) with similar sequence spacing from the catalytic

distal site histidine found in heme peroxidases (*43*). If one of these histidine residues is the proximal (5^{th}) ligand, then this residue can be identified in a reduced-CO (g) UV-visible absorption spectrum with a cysteine variant. The cysteine variant which coordinates the heme-iron will display a Soret maximum shift at or near 450 nm similar to thiolate-ligated cytochrome P450s (*59*).

The color of harvested cells for both variants, H140C and H184C, expressed in BL21(DE3) *E. coli* with iron (III) citrate were red, similar to WT Orf13. Both were soluble upon lysis by French press and were able to intrinsically bind to the Ni-Sepharose resin as observed with WT Orf13. Only the Ni-Sepharose purification step was performed and resulted in greater than 90% purity as judged by SDS-PAGE. This purity was sufficient to evaluate the reduced-CO (g) spectra of the H140C and H184C variants (Note: Orf13 variant H76C was not soluble and could not be evaluated as a possible proximal (5^{th}) ligand residue). The UV-visible absorption spectrum of the purified H140C variant resembled the spectrum of purified WT Orf13 (RZ value 1.8) with an RZ value ~ 1.6 and confirmed heme B occupancy of 100% (Figure 4-5A). This variant displayed catalytic activity for L-DOPA formation with a similar turnover rate (22 ± 2 min^{-1}) as 100% heme B occupied WT Orf13 (28 ± 2 min^{-1}). The reduced-CO (g) UV-visible absorption spectrum of H140C is similar to WT Orf13 with a Soret maximum at 418 nm (Figure 4-5B), indicating that the native histidine residue is not likely the proximal (5^{th}) ligand.

The UV-visible absorption spectrum of the H184C variant appeared to have a broader Soret band and only two distinguishable Q-bands (Figure 4-6A). The RZ value was 3 fold lower at ~0.6, indicating a low percentage of heme B occupancy that was

confirmed as 36% by the pyridine hemochromagen assay. The PPIX stoichiometry was not determined but it was anticipated to be roughly 64% to make up the occupancy difference. This variant displayed low catalytic activity for L-DOPA formation with a turnover rate of 3 ± 1 min^{-1}, which likely reflects the low occupancy of heme B. The reduced-CO (g) UV-visible absorption spectrum of the H184C variant is also similar to WT Orf13 with Soret maxima at 417 nm (Figure 4-6B).

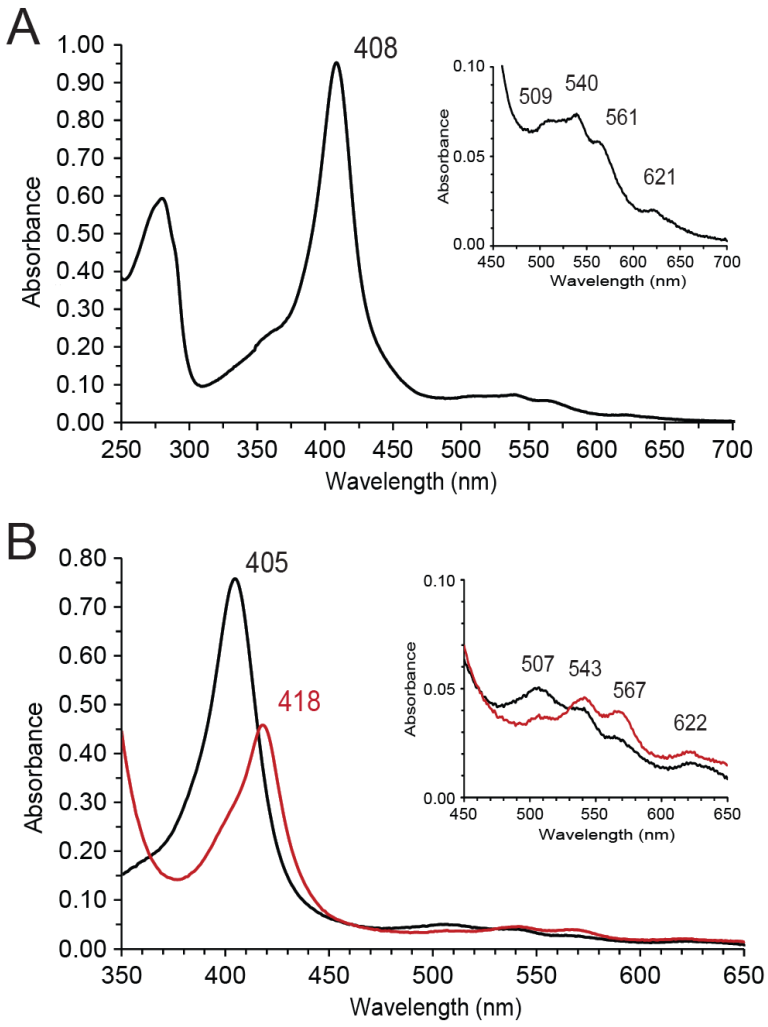

Figure 4-5. UV-visible spectra of Orf13 H140C variant; (A) UV-visible absorption spectrum of purified H140C variant (100% heme B occupancy) in 50 mM sodium phosphate (pH 8.0), 30 mM sodium chloride and 10 mM imidazole; (B) UV-visible absorption spectrum of ferric heme Orf13 H140C (black trace) and ferrous-CO (g) heme (red trace) in 50 mM sodium phosphate (pH 8.0) and 3 mM sodium chloride.

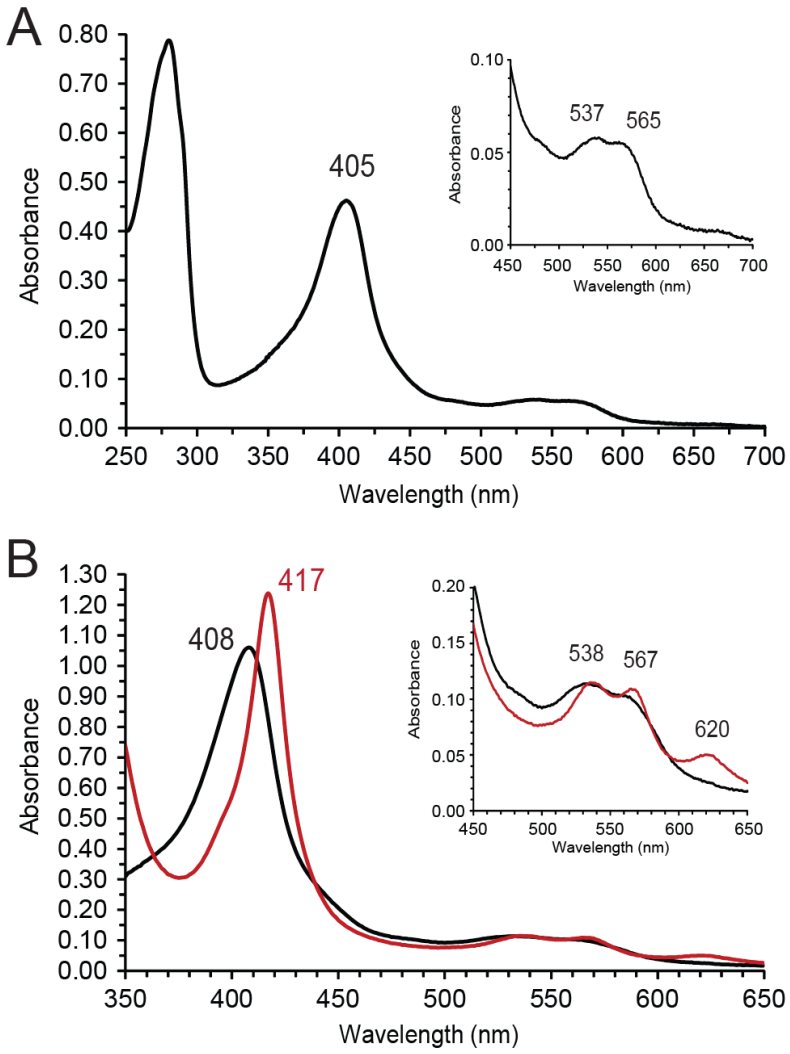

Figure 4-6. UV-visible spectra of Orf13 H184C variant; (A) UV-visible absorption spectrum of purified H184C variant (36% heme B occupancy) in 50 mM sodium phosphate (pH 8.0), 30 mM sodium chloride and 10 mM imidazole; (B) UV-visible absorption spectrum of ferric heme Orf13 H184C (black trace) and ferrous-CO (g) heme (red trace) in 50 mM sodium phosphate (pH 8.0) and 12 mM sodium chloride.

The reduced-CO (g) spectra of Orf13 variants H140C and H184C do not appear to support Orf13 as a histidyl-ligated heme peroxidase as neither variant displays a Soret band shift to 450 nm that is expected for a thiolate-ligated heme-iron. However, the heme environment and axial coordination with the heme-iron can limit direct assessment and assignment of the proximal (5^{th}) residue using this reduced-CO (g) spectroscopic assay.

The ferrous-CO (g) Soret band at or near 450 nm (P450 species) in cytochrome P450 enzymes can transition to an inactive P420 species (at or near 420 nm) due to the proposed formation of a protonated thiol which coordinates the heme-iron (*96-99*). Formation of the P420 species can be pH dependent (*98*), pressure dependent (*99*) and/or affected by salts such as NaCl (*96, 100*). The ferrous-CO (g) spectral characteristics of the Orf13 H184C variant are very similar to the ferrous-CO (g) spectrum of the P420 species in P450cam (*96*), particularly with respect to the height and position of the Soret band and the observed Q-bands at 538 nm and 567 nm (Figure 4-6B). Typically, reduction of ferric heme to the ferrous state decreases the height of the Soret band since the spin state of the iron changes from high to low. This common spectral trend was observed in the ferrous-CO (g) spectra of WT Orf13 (Refer to Chapter 3, Figure 3-6) and the Orf13 H140C variant (Figure 4-5B). However, the Soret band height of ferrous-CO heme in the H184C variant increased (Figure 4-6B) in a similar manner to the formation of P420 species observed with P450cam (*96*). This suggests that the observed species in the H184C variant is a P420-like species that originated from a P450 heme species. Therefore, H184 is likely the proximal (5^{th}) ligand residue. However, direct evidence to identify the proximal (5^{th}) ligand and to confirm H184 as this ligand from the spectroscopic data described will depend on obtaining a crystal structure of native WT Orf13.

Assessment of dityrosine production by Orf13. Classical heme peroxidases (horseradish peroxidase (HRP) and myeloperoxidase (MPO)) catalyze 2-sequential 1-electron transfer reactions with aromatic substrates that non-enzymatically generate radically coupled products, such as dityrosine (*31, 95, 101*) (Figure 4-7). Orf13 is

classified as a unique heme peroxidase with a primary catalytic pathway for hydrogen peroxide dependent aromatic hydroxylation of L-tyrosine. This enzyme also exhibits peroxygenase activity that is similar to HRP by way of a secondary catalytic pathway for molecular oxygen dependent tyrosine hydroxylation in the presence of dihydroxyfumaric acid or L-ascorbate (Refer to Chapter 3). However, it is not known if Orf13 is able to catalyze a 2-sequential 1-electron transfer reaction which can be indirectly observed by the non-enzymatic production of dityrosine.

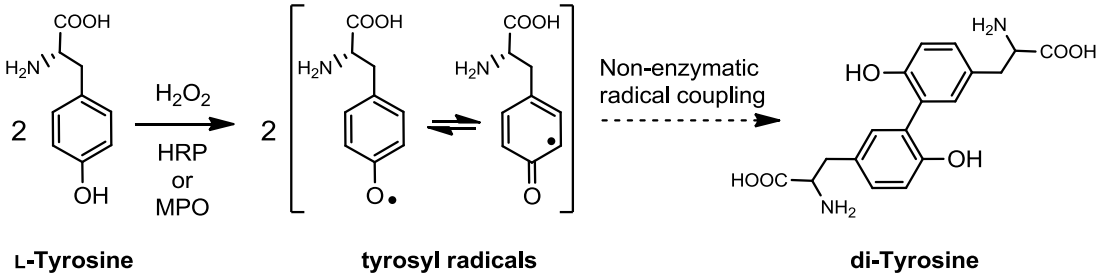

Figure 4-7. The 2-sequential 1-electron transfer reaction of horseradish peroxidase and myeloperoxidase that promotes non-enzymatic dityrosine formation.

To assess the production of dityrosine by Orf13 in the presence of L-tyrosine and hydrogen peroxide, a HPLC separation method was performed as described (*94*) with fluorescence detection added to specifically monitor dityrosine. The fluorescent properties of dityrosine (λ_{EX} 325 nm, λ_{EM} 410 nm) are different from L-tyrosine and L-DOPA (λ_{EX} 281 nm, λ_{EM} 314 nm) and allow for greater sensitivity in its detection from enzymatic assays where yields may be low (*94*). L-Tyrosine and L-DOPA standards are only detected by absorbance at 280 nm and not λ_{EM} 410 nm (See Appendix A-16). The retention time of chemically synthesized dityrosine was confirmed at 10 min by ESI-FT-MS (Figure 4-8).

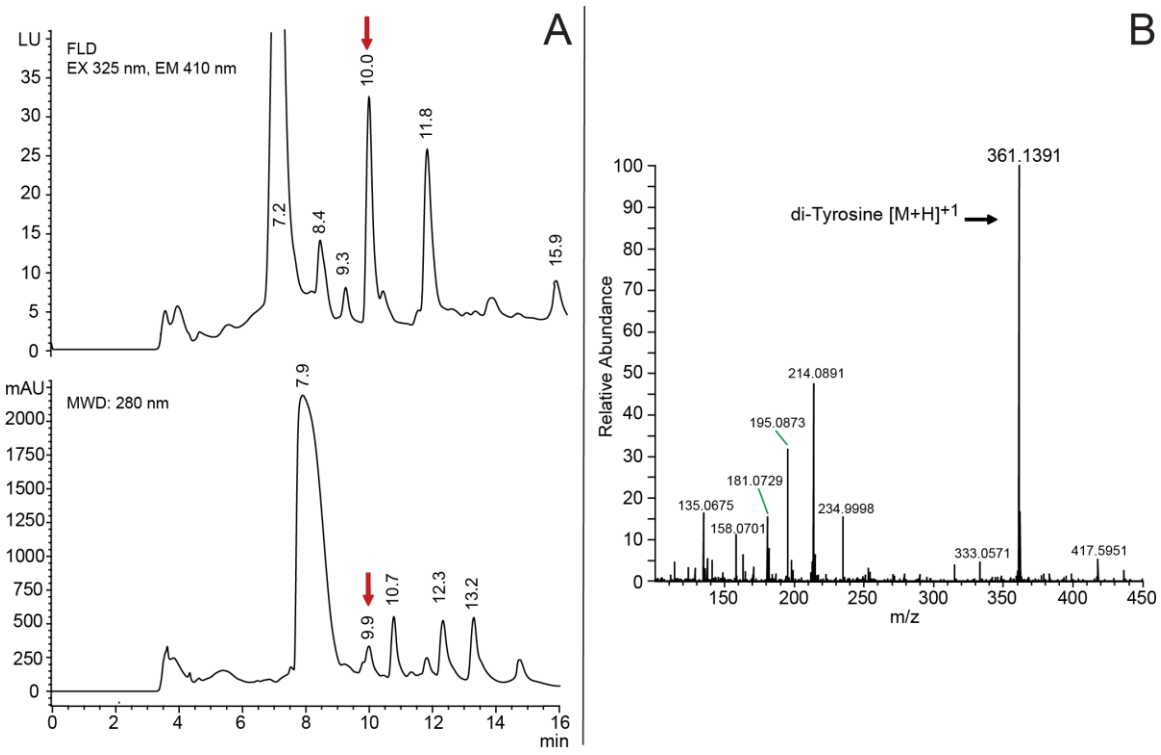

Figure 4-8. (Panel A) HPLC chromatograms of the dityrosine reaction mixture monitored at λ_{EM} 410 nm and absorbance at 280 nm; L-Tyrosine (T_R 7.9 min). (Panel B) ESI-FT-MS of the compound with a retention time of 10 min (indicated by red arrow in Panel A) was confirmed as dityrosine by an observed singly charged peak of 361.13 m/*z*.

Detection of dityrosine from Orf13 reactions was not observed with reaction conditions similar to the 4 minute specific activity assay for production of L-DOPA. However, if the reaction was allowed to proceed up to 30 minutes, dityrosine was detected (Figure 4-9A). As expected the L-DOPA production was observed at 280 nm (TR 7.1 min) for Orf13 pre-incubated with L-tyrosine followed by addition of hydrogen peroxide. A co-injection of dityrosine standard confirmed dityrosine formation (Figure 4-9B) and the average amount of dityrosine produced at 30 minutes was 6.5 ± 0.3 µM. A second compound detected by fluorescence that eluted at 11.6 minutes had been observed in the time zero control for the 30 minute reaction (Figure 4-9A). This indicated it was a background species and ESI-FT-MS analysis of this compound was not pursued for its

identification. In a control reaction containing L-tyrosine and hydrogen peroxide, dityrosine was not formed, demonstrating that the dityrosine observed from the Orf13 reaction is promoted by the enzyme which had generated tyrosyl radical products that coupled together. Furthermore, an enzyme control reaction with Orf13 pre-incubated with hydrogen peroxide did not show dityrosine formation by FLD or L-DOPA production at 280 nm (See Appendix A-17). This confirms inactivation of the enzyme in the absence of L-tyrosine, in addition to demonstrating that the main function of Orf13 is tyrosine hydroxylation.

Overall, these data emphasize that the primary function of Orf13 is tyrosine hydroxylation. Although the formation of dityrosine is observed with Orf13, its production is insignificant over a 30 minute period. This demonstrates that 1-electron oxidation of tyrosine by Orf13 is possible, but it is not likely promoted by the same enzyme form that catalyzes the production of L-DOPA. Tyrosine hydroxylation by Orf13 plateaus beyond 4 minutes under the same assay conditions used to assess dityrosine production. Inactivation of Orf13 by H_2O_2 may have generated a non-productive species for the tyrosine hydroxylation pathway that is still capable of 1-electron transfer to the substrate, L-tyrosine. Some heme peroxidases, such as cytochrome c peroxidase and dehaloperoxidase, form an enzyme radical intermediate called Compound ES (*67, 76, 102, 103*). This is a protein radical species that is formed when the porphyrin radical of Compound I is transferred to an aromatic protein residue in the active site located at the edge of the heme. A Compound ES-like species may have been formed in Orf13 during catalysis which led to a dead-end form of the enzyme for tyrosine hydroxylation but remained competent for the transfer of 1-electron to the L-tyrosine substrate.

Accumulation of tyrosyl radical side products likely led to the non-enzymatic formation of dityrosine, which could only be detected after prolonged assay times (Figure 4-9A).

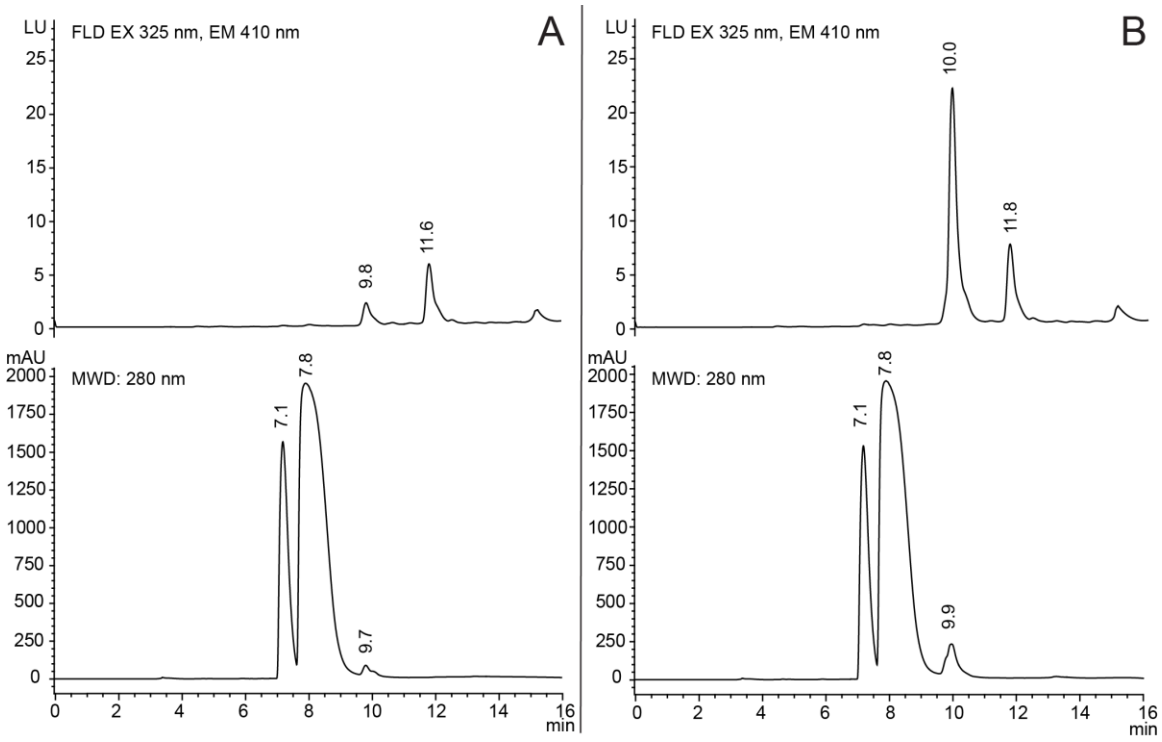

Figure 4-9. HPLC chromatograms for assessment of dityrosine production by Orf13; (Panel A) 30 minute time point of Orf13 (3 μM; 100% heme B) pre-incubated with L-tyrosine (5 mM final; T_R 7.9 min) followed by addition of H_2O_2 (500 μM final) in 100 mM sodium phosphate at 37 °C; (Panel B) 30 min time point of Orf13 assay co-injected with dityrosine standard (50 μM). Average retention times: L-DOPA (7.1 min), L-tyrosine (7.8 min) and dityrosine (9.9 min).

Substrate specificity of Orf13 for aromatic hydroxylation. Heme peroxidases are promiscuous enzymes capable of oxidizing a wide assortment of aromatic substrates. Their lack of substrate specificity has been attributed to a larger active site that can accommodate various substrates, as well as the presence of additional substrate binding locations in the vicinity of the exposed heme edges where the reaction can also occur

(*104*). The substrate analogues L-phenylalanine, D-tyrosine, DL-*m*-tyrosine, tyramine, 3-(4-hydroxyphenyl) propanoic acid and *p*-cresol were selected to test the substrate specificity of Orf13 (See Appendix A-18), as well as to evaluate the requirement of chemical substituents on the aromatic ring in order for the hydroxylation reaction to occur. The *para*-substituted phenols (tyramine, 3-(4-hydroxyphenyl) propanoic acid and *p*-cresol) were converted by Orf13 in the presence of hydrogen peroxide to their respective catechol products, which were detected as colorimetric catechol-nitrite complexes using the L-DOPA colorimetric assay (See Appendix A-19). Comparison of the relative specific activity of these substrate analogues to L-tyrosine was unsuccessful as formation of the product analogues plateaued after the first minute of turnover, while L-DOPA formation from L-tyrosine remained linear up to 6 minutes (Figure 4-10). Orf13 is more susceptible to inactivation by hydrogen peroxide in the presence of these substrate analogues than with L-tyrosine. No increase in catechol product formation was detected when L-tyrosine was added to the *p*-cresol reaction after 1 minute, confirming the inactivation of Orf13 (data not shown). No L-phenylalanine conversion to L-tyrosine was observed using an HPLC-FLD method to detect L-tyrosine, and no L-DOPA formation was observed using the L-DOPA colorimetric assay when DL-*m*-tyrosine was provided as a substrate. These results show that the hydroxyl group at the *para* position of the aromatic ring is necessary for hydroxylation since conversion of L-tyrosine, tyramine, 3-(4-hydroxyphenyl) propanoic acid and *p*-cresol to their respective catechol products is observed.

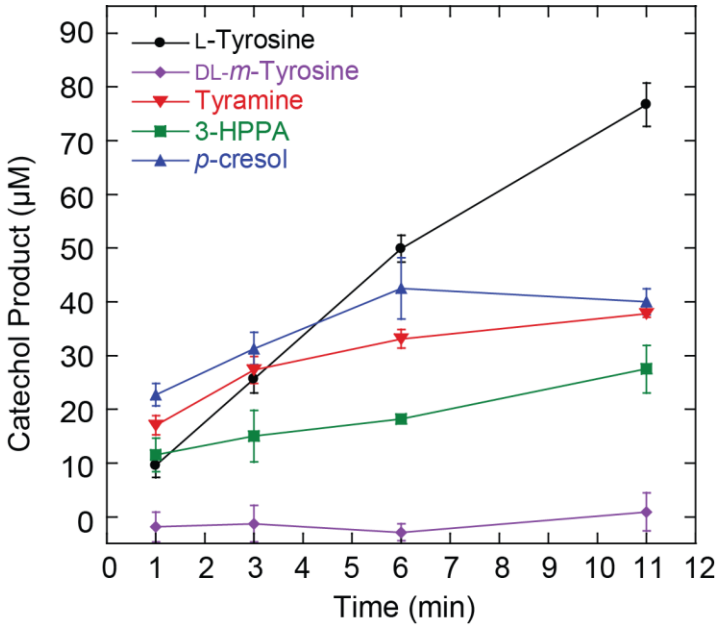

Figure 4-10. Progress curves of the aromatic hydroxylation of L-tyrosine and aromatic substrate analogues (DL-*m*-tyrosine, tyramine, 3-(4-hydroxyphenyl) propanoic acid and *p*-cresol) by Orf13. Assay conditions: Orf13 (1.5 μM; 48% heme B occupancy), 5 mM L-tyrosine or substrate analogue, 250 μM H_2O_2 in 100 mM sodium phosphate (pH 8.0) at room temperature. Figure was modified from Connor, KL et al (*43*).

The substrate stereoselectivity of Orf13 for the amino and carboxyl functional groups of tyrosine was evaluated with D-tyrosine (99% optical purity). Orf13 is stereoselective for L-tyrosine as turnover with D-tyrosine (0.7 ± 0.1 min^{-1}) was negligible compared to L-tyrosine (17.0 ± 0.4 min^{-1}) for DOPA formation measured by the DOPA colorimetric assay (See Appendix A-20). A small amount of DOPA (~ 8 μM) is produced in the D-tyrosine reaction after the first minute of turnover, but did not continue to increase for the remainder of the time course. This may indicate hydrogen peroxide inactivation of Orf13 as previously observed with the other substrate analogs. Alternatively, the small turnover observed may have been due to the presence of L-tyrosine at 1% (50 μM) of the final D-tyrosine concentration in the assay. In either case, the results show that Orf13 is selective for L-tyrosine. The stereochemistry of the amino

and carboxyl functional groups is important for proper substrate binding and orientation of L-tyrosine in the heme active site for catalysis. In addition, the poor binding of L-phenylalanine (K_D = 500 ± 160 μM) and lack of turnover for L-tyrosine production implicate the requirement of the hydroxyl group in L-tyrosine for both proper binding in the active site and catalysis.

Identification of the oxygen source for tyrosine hydroxylation. HRP and other heme peroxidases such as myeloperoxidase and chloroperoxidase are known to catalyze dimerization of aromatic substrates in the presence of hydrogen peroxide by the 2-sequential 1-electron transfer mechanism (*95, 105, 106*). However, hydroxylation of aromatic amino acids in the presence of hydrogen peroxide by heme peroxidases has not been reported (*36*). These results emphasize the uniqueness of Orf13 for its ability to use hydrogen peroxide for aromatic hydroxylation of L-tyrosine. In order to identify the source of oxygen found in the enzyme reaction product, L-DOPA, a labeling study using $H_2{}^{18}O_2$ was performed. The L-DOPA product was analyzed by ESI-FT-MS from an end point assay with Orf13 and L-tyrosine in the presence of H_2O_2 (Figure 4-11A) or $H_2{}^{18}O_2$ (Figure 4-11B). The oxygen originates from H_2O_2 as there is a 2 amu increase in the singly charged mass of the L-DOPA product (200.07 m/*z*) to indicate the incorporation of an ^{18}O atom (Figure 4-11B).

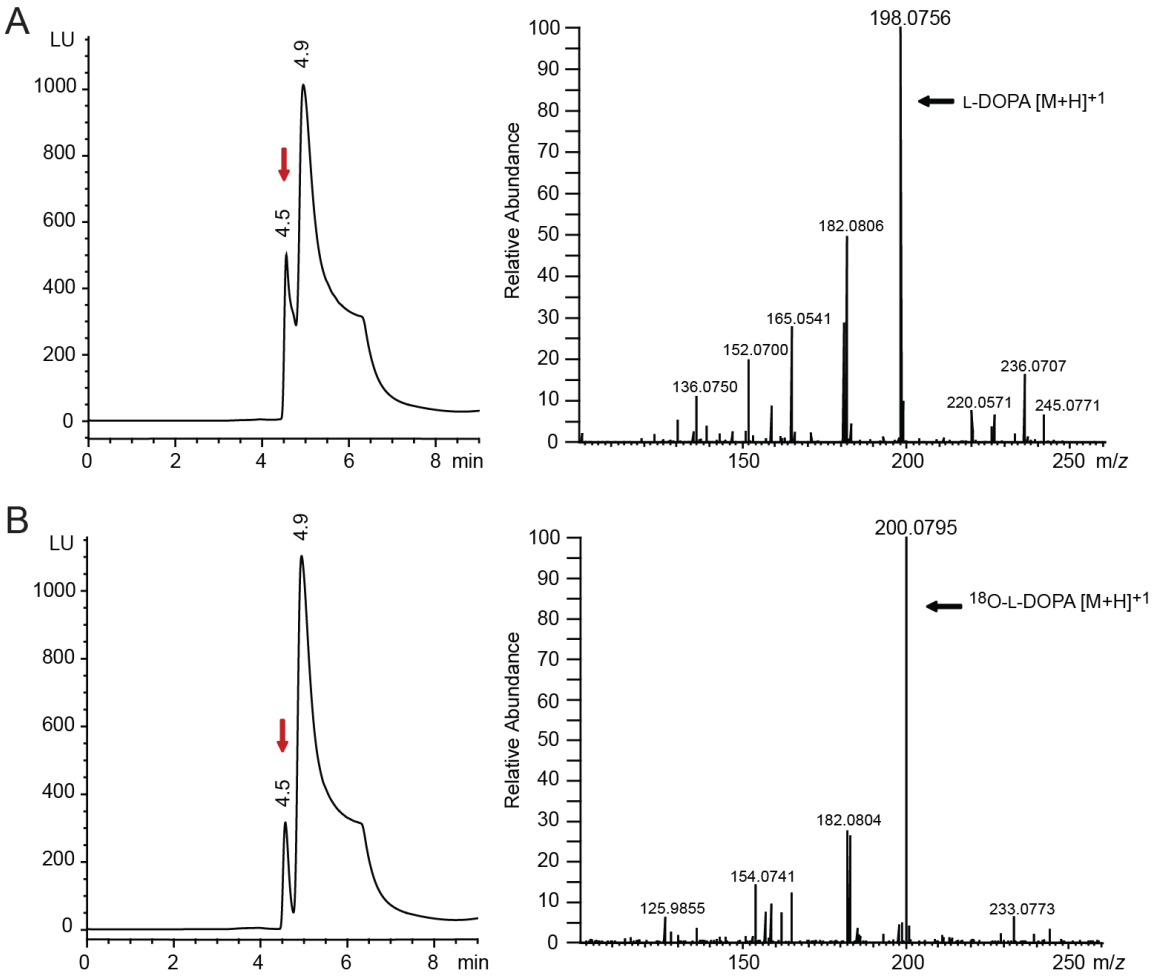

Figure 4-11. HPLC-FLD chromatograms with corresponding ESI-FT-MS spectra of the L-DOPA product (T_R 4.5 min) from Orf13 reactions catalyzed by (A) H_2O_2 and (B) $H_2{}^{18}O_2$; HPLC-FLD λ_{EX} 281 nm, λ_{EM} 314 nm; L-tyrosine (T_R 4.9 min).

Proposed mechanism of L-tyrosine hydroxylation. A possible mechanism of L-tyrosine hydroxylation for Orf13 may share the initial steps of the classic heme peroxidase catalytic cycle up to the formation of Compound I (Scheme 4-1) (*95, 105, 106*). Compound I is also an intermediate for aromatic hydroxylation catalyzed by cytochrome P450 enzymes for the oxygen dependent reaction and the peroxide shunt pathway (*29, 62*). This intermediate has also been proposed in the hydrogen peroxide dependent hydroxylation reactions of heme-thiolate peroxygenases (*29, 107*). These

enzymes function more like heme peroxidases in their use of hydrogen peroxide as the oxygen source but are more similar to cytochrome P450s based on their substrate specificity and thiolate-ligated heme-iron (*29, 107, 108*). Orf13 likely represents the first heme-histidyl enzyme and serves as a mechanistic bridge between heme peroxidases and cytochrome P450 enzymes.

Scheme 4-1. Proposed mechanism of *ortho*-hydroxylation of L-tyrosine by Orf13.

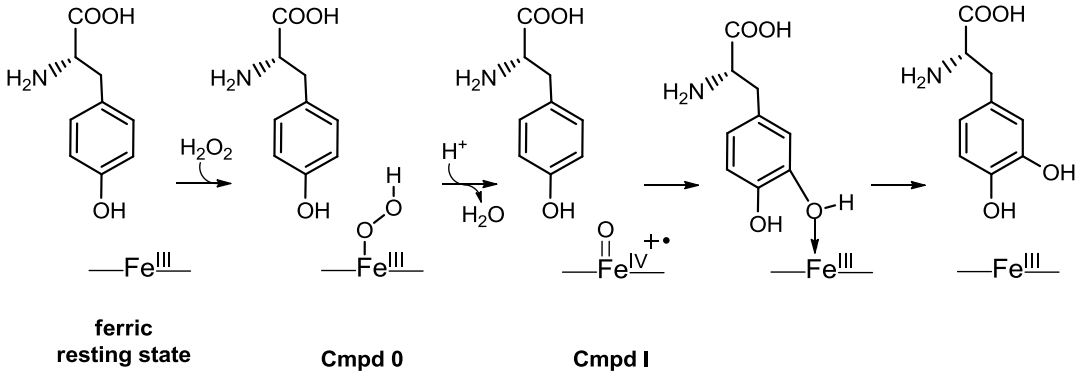

Therefore, subsequent steps after formation of Compound I may be reminiscent of the electron rebound mechanism proposed by Groves for cytochrome P450 enzymes (Scheme 4-1) (*62, 64*). Formation of the product complex with the oxygen coordinated to the iron (III) center may proceed through a hydroxyl iron (IV) substrate radical complex obtained by hydrogen abstraction by Compound I from the substrate (*64*). The fate of the reaction toward hydroxylation rather than 1-electron transfer reactions that can produce dityrosine indicates a specific reactivity of the Compound I complex which is controlled by steric and electronic interactions in the active site (*63, 109*). These interactions may

significantly reduce the life time of this radical intermediate and/or may stabilize the hydroxylation transition state.

Conclusion. Orf13 is thought to be similar to heme peroxidases with respect to a histidyl-ligand heme-iron, which has been suggested as H184 through reduced-CO (g) spectral analysis with a H184C variant. This enzyme is also able to catalyze 1-electron transfer reactions in a limited capacity that was observed by the marginal non-enzymatic production of dityrosine. Conversely, Orf13 is not similar to heme peroxidases based on its substrate specificity and stereoselectivity for L-tyrosine. Aromatic hydroxylation with *para*-phenol substrates was observed but the enzyme is more susceptible to hydrogen peroxide inactivation. This implicates a catalytic mechanism requiring the *para*-phenol substituent for hydroxylation as no turnover for L-phenylalanine or DL-*m*-tyrosine was observed. The oxygen source for tyrosine hydroxylation was identified as hydrogen peroxide with ^{18}O-L-DOPA detected by ESI-FT-MS in reactions catalyzed by $H_2{}^{18}O_2$. This implicates that Orf13 is at a mechanistic intersection between heme peroxidases and cytochrome P450 enzymes, and the chemical mechanism of L-tyrosine hydroxylation is proposed to proceed through Compound I with direct insertion of an oxygen atom from hydrogen peroxide.

Chapter 5: Conclusions

Orf13 is the first functionally identified bacterial tyrosine hydroxylase as well as the first heme peroxidase catalyzing aromatic amino acid hydroxylation with hydrogen peroxide. The work described in this dissertation provides direct characterization of Orf13, a tyrosine hydroxylase, involved in the first step of the hydropyrrole moiety biosynthesis of anthramycin (*S. refuineus*). This enzyme is a heme dependent enzyme that requires hydrogen peroxide to catalyze the *ortho*-hydroxylation of L-tyrosine to L-DOPA. The catalytic requirements of heme B and hydrogen peroxide classify Orf13 as a heme peroxidase. This classification is supported by spectroscopic analyses indicating a high spin heme-iron for ferric Orf13 and a histidyl-ligated heme-iron, which has been proposed as H184. Orf13 also displays similar catalytic activities observed with heme peroxidases; 1) a secondary catalytic pathway for tyrosine hydroxylation which is dependent on molecular oxygen and dihydroxyfumaric acid, and 2) 1-electron oxidations with hydrogen peroxide resulting in the coupling of tyrosyl radicals that non-enzymatically produce dityrosine.

Remarkably, Orf13 shares features found in heme-histidyl peroxidases (*29, 31, 95, 105, 106*), heme-thiolate peroxygenases (*29, 107, 108*), and cytochrome P450 enzymes (*29*) (Figure 5-1). In contrast to heme peroxidases yet similar to cytochrome P450s, Orf13 is substrate selective for L-tyrosine and its primary function is tyrosine hydroxylation. Identification of hydrogen peroxide as the oxygen donor for aromatic hydroxylation implicates that this enzyme is at a mechanistic intersection between heme

peroxidases and cytochrome P450 enzymes. The chemical mechanism of L-tyrosine hydroxylation is proposed to proceed through Compound I, a ferryl heme-iron intermediate. This heme intermediate is common in both mechanisms for heme peroxidases and cytochrome P450s. Formation of Compound I is expected to share the initial catalytic steps of heme peroxidases (*29, 31*), followed by the hydroxylation of tyrosine through an oxygen rebound mechanism proposed for cytochrome P450 enzymes (*62-64*).

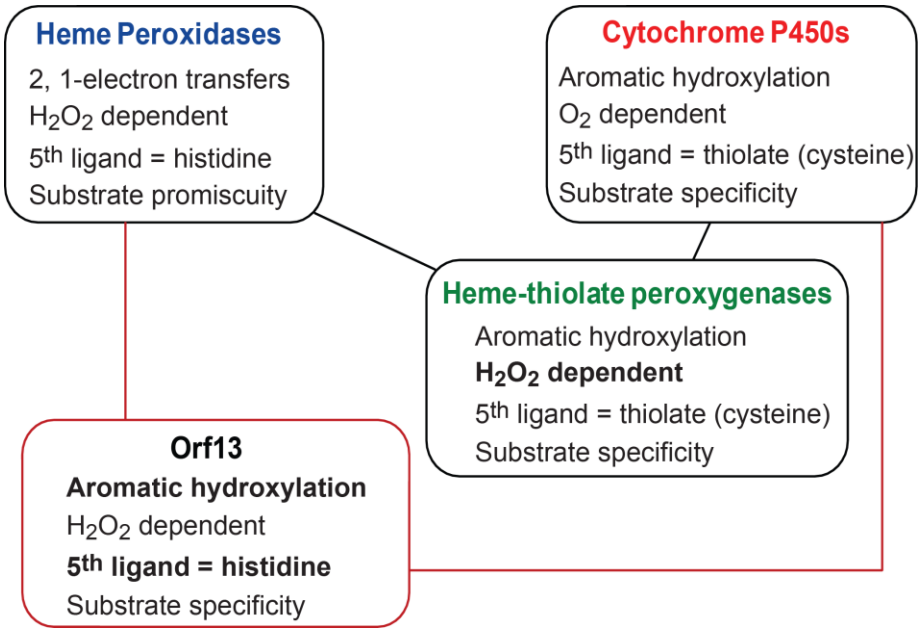

Figure 5-1. Diagram relating the key features found in heme peroxidases, cytochrome P450s, heme-thiolate peroxygenases and Orf13. Text in bold indicates unique attributes in contrast to the common qualities of heme peroxidase or cytochrome P450s.

The majority of this dissertation work has been reported in Connor, KL et al (*43*). Unpublished research includes: 1) the identification of hydrogen peroxide as the oxygen source with the $H_2{}^{18}O_2$ labeling study, 2) site-directed mutagenesis efforts of potential catalytic residues, R71 and H76, in the proposed distal site motif $R^{71}W^{72}X_3H^{76}$, and 3)

site-directed mutagenesis and spectroscopic analysis of the proximal (5^{th}) ligand candidates H140 and H184. A crystal structure of Orf13 could not be obtained at the time this dissertation was compiled. This information will be extremely valuable to provide direct identification of catalytic residues, the proximal (5^{th}) ligand residue and the overall active site environment and structural fold. It is hoped that the preliminary results described in Chapter 4 will offer supporting evidence and facilitate progress for advanced studies once structural information is available. Altogether, this information will continue to illustrate the uniqueness of this new class of bacterial tyrosine hydroxylases and guide future mechanistic studies.

At the time this dissertation was compiled and since Orf13 was first reported as a novel heme peroxidase (*43*), only one other enzyme has been reported in the literature as a heme peroxidase catalyzing aromatic hydroxylation with hydrogen peroxide (*110*). SmfD, a 3-methyltyrosine hydroxylase from the saframycin A biosynthetic gene cluster (*Streptomyces lavendulae*), was confirmed as a heme dependent enzyme requiring hydrogen peroxide to catalyze the production of 3-hydroxy-5-methyltyrosine. This enzyme is substrate specific for 3-methyltyrosine than L-tyrosine, and the oxygen source was identified as hydrogen peroxide (*110*). SfmD and Orf13 bear no resemblance to each other by global sequence alignment and neither appears as a protein hit when searching the protein database using BLAST. This indicates that SfmD and Orf13 are different types of heme peroxidases catalyzing hydrogen peroxide dependent aromatic hydroxylation. The proximal (5^{th}) ligand in SfmD has not been confirmed; however, there are conserved cysteine residues which may act as this ligand and further classify this enzyme as a heme-thiolate peroxygenase (Figure 5-1). This stresses the novelty of Orf13

as a histidyl-ligated heme peroxidase and the discovery of the first class of bacterial tyrosine hydroxylases.

Prior to the discovery and characterization of Orf13, only the non-heme iron pterin or α-KG dependent enzymes and the copper dependent tyrosinases were known to specifically catalyze the *ortho*-hydroxylation of L-tyrosine to L-DOPA (*33, 34*). Orf13 expands the known classes of tyrosine hydroxylases and is a new member representing the class of histidyl-ligated heme and hydrogen peroxide dependent enzymes. This class of bacterial tyrosine hydroxylases has thus far been identified in the biosynthetic pathways of natural products containing a hydropyrrole moiety.

Appendix

A-1. In solution quaternary structure determination of Orf13 by gel filtration

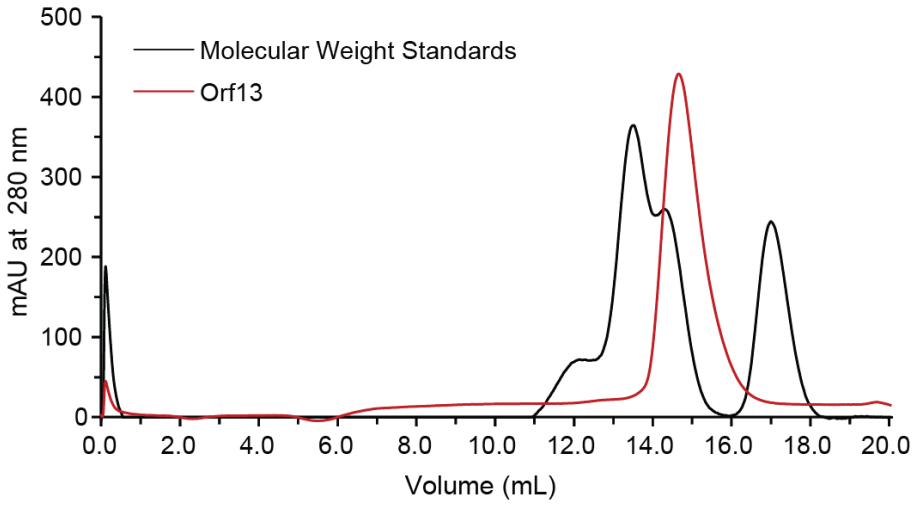

Figure A-1. FPLC chromatogram of molecular weight standards (black trace); aldolase (158 kDa; V_E 12.1 min), conalbumin (75 kDa; V_E 13.5 min), ovalbumin (44 kDa; V_E 14.2 min), and ribonuclease A (13.7 kDa; V_E 17.0 min). The quaternary structure of Orf13 (V_E 14.6 min; red trace) was calculated as 37.9 kDa, indicating a monomer based on the predicted 33.6 kDa molecular weight. Abbreviation: elution volume, V_E.

A-2. MALDI-TOF-MS of Orf13 for protein monoisotopic mass

The average monoisotopic mass of purifed native Orf13 was measured in 3 independent samples by MALDI-TOF-MS (Kratos AXIMA-CFR MALDI-TOFMS; Kratos Analytical Inc., Manchester, UK) within 10 shots at 110 V with 200 profiles collected in a mass range of 0-70,000 m/z. Desalted Orf13 (20 µM) was spotted on the MALDI plate using the sandwich method (bottom to top): 1 µL sinapic acid (10 mg/mL in 70:30 (v/v) acetonitrile (ACN): 0.1% formic acid), 1 µL sample and 0.75 µL sinapic acid (10 mg/mL in 70:30 (v/v) ACN: 0.1% formic acid). Protein standards (10 µM each) of apomyoglobin (16,952 Da) and albumin (66,430 Da) (Sigma ProteoMass^{TM} Peptide and Protein MALDI-MS Calibration Kit; Cat No. MSCAL1) were also prepared on the MALDI plate in the same manner as the Orf13 sample. The observed m/z peaks were corrected to match the average mass of each standard sample to calibrate the instrument.

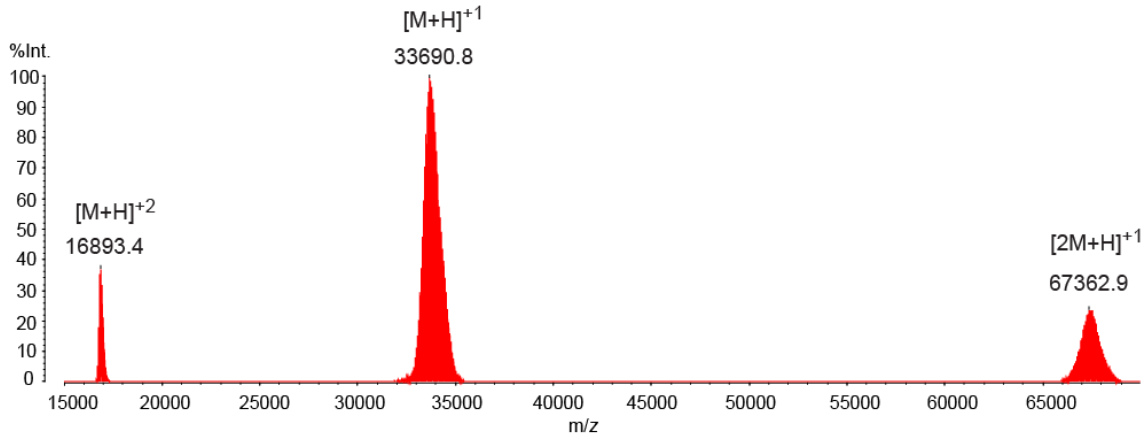

Figure A-2. MALDI-TOF-MS of native Orf13 from one independent sample. The singly charged peak of 33,690.8 m/z and doubly charged peak 16,893.4 m/z represent the monomeric mass of the enzyme (predicted mass of 33,625 Da). The peak of 67,362.9 m/z is likely a singly charged dimer species. The average monoisotopic mass of Orf13 calculated from all 3 independent sample is m/*z* 33,676 ± 58 Da.

A-3. Pyridine hemochromagen spectra of Orf13 for heme B quantitation

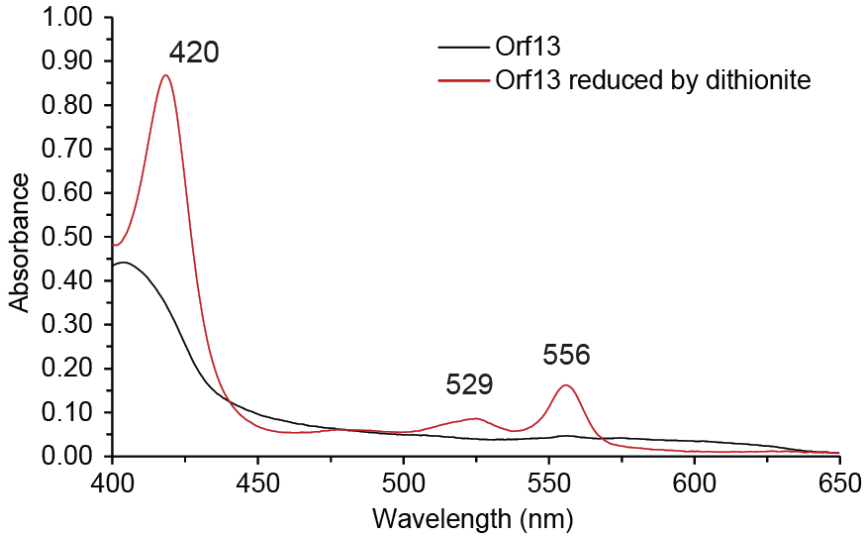

Figure A-3. Visible absorption spectra of the pyridine hemochromagen assay to quantitate the amount of heme B bound to Orf13. The basic pyridine solution containing Orf13 (black trace) is reduced with dithionite (red trace) to produce the 556 nm band that is used for the quantitation of heme B in the protein sample, as described (*40*).

A-4. HPLC co-injection of protoporphyrin IX (PPIX) with Orf13

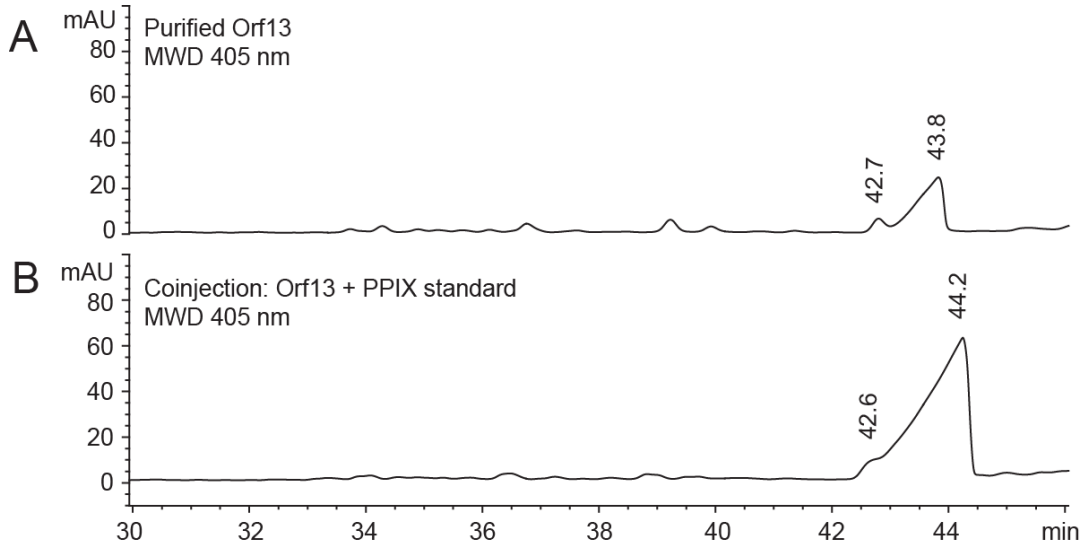

Figure A-4. HPLC chromatograms for porphyrin detection: (A) Supernatant of denatured Orf13 sample; (B) Co-injection of the sample shown in A with PPIX standard.

A-5. Identification of protoporphyrin IX (PPIX) bound to Orf13 by ESI-MS/MS.

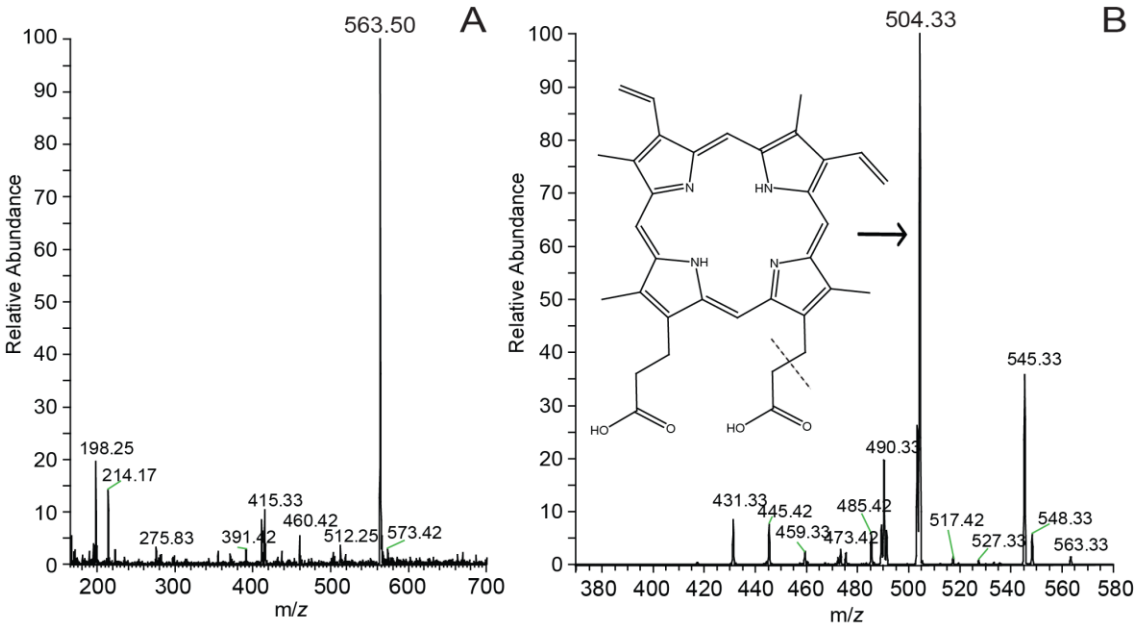

Figure A-5. (A) ESI-MS of peak (T_R 44 min, Figure 2-4A) collected from HPLC of the denatured Orf13 sample. The singly charged precursor ion m/*z* 563.5 is the same precursor ion m/z observed with PPIX standard sample collected from HPLC at 44 minutes and is in agreement with the MW of PPIX; (B) The ESI-MS/MS fragmentation of m/*z* 563.5 precursor ion generated a predominant product ion peak at 504.3 m/*z*. This mass is 59 amu less than the precursor ion and corresponds to the loss of $–CH_2COOH$ from one of the propanoic acid groups of the porphyrin ring. The same fragmentation pattern was observed with the PPIX standard sample. Figure was modified from Connor, KL et al (*43*).

A-6. HPLC-FLD of the Orf13 activity assay in the presence of hydrogen peroxide.

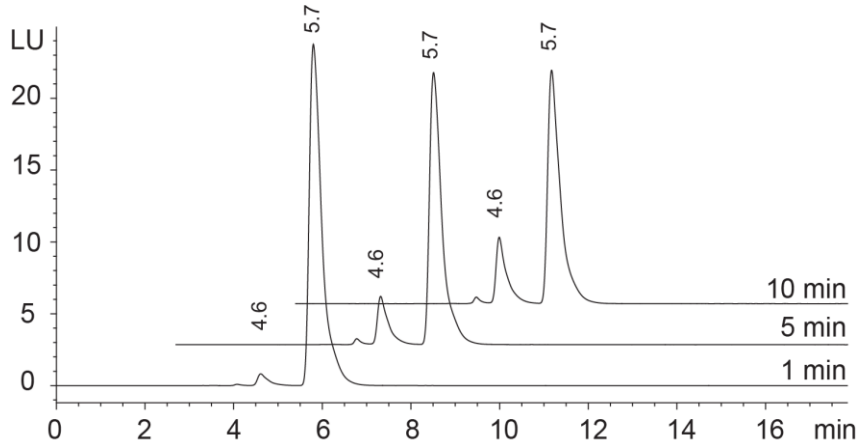

Figure A-6. HPLC-FLD chromatograms of the Orf13 activity assay in the presence of hydrogen peroxide. Final assay conditions: 2.5 μM Orf13 (76% heme B occupancy), 1 mM L-tyrosine and 0.1 mM H_2O_2 in 50 mM sodium phosphate (pH 8.0) at 37 °C. L-DOPA production was observed by an increase of the peak at 4.6 minutes. Average retention times of L-DOPA and L-tyrosine standards are 4.5 and 5.5 minutes, respectively. Figure was modified from Connor, KL et al (*43*).

A-7. Michaelis-Menten steady-state kinetic analysis of L-tyrosine for L-tyrosine hydroxylation by Orf13.

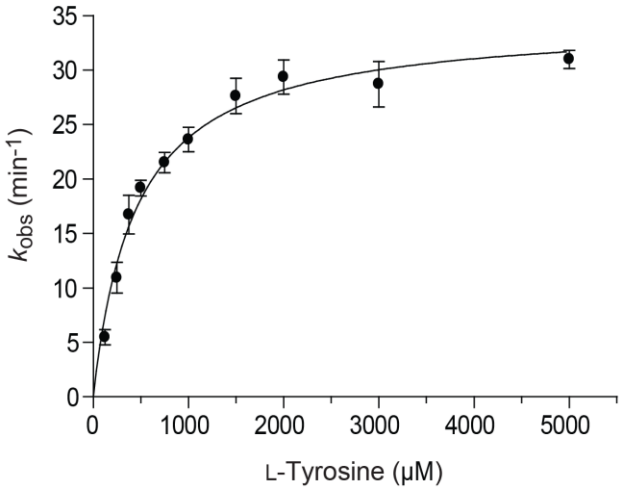

Substrate: L-Tyrosine	Non-linear Fit
Best-fit values	
KCAT (min^{-1})	34.55
KM (μM)	452.7
Standard Error	
KCAT (min^{-1})	1.128
KM (μM)	50.15
95% Confidence Intervals	
KCAT (min^{-1})	31.95 to 37.15
KM (μM)	337.0 to 568.3
Goodness of Fit	
Degrees of Freedom	8
R^2	0.9799
Absolute Sum of Squares	12.92
Sy.x	1.271
Data	
Number of X values	10
Number of Y replicates	1
Total number of values	10
Number of missing values	0

Figure A-7. Michaelis-Menten curve of L-tyrosine hydroxylation by Orf13 for the hydrogen peroxide dependent reaction at fixed variable concentrations of L-tyrosine and a fixed H_2O_2 (500 μM) concentration. Assay conditions: Orf13 was pre-incubated for 5 min at 37 °C with L-tyrosine followed by addition of H_2O_2 to initiate the reaction. The reaction was carried out for 4 min at 37 °C with L-DOPA formation was measured by the L-DOPA colorimetric assay. Statistics of non-linear fitting of the data to the Michaelis-Menten equation (Equation 3-1) by Prism (GraphPad) are displayed to the right of the curve. Figure was modified from Connor, KL et al (*43*).

A-8. Michaelis-Menten steady-state kinetic analysis of hydrogen peroxide at 2 mM L-tyrosine for L-tyrosine hydroxylation by Orf13.

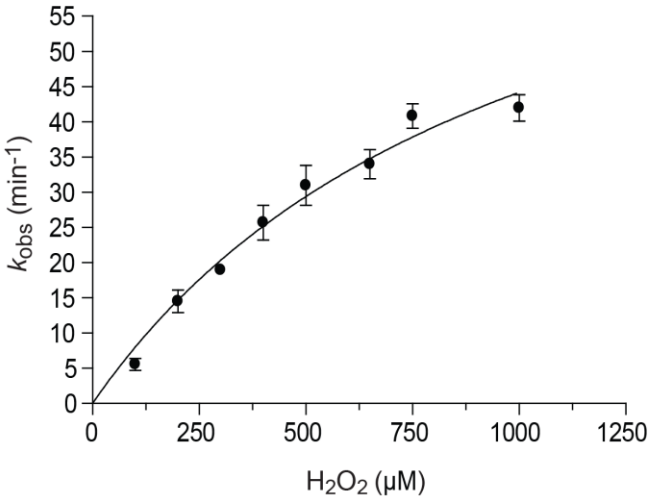

Substrate: H_2O_2	Non-linear fit
Best-fit values	
KCAT (min^{-1})	89.11
KM (μM)	1017
Standard Error	
KCAT (min^{-1})	14.3
KM (μM)	264.4
95% Confidence Intervals	
KCAT (min^{-1})	54.12 to 124.1
KM (μM)	370.1 to 1664
Goodness of Fit	
Degrees of Freedom	6
R^2	0.9785
Absolute Sum of Squares	24.95
Sy.x	2.039
Data	
Number of X values	8
Number of Y replicates	1
Total number of values	8
Number of missing values	0

Figure A-8. Michaelis-Menten curve of L-tyrosine hydroxylation by Orf13 for the hydrogen peroxide dependent reaction at fixed variable concentrations of H_2O_2 and a fixed L-tyrosine (2 mM) concentration. Assay conditions: Orf13 was pre-incubated for 5 min at 37 °C with L-tyrosine followed by addition of H_2O_2 to initiate the reaction. The reaction was carried out for 4 min at 37 °C with L-DOPA formation was measured by the L-DOPA colorimetric assay. Statistics of non-linear fitting of the data to the Michaelis-Menten equation (Equation 3-1) by Prism (GraphPad) are displayed to the right of the curve. Figure was modified from Connor, KL et al (*43*).

A-9. Michaelis-Menten steady-state kinetic analysis of hydrogen peroxide at 0.45 mM and 5 mM L-tyrosine for L-tyrosine hydroxylation by Orf13.

General assay conditions: Orf13 was pre-incubated for 5 min at 37 °C with L-tyrosine followed by addition of H_2O_2 to initiate the reaction. The reaction was carried out for 4 min at 37 °C with L-DOPA formation was measured by the L-DOPA colorimetric assay.

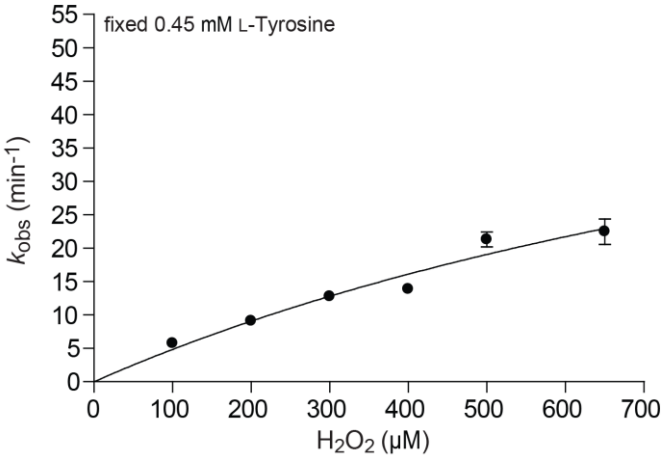

Substrate: H_2O_2	Non-linear fit
Best-fit values	
KCAT (min^{-1})	71.65
KM (µM)	1380
Standard Error	
KCAT (min^{-1})	37.62
KM (µM)	971.7
95% Confidence Intervals	
KCAT (min^{-1})	-32.78 to 176.1
KM (µM)	-1318 to 4077
Goodness of Fit	
Degrees of Freedom	4
R^2	0.9486
Absolute Sum of Squares	11.21
Sy.x	1.674
Data	
Number of X values	6
Number of Y replicates	1
Total number of values	6
Number of missing values	0

Figure A-9A. Michaelis-Menten curve of L-tyrosine hydroxylation by Orf13 for the hydrogen peroxide dependent reaction at fixed variable concentrations of H_2O_2 and a fixed L-tyrosine (0.45 mM) concentration. Statistics of non-linear fitting of the data to the Michaelis-Menten equation (Equation 3-1) by Prism (GraphPad) are displayed to the right of the curve. Steady-state analysis at 0.45 mM L-tyrosine (a non-saturating condition) was limited to a maximal H_2O_2 concentration of 650 µM since inactivation of Orf13 by H_2O_2 was observed.

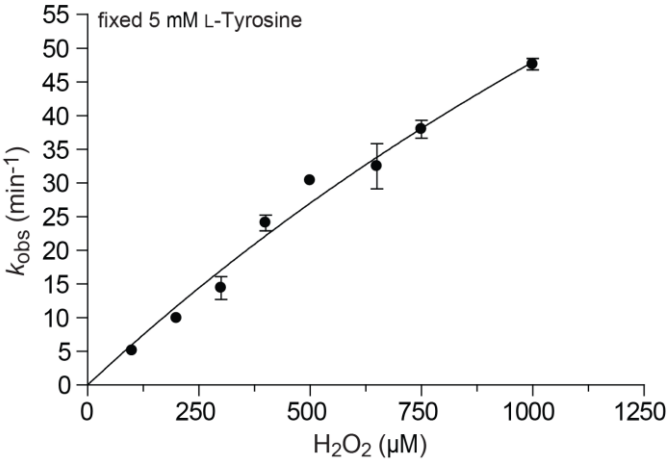

Substrate: H_2O_2	Non-linear fit
Best-fit values	
KCAT (min^{-1})	214.4
KM (μM)	3472
Standard Error	
KCAT (min^{-1})	97.7
KM (μM)	1906
95% Confidence Intervals	
KCAT (min^{-1})	-24.71 to 453.4
KM (μM)	-1192 to 8137
Goodness of Fit	
Degrees of Freedom	6
R^2	0.9815
Absolute Sum of Squares	27.8
Sy.x	2.153
Data	
Number of X values	8
Number of Y replicates	1
Total number of values	8
Number of missing values	0

Figure A-9B. Michaelis-Menten curve of L-tyrosine hydroxylation by Orf13 for the hydrogen peroxide dependent reaction at fixed variable concentrations of H_2O_2 and a fixed L-tyrosine (5 mM) concentration. Statistics of non-linear fitting of the data to the Michaelis-Menten equation (Equation 3-1) by Prism (GraphPad) are displayed to the right of the curve.

Table A-9. Steady-State Kinetic Rate Constants of H_2O_2 for L-Tyrosine Hydroxylation by Orf13[a]

Fixed L-Tyrosine (mM)	K_m[c] (mM)	k_{cat} (s^{-1})	k_{cat}/K_m (s^{-1} M^{-1})
0.45	1.2 ± 0.3	1.0 ± 0.2	(0.90 ± 0.05) x 10^3
2[b]	1.0 ± 0.3	1.5 ± 0.3	(1.5 ± 0.2) x 10^3
5	3.6 ± 0.9	3.7 ± 0.7	(1.0 ± 0.1) x 10^3

[a]Assays were performed at 37 °C with 0.3 – 1 μM Orf13 (75% heme B occupancy) in 100 mM sodium phosphate (pH 8.0). L-DOPA formation was measured using the L-DOPA colorimetric assay. Data are not normalized to heme B occupancy.
[b]Reported steady-state kinetic rate constants for H_2O_2 (*43*).
[c]These values are apparent K_m constants at the concentrations of L-tyrosine indicated.

A-10. HPLC-FLD of Orf13 activity assay in the presence of L-ascorbate and DHFA.

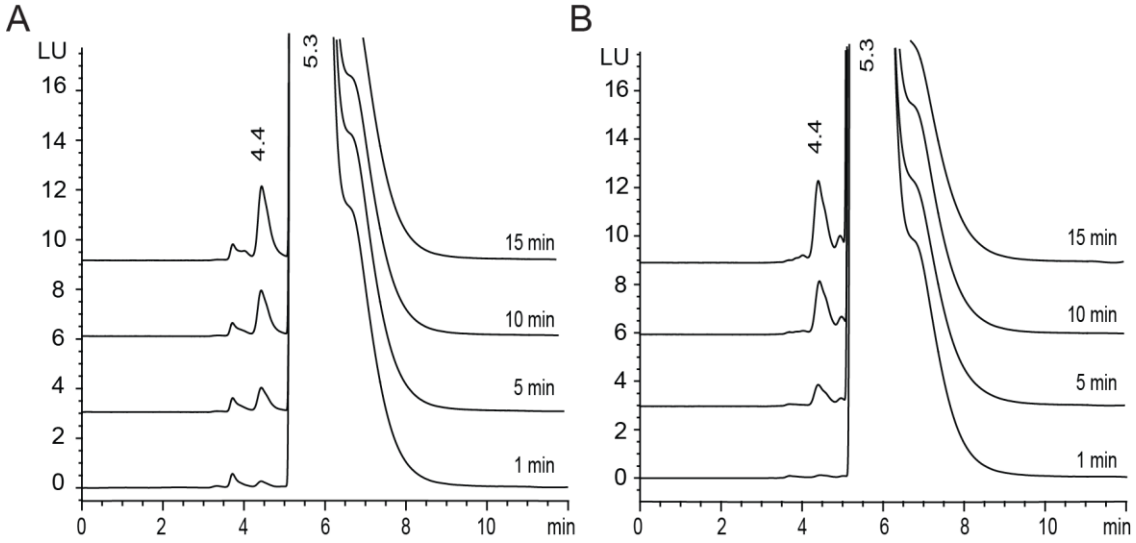

Figure A-10. HPLC-FLD chromatograms of L-tyrosine hydroxylation by Orf13 in the presence of (A) L-ascorbate or (B) dihydroxyfumaric acid. Average retention times of L-DOPA and L-tyrosine standards are 4.5 and 5.5 minutes, respectively. Figure was modified from Connor, KL et al (*43*).

A-11. Fluorescence excitation and emission spectra of heme B bound to Orf13.

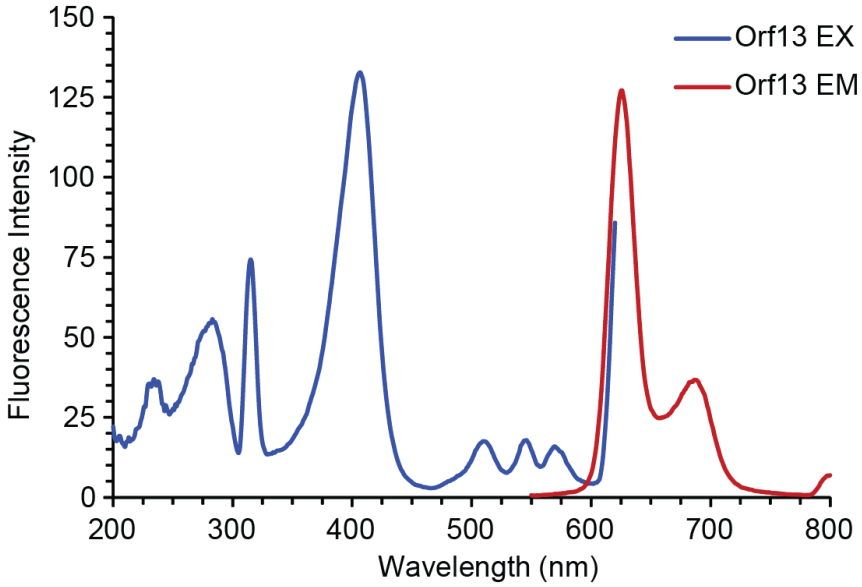

Figure A-11. Fluorescence excitation (blue trace) and emission (red trace) spectra of Orf13. Sample conditions: 2.5 μM Orf13 (100% heme B) in 20 mM sodium phosphate (pH 8.0) at 25 °C. λ_{EX} maxima (blue trace): 280 nm, 315 nm, 404 nm, 501 nm, 540 nm and 563 nm; λ_{EM} maxima (red trace): 625 nm and 680 nm.

A-12. Fluorescence equilibrium binding analysis of L-tyrosine with Orf13.

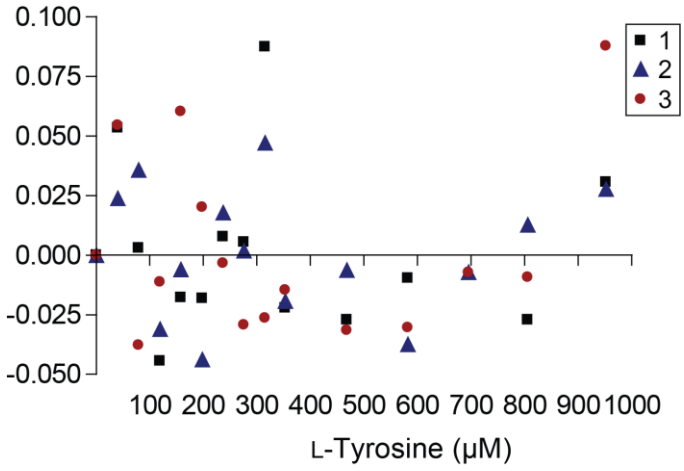

Ligand: L-Tyrosine	Non-linear fit
Best-fit values	
BMAX	1.028
KD (μM)	149.5
Std. Error	
BMAX	0.02408
KD (μM)	11.36
95% Confidence Intervals	
BMAX	0.9762 to 1.080
KD (μM)	125.0 to 174.0
Goodness of Fit	
Degrees of Freedom	13
R^2	0.9906
Absolute Sum of Squares	0.008509
Sy.x	0.02558
Constraints	
BMAX	BMAX > 0.0
KD	KD > 0.0
Data	
Number of X values	15
Number of Y replicates	1
Total number of values	15
Number of missing values	0

Figure A-12. Plot of residuals for the equilibrium binding data across 3 independent ligand titration experiments for L-tyrosine with Orf13. The random scattering of the data indicates the data fit to the one site binding model (Equation 4-2) is in agreement with the model. The statistics of the data (averaged across the 3 independent titration experiments) to Equation 4-2 using Prism (GraphPad) are displayed to the right of the residual plot.

A-13. Fluorescence equilibrium binding data and analysis of L-DOPA with Orf13.

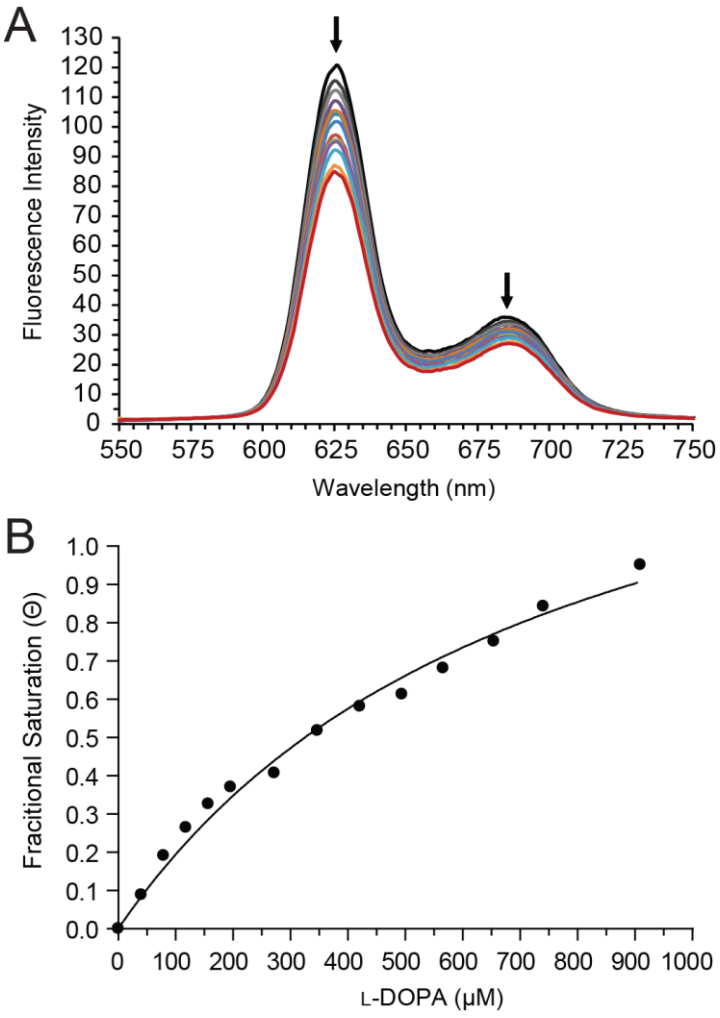

Ligand: L-DOPA	Non-linear fit
Best-fit values	
BMAX	1.657
KD (μM)	751.2
Std. Error	
BMAX	0.1435
KD (μM)	111.6
95% Confidence Intervals	
BMAX	1.344 to 1.969
KD (μM)	507.9 to 994.5
Goodness of Fit	
Degrees of Freedom	12
R^2	0.9885
Absolute Sum of Squares	0.01208
Sy.x	0.03172
Constraints	
BMAX	BMAX > 0.0
KD	KD > 0.0
Data	
Number of X values	14
Number of Y replicates	1
Total number of values	14
Number of missing values	0

Figure A-13A. Equilibrium ligand binding experiment for L-DOPA with Orf13 (100% heme B) in 20 mM sodium phosphate (pH 8.0) at 25 °C; (A) The fluorescence emission spectra of heme B bound to Orf13 upon titration of L-DOPA; (B) Direct plot of the average fractional saturation for L-DOPA with Orf13 based on the change of λ_{EM} 625 nm. The statistics of the non-linear fit of the data to Equation 4-2, one site binding model for dissociation constant of a ligand, using Prism (GraphPad) are displayed to the right of the curve.

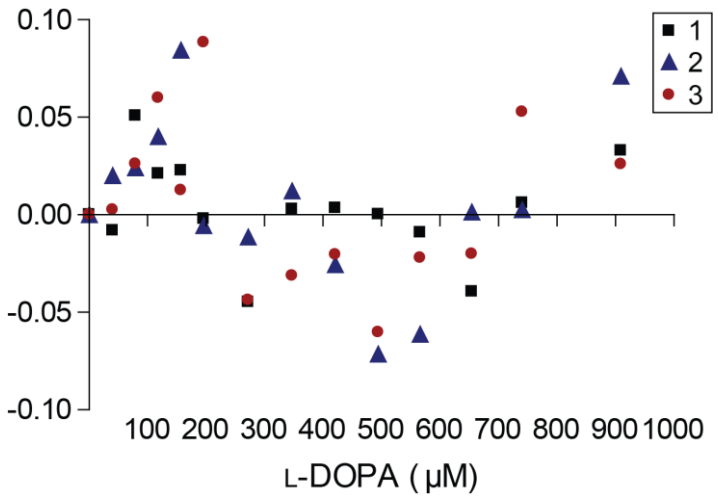

Figure A-13B. Plot of residuals for the equilibrium binding data across 3 independent ligand titration experiments for L-DOPA with Orf13. The residuals are not randomly scattered and display a "U" shaped trend. This indicates that the data fit to the one site binding model (Equation 4-2) are not in agreement with this model and the value calculated for the dissociation constant is not accurate.

A-14. Fluorescence equilibrium binding data and analysis of L-phenylalanine with Orf13.

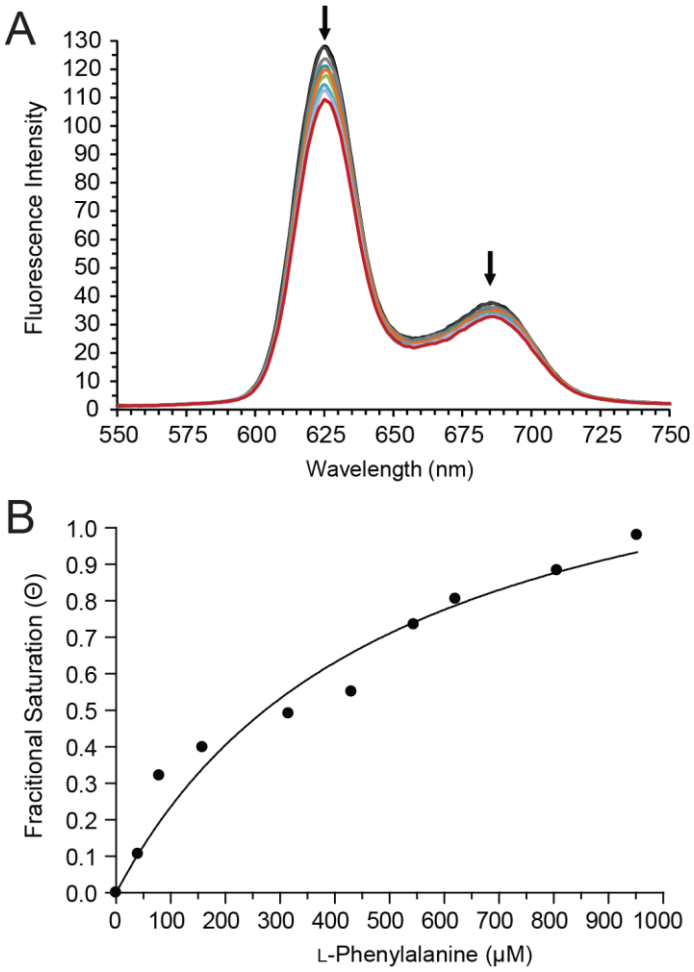

Ligand: L-Phenylalanine	Non-linear fit
Best-fit values	
BMAX	1.429
KD (μM)	504.9
Std. Error	
BMAX	0.2143
KD (μM)	161.4
95% Confidence Intervals	
BMAX	0.9348 to 1.923
KD (μM)	132.6 to 877.2
Goodness of Fit	
Degrees of Freedom	8
R^2	0.9619
Absolute Sum of Squares	0.03687
Sy.x	0.06789
Constraints	
BMAX	BMAX > 0.0
KD	KD > 0.0
Data	
Number of X values	10
Number of Y replicates	1
Total number of values	10
Number of missing values	0

Figure A-14A. Equilibrium ligand binding experiment for L-phenylalanine with Orf13 (100% heme B) in 20 mM sodium phosphate (pH 8.0) at 25 °C. (A) The fluorescence emission spectra of heme B bound to Orf13 upon titration of L-phenylalanine. (B) Direct plot of the average fractional saturation for L-phenylalanine with Orf13 based on the change of λ_{EM} 625 nm. The statistics of the non-linear fit of the data to Equation 4-2, one site binding model for dissociation constant of a ligand, using Prism (GraphPad) are displayed to the right of the curve.

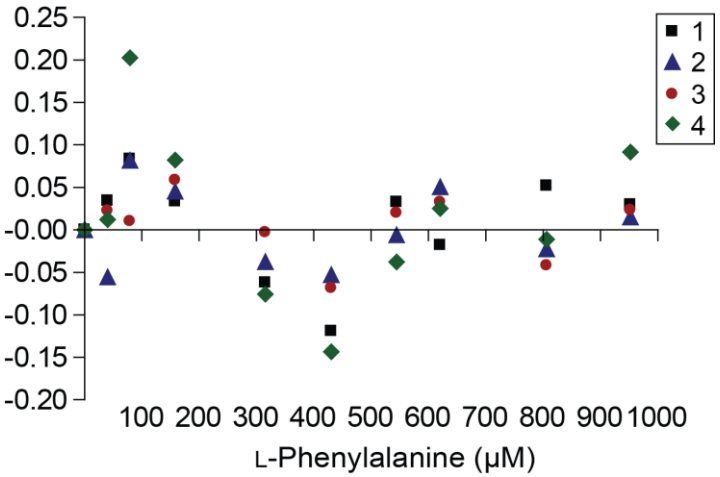

Figure A-14B. Plot of residuals for the equilibrium binding data across 4 independent ligand titration experiments for L-phenylalanine with Orf13. The residuals are not randomly scattered and display a "W" shaped trend. This indicates that the data fit to the one site binding model (Equation 4-2) are not in agreement with this model and the value calculated for the dissociation constant is not accurate.

A-15. Absorbance equilibrium binding data and analysis of imidazole with Orf13.

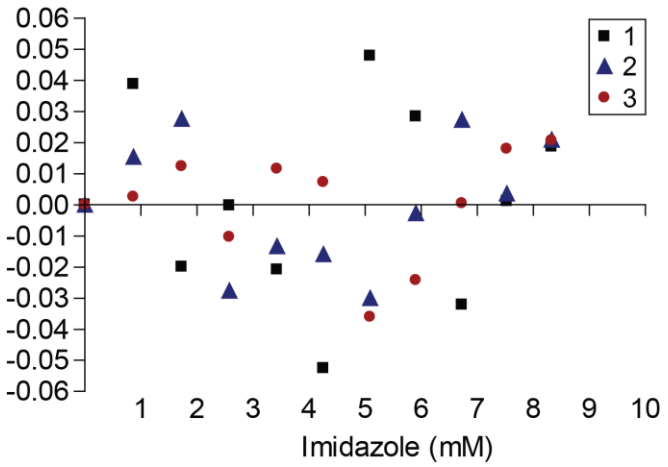

Ligand: Imidazole	Non-linear fit
Best-fit values	
BMAX	1.157
KD (mM)	1.514
Std. Error	
BMAX	0.01449
KD (mM)	0.07081
95% Confidence Intervals	
BMAX	1.124 to 1.190
KD (mM)	1.354 to 1.675
Goodness of Fit	
Degrees of Freedom	9
R^2	0.9983
Absolute Sum of Squares	0.001481
Sy.x	0.01283
Constraints	
BMAX	BMAX > 0.0
KD	KD > 0.0
Data	
Number of X values	11
Number of Y replicates	1
Total number of values	11
Number of missing values	0

Figure A-15. Plot of residuals for the equilibrium binding data across 3 independent ligand titration experiments for imidazole with Orf13. The random scattering of the data indicates the data fit to the one site binding model (Equation 4-2) is in agreement with the model. The statistics of the data (averaged across the 3 independent titration experiments) to Equation 4-2 using Prism (GraphPad) are displayed to the right of the residual plot.

A-16. HPLC-FLD chromatogram of dityrosine, L-tyrosine and L-DOPA for the assessment of dityrosine production with Orf13.

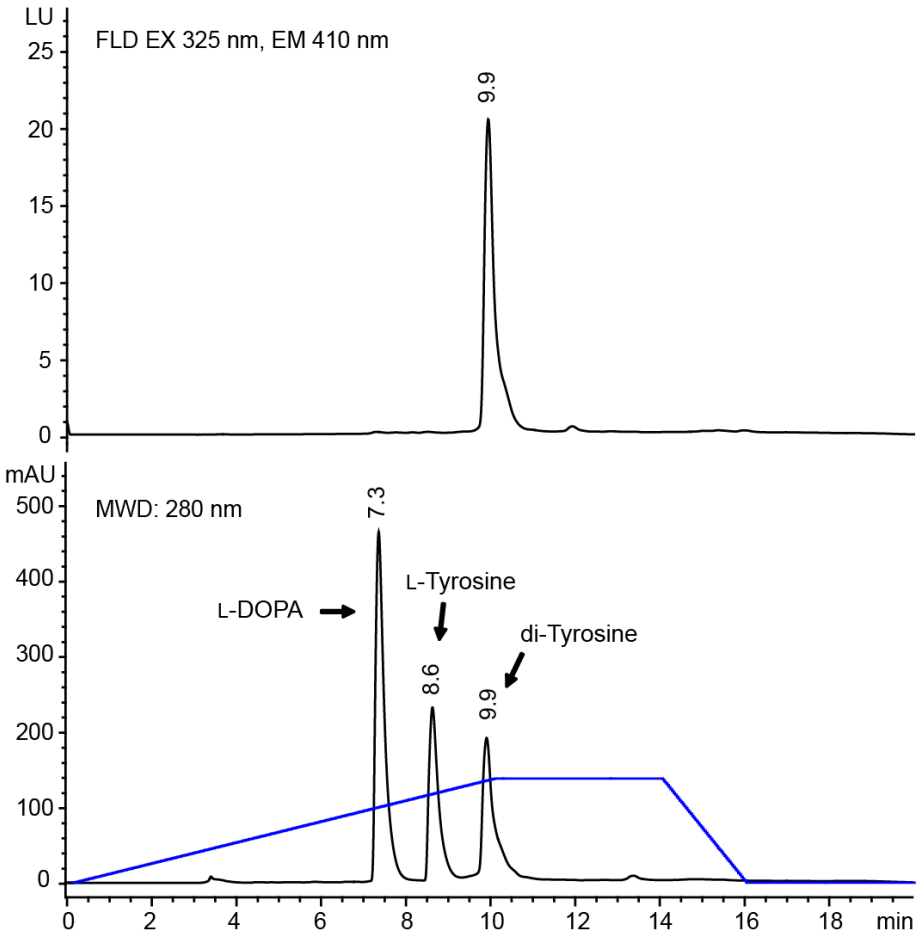

Figure A-16. HPLC chromatograms of chemical standards to assess dityrosine production by Orf13. The linear gradient of methanol with 0.1% TFA is shown in blue. Chemical standards: 100 µM L-DOPA (T_R 7.3 min), 100 µM L-tyrosine (T_R 8.6 min) and 50 µM dityrosine (T_R 9.9 min) in 100 mM sodium phosphate (pH 8.0).

A-17. HPLC-FLD chromatogram of Orf13 pre-incubated with H_2O_2 for assesment of dityrosine production.

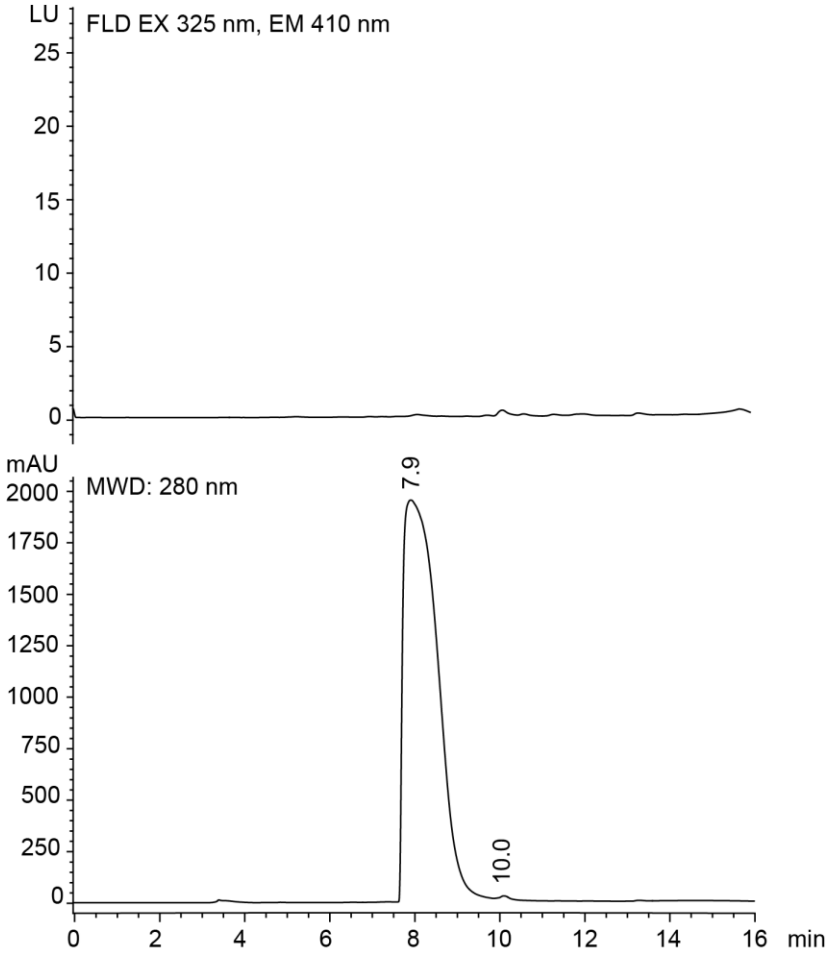

Figure A-17. HPLC chromatograms for assessment of dityrosine production by Orf13. Assay condition: 30 minute time point of Orf13 (3 μM; 100% heme B) pre-incubated with hydrogen peroxide (500 μM final) followed by addition of L-tyrosine (5 mM final; T_R 7.9 min) in 100 mM sodium phosphate at 37 °C.

A-18. Substrate analogues to evaluate substrate requirements for aromatic hydroxylation by Orf13.

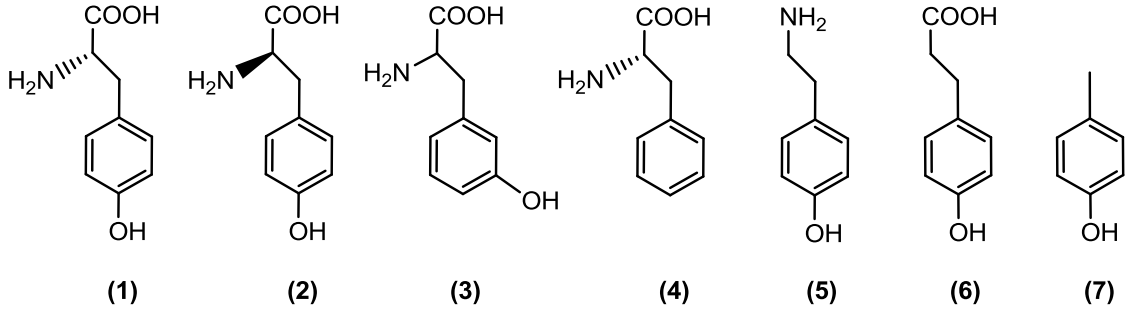

Figure A-18. Chemical structures of L-tyrosine (**1**) and substrate analogues (**2-7**) used to evaluate the substrate specificity of the aromatic hydroxylation reaction by Orf13; D-tyrosine (**2**), DL-*m*-tyrosine (**3**), L-phenylalanine (**4**), tyramine (**5**), 3-(4-hydroxyphenyl) propanoic acid, 3-HPPA, (**6**) and *p*-cresol (**7**).

A-19. Catechol-nitrite complexes of substrate analogues hydroxylated by Orf13.

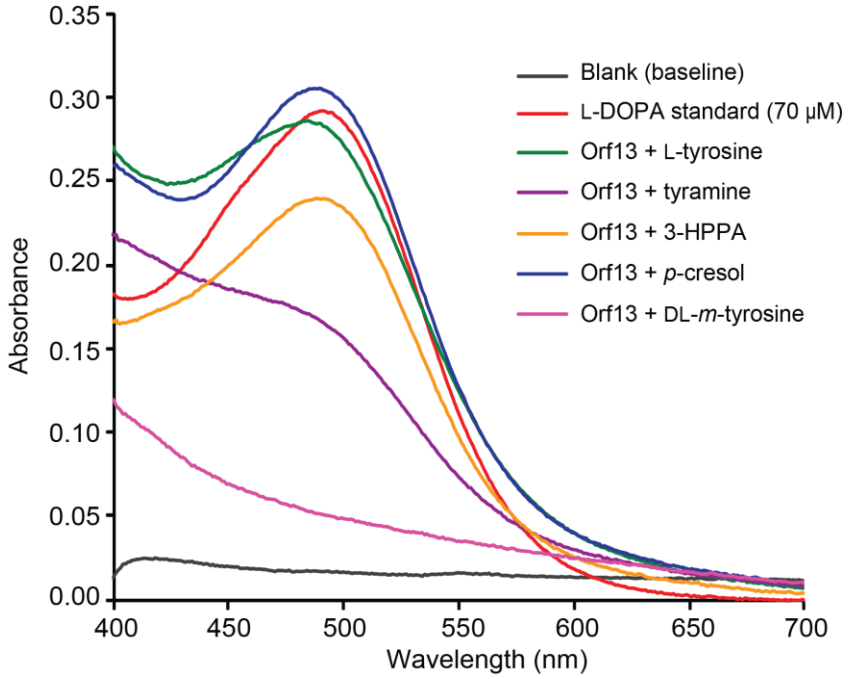

Figure A-19. Visible absorption spectra of catechol-nitrite complexes for catechol product formation by the aromatic hydroxylation of L-tyrosine and phenol substrate analogues by Orf13 in the presence of hydrogen peroxide. Final assay conditions: 1.5 µM Orf13 (48% heme B occupancy), 5 mM L-tyrosine or substrate analogue, 500 µM H_2O_2 in 100 mM sodium phosphate (pH 8.0). All reactions were performed at 37 °C, quenched at 2 minutes and underwent the DOPA colorimetric assay work described in Chapter 3. The substrate analogue 3-(4-hydroxyphenyl) propanoic acid is abbreviated as 3-HPPA. Figure was modified from Connor, KL et al (*43*).

A-20. Turnover comparison of D vs L-tyrosine to assess substrate stereoselectivity by Orf13.

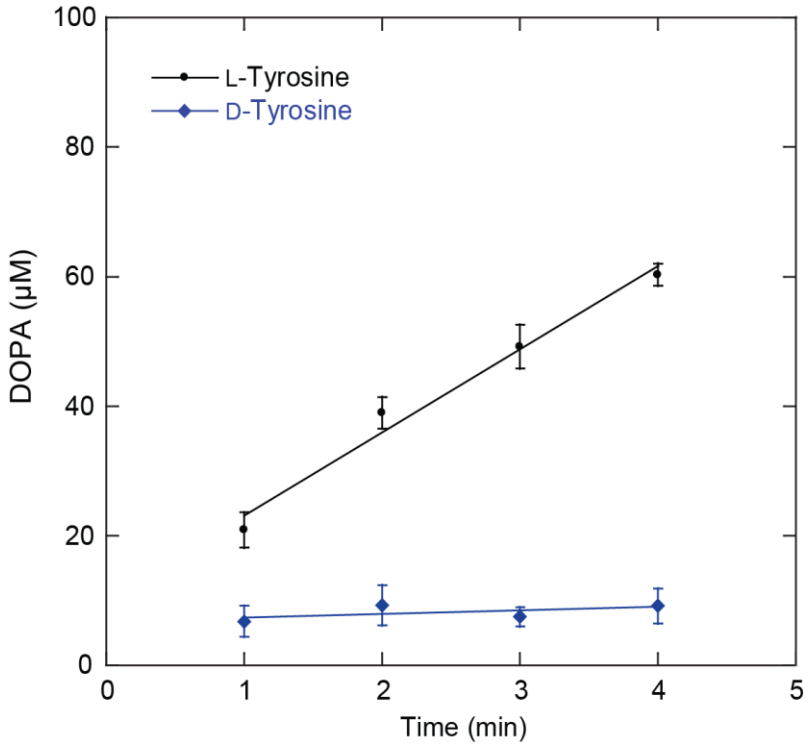

Figure A-20. Progress curves of tyrosine hydroxylation for L-tyrosine (●) or D-tyrosine (♦) by Orf13. Assay conditions: 0.75 μM Orf13 (48% heme B), 5 mM (L or D) tyrosine and 500 μM H_2O_2 in 100 mM sodium phosphate (pH 8.0) at 37 °C. Orf13 was pre-incubated with tyrosine for 5 min at 37 °C followed by addition to H_2O_2 to initiate the reaction. DOPA formation was measured by the DOPA colorimetric assay.

Bibliography

1. Ferlay J, Shin HR, Bray F, Forman D, Mathers C, and Parkin DM. Estimates of global cancer prevalence in 2008 for 27 sites in the adult population, in *GLOBOCAN 2008 v1.2, Cancer Incidence and Mortality Worldwide: IARC CancerBase No. 10*, International Agency for Research on Cancer; 2010. Available from: http://globocan.iarc.fr, Lyon, France

2. Newman, D. J., and Cragg, G. M. (2012) Natural products as sources of new drugs over the 30 years from 1981 to 2010, *J. Nat. Prod. 75*, 311-335.

3. Gerratana, B. (2012) Biosynthesis, synthesis, and biological activities of pyrrolobenzodiazepines, *Med. Res. Rev. 32*, 254-293.

4. Tendler, M. D., and Korman, S. (1963) `*Refuin*' : a non-cytotoxic carcinostatic compound proliferated by a thermophilic actinomycete, *Nature 199*, 501-501.

5. Hartley, J. A. (2011) The development of pyrrolobenzodiazepines as antitumour agents, *Expert Opinion on Investigational Drugs 20*, 733-744.

6. Puzanov, I., Lee, W., Chen, A. P., Calcutt, M. W., Hachey, D. L., Vermeulen, W. L., Spanswick, V. J., Liao, C.-Y., Hartley, J. A., Berlin, J. D., and Rothenberg, M. L. (2011) Phase I pharmacokinetic and pharmacodynamic study of SJG-136, a novel DNA sequence selective minor groove cross-linking agent, in advanced solid tumors, *Clinical Cancer Research 17*, 3794-3802.

7. Hu, Y., Phelan, V., Ntai, I., Farnet, C. M., Zazopoulos, E., and Bachmann, B. O. (2007) Benzodiazepine biosynthesis in *Streptomyces refuineus*, *Chem. Biol. 14*, 691-701.

8. Li, W., Chou, S., Khullar, A., and Gerratana, B. (2009) Cloning and characterization of the biosynthetic gene cluster of tomaymycin, an SJG-136 monomeric analog, *Appl. Environ. Microbiol. 75*, 2958-2963.

9. Li, W., Khullar, A., Chou, S., Sacramo, A., and Gerratana, B. (2009) Biosynthesis of sibiromycin, a potent antitumor antibiotic, *Appl. Environ. Microbiol. 75*, 2869-2878.

10. Yonemoto, I. T., Li, W., Khullar, A., Reixach, N., and Gerratana, B. (2012) Mutasynthesis of a potent anticancer sibiromycin analogue, *ACS Chemical Biology* ***Article ASAP***.

11. Kopka, M. L., Goodsell, D. S., Baikalov, I., Grzeskowiak, K., Cascio, D., and Dickerson, R. E. (1994) Crystal structure of a covalent DNA-drug adduct: anthramycin bound to C-C-A-A-C-G-T-T-G-G and a molecular explanation of specificity, *Biochemistry 33*, 13593-13610.

12. Thurston, D. E., Bose, D. S., Howard, P. W., Jenkins, T. C., Leoni, A., Baraldi, P. G., Guiotto, A., Cacciari, B., Kelland, L. R., Foloppe, M.-P., and Rault, S. (1999) Effect of A-ring modifications on the DNA-binding behavior and cytotoxicity of pyrrolo[2,1-c][1,4]benzodiazepines, *J. Med. Chem. 42*, 1951-1964.

13. Gregson, S. J., Howard, P. W., Corcoran, K. E., Barcella, S., Yasin, M. M., Hurst, A. A., Jenkins, T. C., Kelland, L. R., and Thurston, D. E. (2000) Effect of C2-exo unsaturation on the cytotoxicity and DNA-binding reactivity of pyrrolo[2,1-c][1,4]benzodiazepines, *Bioorg. Med. Chem. Lett. 10*, 1845-1847.

14. Gregson, S. J., Howard, P. W., Barcella, S., Nakamya, A., Jenkins, T. C., Kelland, L. R., and Thurston, D. E. (2000) Effect of C2/C3-endo unsaturation on the cytotoxicity and dna-binding reactivity of pyrrolo[2,1-c][1,4]benzodiazepines, *Bioorg. Med. Chem. Lett. 10*, 1849-1851.

15. Chen, Z., Gregson, S. J., Howard, P. W., and Thurston, D. E. (2004) A novel approach to the synthesis of cytotoxic C2-C3 unsaturated pyrrolo[2,1-c][and]benzodiazepines (PBDs) with conjugated acrylyl C2-substituents, *Bioorg. Med. Chem. Lett. 14*, 1547.

16. Hurley, L. H., Zmijewski, M., and Chang, C.-J. (1975) Biosynthesis of anthramycin. Determination of the labeling pattern by the use of radioactive and stable isotope techniques, *J. Am. Chem. Soc. 97*, 4372-4378.

17. Hurley, L. H. (1977) Pyrrolo(1,4)benzodiazepine antitumor antibiotics. Comparative aspects of anthramycin, tomaymycin and sibiromycin, *J. Antibiot. 30*, 349-370.

18. Hurley, L. H., Lasswell, W. L., Ostrander, J. M., and Parry, R. (1979) Pyrrolo[1,4]benzodiazepine antibiotics. Biosynthetic conversion of tyrosine to the C2- and C3-proline moieties of anthramycin, tomaymycin, and sibiromycin, *Biochemistry 18*, 4230-4237.

19. Hurley, L. H. (1980) Elucidation and formulation of novel biosynthetic pathways leading to the pyrrolo[1,4]benzodiazepine antibiotics anthramycin, tomaymycin, and sibiromycin, *Acc. Chem. Res. 13*, 263-269.

20. Witz, D. F., Hessler, E. J., and Miller, T. L. (1971) Bioconversion of tyrosine into the propylhygric acid moiety of lincomycin, *Biochemistry 10*, 1128-1133.

21. Brahme, N. M., Gonzalez, J. E., Rolls, J. P., Hessler, E. J., Mizsak, S., and Hurley, L. H. (1984) Biosynthesis of the lincomycins. 1. Studies using stable isotopes on the biosynthesis of the propyl- and ethyl-L-hygric acid moieties of lincomycins A and B, *J. Am. Chem. Soc. 106*, 7873-7878.

22. Höfer, I., Crüsemann, M., Radzom, M., Geers, B., Flachshaar, D., Cai, X., Zeeck, A., and Piel, J. (2011) Insights into the biosynthesis of hormaomycin, an exceptionally complex bacterial signaling metabolite, *Chem. Biol. 18*, 381-391.

23. Spízek, J., and Rezanka, T. (2004) Lincomycin, clindamycin and their applications, *Appl. Microbiol. Biotechnol. 64*, 455-464.

24. Rössner, E., Zeeck, A., and König, W. A. (1990) Elucidation of the structure of Hormaomycin, *Angew. Chem. Intl. Ed. 29*, 64-65.

25. Peschke, U., Schmidt, H., Zhang, H.-Z., and Piepersberg, W. (1995) Molecular characterization of the lincomycin-production gene cluster of *Streptomyces lincolnensis* 78-11, *Mol. Microbiol. 16*, 1137-1156.

26. Novotna, J., Honzatko, A., Bednar, P., Kopecky, J., Janata, J., Spizek, J. (2004) L-3,4-Dihydroxyphenyl alanine-extradiol cleavage is followed by intramolecular cyclization in lincomycin biosynthesis, *Eur. J. Biochem. 271*, 3678-3683.

27. Neusser, D., Schmidt, H., Spizek, J., Novotna, J., U., P., Kaschabeck, S., Tichy, P., and Piepersberg, W. (1998) The genes lmbB1 and lmbB2 of *Streptomyces lincolnensis* encode enzymes involved in the conversion of L-tyrosine to propylproline during the biosynthesis of the antibiotic lincomycin A, *Arch. Microbiol. 169*, 322-332.

28. Needleman, S. B., and Wunsch, C. D. (1970) A general method applicable to the search for similarities in the amino acid sequence of two proteins, *J. Mol. Biol. 48*, 443-453.

29. Ullrich, R., and Hofrichter, M. (2007) Enzymatic hydroxylation of aromatic compounds, *Cell. Mol. Life. Sci. 64*, 271-293.

30. Meunier, B., de Visser, S. P., and Shaik, S. (2004) Mechanism of oxidation reactions catalyzed by cytochrome P450 enzymes, *Chem. Rev. 104*, 3947-3980.

31. Ortiz de Montellano, P. R. (2010) Catalytic mechanisms of heme peroxidases, in *Biocatalysis Based on Heme Peroxidases* (Torres, E., and Ayala, M., Eds.), Springer-Verlab, Berlin Heidelberg.

32. Leahy, J. G., Batchelor, P. J., and Morcomb, S. M. (2003) Evolution of the soluble diiron monooxygenases, *FEMS. Microbiol. Rev. 27*, 449-479.

33. Fitzpatrick, P. F. (2003) Mechanism of aromatic amino acid hydroxylation, *Biochemistry 42*, 14083-14091.

34. Rosenzweig, A. C., and Sazinsky, M. H. (2006) Structural insights into dioxygen-activating copper enzymes, *Curr. Opin. Struct. Biol. 16*, 729.

35. Koehntop, K. D., Emerson, J. P., and Que, L. (2005) The 2-His-1-carboxylate facial triad: a versatile platform for dioxygen activation by mononuclear non-heme iron(II) enzymes, *J. Biol. Inorg. Chem. 10*, 87-93.

36. Dordick, J. S., Klibanov, A. M., and Marletta, M. A. (1986) Horseradish peroxidase catalyzed hydroxylations: mechanistic studies, *Biochemistry. 25*, 2946-2951.

37. Halliwell, B. (1977) Generation of hydogen peroxide, superoxide, and hydroxyl radicals during the oxidation of dihydroxyfumaric acid by peroxidase, *Biochem. J. 163*, 441-448.

38. Mossessova, E., and Lima, C. D. (2000) Ulp1-Sumo crystal structure and genetic analysis reveal conserved interactions and a regulatory element essential for cell growth in yeast, *Molecular Cell 5*, 865-876.

39. Woodward, J. J., Martin, N. I., and Marletta, M. A. (2007) An *Escherichia coli* expression-based method for heme substitution, *Nat. Methods. 4*, 43-45.

40. Berry, E. A., and Trumpower, B. L. (1987) Simultaneous determination of hemes *a*, *b*, and *c* from pyridine hemochrome spectra, *Anal. Biochem. 161*, 1-15.

41. Morris, F. (1950) Non-enzymatic oxidation of tyrosine and dopa, *Proc. Natl. Acad. Sci. U.S.A. 36*, 606-611.

42. LaRonde-LeBlanc, N., Resto, M., and Gerratana, B. (2009) Regulation of active site coupling in glutamine-dependent NAD^+ synthetase, *Nature Structural and Molecular Biology 16*, 421-429.

43. Connor, K. L., Colabroy, K. L., and Gerratana, B. (2011) A heme peroxidase with a functional role as an L-tyrosine hydroxylase in the biosynthesis of anthramycin, *Biochemistry. 50*, 8926-8936.

44. Whiteaker, J. R., Fenselau, C. C., Fetterolf, D., Steele, D., and Wilson, D. (2004) Quantitative determination of heme for forensic characterization of *Bacillus* spores using matrix-assisted laser desorption/Ionization time-of-flight mass spectrometry, *Anal. Chem. 76*, 2836-2841.

45. Wang, Y., Gatti, P., Sadilek, M., Scott, C. R., Turecek, F., and Gelb, M. H. (2008) Direct assay of enzymes in heme biosynthesis for the detection of porphyrias by tandem mass spectrometry. Uroporphyrinogen decarboxylase and coproporphyrinogen III oxidase, *Anal. Chem. 80*, 2599-2605.

46. Falk, J. E. (1964) Porphyrins and metalloporphyrins, p 236, Elsevier, Amsterdam.

47. Hargrove, M. S., Barrick, D., and Olson, J. S. (1996) The association rate constant for heme binding to globin is independent of protein structure *Biochemistry. 35*, 11293-11299.

48. Gattoni, M., Boffi, A., Sarti, P., and Chiancone, E. (1996) Stability of the heme-globin linkage in ab dimers and isolated chains of human hemoglobin. A study of the heme transfer reaction from the immobilized proteins to albumin., *J. Biol. Chem. 271*, 10130-10136.

49. Bhakta, M. N., and Wilks, A. (2006) The mechanism of heme transfer from the cytoplasmic heme binding protein PhuS to the δ-regioselective heme oxygenase of *Pseudomonas aeruginosa Biochemistry. 45*, 11642-11649.

50. Dailey, H. A. (1985) Spectroscopic examination of the active site of bovine ferrochelatase, *Biochemistry. 24*, 1287-1291.

51. Mulrooney, S. B., and Waskell, L. (2000) High-level expression in *Escherichia coli* and purification of the membrane-bound form of cytochrome b5, *Prot. Expr. Pur. 19*, 173-178.

52. Suits, M. D. L., Jaffer, N., and Jia, Z. (2006) Structure of the *Escherichia coli* O157:H7 heme oxygenase ChuS in complex with heme and enzymatic inactivation by mutation of the heme coordinating residue His-193, *J. Biol. Chem. 281*, 36776-36782.

53. Dalton, D. A., del Castillo, L. D., Kahn, M. L., Joyner, S. L., and Chatfield, J. M. (1996) Heterologous expression and characterization of soybean cytosolic ascorbate peroxidase, *Arch. Biochem. Biophys. 328*, 1-8.

54. Kimoto, H., Matsuyama, H., Yumoto, I., and Yoshimune, K. (2008) Heme content of recombinant catalase from *Psychrobacter* sp. T-3 altered by host *Escherichia coli* cell growth conditions, *Prot. Expr. Pur. 59*, 357-359.

55. Li, J. M., Umanoff, H., Proenca, R., Russell, C. S., and Cosloy, S. D. (1988) Cloning of the *Escherichia coli* K-12 *hemB* gene, *J. Bacteriol. 170*, 1021-1025.

56. Winter, M. B., McLaurin, E. J., Reece, S. Y., Olea, C., Nocera, D. G., and Marletta, M. A. (2010) Ru-porphyrin protein scaffolds for sensing O_2, *J. Am. Chem. Soc. 132*, 5582-5583.

57. Angerer, A., and Braun, V. (1998) Iron regulates transcription of the *Escherichia coli* ferric citrate transport genes directly and through the transcription initiation proteins, *Arch. Microbiol. 169*, 483-490.

58. Mogharrab, N., Ghourchian, H., and Amininasab, M. (2007) Structural stabilization and functional improvement of horseradish peroxidase upon modification of accessible lysines: Experiments and simulation, *Biophys. J. 92*, 1192-1203.

59. Ortiz de Montellano, P. R. (2005) *Cytochrome P450 - Structure, Mechanism, and Biochemistry*, 3rd ed., Kluwer Academic/Plenum Publishers, New York.

60. Bernhardt, R. (2006) Cytochromes P450 as versatile biocatalysts, *Journal of Biotechnology 124*, 128-145.

61. Groves, J. T. (2006) High-valent iron in chemical and biological oxidations, *J. Inorg. Biochem. 100*, 434-447.

62. Rittle, J., and Green, M. T. (2010) Cytochrome P450 Compound I: Capture, characterization, and C-H bond activation kinetics, *Science 330*, 933-937.

63. Wang, Y., Hirao, H., Chen, H., Onaka, H., Nagano, S., and Shaik, S. (2008) Electron transfer activation of chromopyrrolic acid by cytochrome P450 en route to the formation of an antitumor indolocarbazole derivative: Theory supports experiment, *J. Am. Chem. Soc. 130*, 7170-7171.

64. Groves, J. T. (2003) The bioinorganic chemistry of iron in oxygenases and supramolecular assemblies, *Proc. Natl. Acad. Sci. U.S.A. 100*, 3569-3574.

65. Dunford, H. B. (1999) *Heme Peroxidases*, John Wiley & Sons, Inc., New York.

66. Bairoch, A. (2000) The ENZYME database in 2000, *Nucleic Acids Research 28*, 304-305.

67. Poulos, T. L. (2010) Thirty years of heme peroxidase structural biology, *Arch. Biochem. Biophys. 500*, 3-12.

68. Olsovská, J., Novotná, J., Flieger, M., and Spízek, J. (2007) Assay of tyrosine hydroxylase based on high-performance liquid chromatography separation and quantification of L-dopa and L-tyrosine, *Biomed. Chromatogr. 21*, 1252-1258.

69. Edelhoch, H. (1962) The properties of thyroglobulin, *J. Biol. Chem. 237*, 2778-2787.

70. *The Merck Index*, 13th ed., Entry# 5485.

71. Hiner, A. N., Rodriguez-Lopez, J. N., Arnao, M. B., Lloyd Raven, E., Garcia-Canovas, F., and Acosta, M. (2000) Kinetic study of the inactivation of ascorbate peroxidase by hydrogen peroxide, *Biochem. J. 348*, 321-328.

72. Arnow, L. E. (1937) Colormetric determination of the components of 3,4-dihydroxyphenylalanine-tyrosine mixtures, *J. Biol. Chem. 118*, 531-537.

73. Fitzpatrick, P. F. (1991) Steady-state kinetic mechanism of rat tyrosine hydroxylase, *Biochemistry 30*, 3658-3662.

74. Garcia-Arellano, H. (2010) A compendium of bio-physical-chemical properties of peroxidases, in *Biocatalysis Based on Heme Peroxidases* (Torres, E., and Ayala, M., Eds.), Springer-Verlab, Berlin Heidelberg.

75. Valderrama, B. (2010) Deactivation of hemeperoxidases by hydrogen peroxide: Focus on Compound III, in *Biocatalysis Based on Heme Peroxidases* (Torres, E., and Ayala, M., Eds.), Springer-Verlab, Berlin Heidelberg.

76. Feducia, J., Dumarieh, R., Gilvey, L. B., Smirnova, T., Franzen, S., and Ghiladi, R. A. (2009) Characterization of dehaloperoxidase Compound ES and its reactivity with trihalophenols, *Biochemistry. 48*, 995-1005.

77. Ayala, M., Batista, C., and Vazquez-Duhalt, R. (2011) Heme destruction, the main molecular event during the peroxide-mediated inactivation of chloroperoxidase from *Caldariomyces fumago*, *J. Biol. Inorg. Chem. 16*, 63-68.

78. Belyea, J., Gilvey, L. B., Davis, M. F., Godek, M., Sit, T. L., Lommel, S. A., and Franzen, S. (2005) Enzyme function of the globin dehaloperoxidase from

Amphitrite ornata is activated by substrate binding *Biochemistry. 44*, 15637-15644.

79. Osborne, R. L., Coggins, M. K., Raner, G. M., Walla, M., and Dawson, J. H. (2009) The mechanism of oxidative halophenol dehalogenation by *Amphitrite ornata* dehaloperoxidase is initiated by H_2O_2 binding and involves two consecutive one-electron steps: Role of ferryl intermediates, *Biochemistry. 48*, 4231-4238.

80. Ayala, M. (2010) Redox potential of peroxidases, in *Biocatalysis Based on Heme Peroxidases* (Torres, E., and Ayala, M., Eds.), Springer-Verlab, Berlin Heidelberg.

81. Pearson, R. (1963) Hard and soft acids and bases, *J. Am. Chem. Soc. 120*, 13383-13388.

82. Evans, J. J. (1970) Spectral similarities and kinetic differences of two tomato plant peroxidase isoenzymes, *Plant. Physiol. 45*, 66-69.

83. Roberts, J. N., Singh, R., Grigg, J. C., Murphy, M. E. P., Bugg, T. D. H., and Eltis, L. D. (2011) Characterization of dye-decolorizing peroxidases from *Rhodococcus jostii* RHA1, *Biochemistry. 50*, 5108-5119.

84. Dunford, H. B. (1999) Spectroscopy of horseradish peroxidase. II: Nuclear magnetic resonance, electron paramagnetic resonance, electron nuclear double resonance, mossbauer spectroscopy, and theoretical studies, in *Heme Peroxidases*, pp 92-95, John Wiley & Sons, Inc., New York.

85. Passardi, F., Theiler, G., Zamocky, M., Cosio, C., Rouhier, N., Teixera, F., Margis-Pinheiro, M., Ioannidis, V., Penel, C., Falquet, L., and Dunand, C. (2007) PeroxiBase: The peroxidase database, *Phytochem. 68*, 1605-1611.

86. Kunishima, N., Fukuyama, K., Wakabayashi, S., Sumida, M., Takaya, M., Shibano, Y., Amachi, T., and Matsubara, H. (1993) Crystallization and preliminary X-ray diffraction studies of peroxidase from a fungus *Arthromyces ramosus*, *Proteins: Struct. Funct. Bioinf. 15*, 216-220.

87. Patterson, W. R., and Poulos, T. L. (1995) Crystal structure of recombinant pea cytosolic ascorbate peroxidase, *Biochemistry. 34*, 4331-4341.

88. Gajhede, M., Schuller, D., Henriksen, A., Smith, A. T., and Poulos, T. L. (1997) Crystal structure of horseradish peroxidase c at 2.15 A resolution, *Nat. Struct. Biol. 4*, 1032-1038.

89. Zámocký, M., Furtmüller, P. G., and Obinger, C. (2010) Evolution of structure and function of Class I peroxidases, *Arch. Biochem. Biophys. 500*, 45-57.

90. Fidy, J., Paul, K. G., and Vanderkooi, J. M. (1989) Differences in the binding of aromatic substrates to horseradish peroxidase revealed by fluorescence line narrowing, *Biochemistry. 28*, 7531-7541.

91. Beckett, D., Johnson, M. L., Holt, J. M., and Ackers, G. K. (2011) Chapter one - Measurement and analysis of equilibrium binding titrations: A beginner's guide, in *Methods in Enzymology*, pp 1-16, Academic Press.

92. Gill, G., Richter-Rusli, A. A., Ghosh, M., Burrows, C. J., and Rokita, S. E. (1997) Nickel-dependent oxidative cross-linking of a protein, *Chem. Res. Toxicol. 10*, 302-309.

93. Gill, G. (1993) Protein and nucleic acid modification and nickel salts, in *Department of Chemistry*, Stony Brook University.

94. Hazen, S. L., Hsu, F. F., and Heinecke, J. W. (1996) *p*-Hydroxyphenylacetaldehyde is the major product of L-tyrosine oxidation by activated human phagocytes, *J. Biol. Chem. 271*, 1861-1867.

95. Marquez, L. A., and Dunford, H. B. (1995) Kinetics of oxidation of tyrosine and dityrosine by myeloperoxidase compounds I and II, *J. Biol. Chem. 270*, 30434-30440.

96. Manna, S. K., and Mazumdar, S. (2008) Reversible inactivation of cytochrome P450 by alkaline earth metal ions: Auxiliary metal ion induced conformation change and formation of inactive P420 species in CYP101, *J. Inorg. Biochem. 102*, 1312-1321.

97. Mouro, C., Jung, C., Bondon, A., and Simonneaux, G. (1997) Comparative Fourier transform infrared studies of the secondary structure and the CO heme ligand environment in cytochrome P-450cam and cytochrome P-420cam *Biochemistry. 36*, 8125-8134.

98. O'Keefe, D. H., Ebel, R. E., Peterson, J. A., Maxwell, J. C., and Caughey, W. S. (1978) An infrared spectroscopic study of carbon monoxide bonding to ferrous cytochrome P-450, *Biochemistry. 17*, 5845-5852.

99. Martinis, S. A., Blanke, S. R., Hager, L. P., Sligar, S. G., Hui Bon Hoa, G., Rux, J. J., and Dawson, J. H. (1996) Probing the heme iron coordination structure of pressure-induced cytochrome P420cam, *Biochemistry. 35*, 14530-14536.

100. Imai, Y., and Sato, R. (1967) Conversion of P-450 to P-420 by neutral salts and some other reagents, *Eur. J. Biochem. 1*, 419-426.

101. Malencik, D. A., Sprouse, J. F., Swanson, C. A., and Anderson, S. R. (1996) Dityrosine: Preparation, isolation, and analysis, *Anal. Biochem. 242*, 202-213.

102. Thompson, M. K., Franzen, S., Ghiladi, R. A., Reeder, B. J., and Svistunenko, D. A. (2010) Compound ES of Dehaloperoxidase Decays via Two Alternative Pathways Depending on the Conformation of the Distal Histidine, *J. Am. Chem. Soc. 132*, 17501-17510.

103. Hiner, A. N., Raven, E. L., Thorneley, R. N., Garcia-Canovas, F., and Rodriguez-Lopez, J. N. (2002) Mechanisms of compound I formation in heme peroxidases, *J. Inorg. Biochem. 91*, 27-34.

104. Gumiero, A., Murphy, E., Metcalfe, C. L., Moody, P., and Raven, E. L. (2010) An analysis of substrate binding interactions in the heme peroxidase enzymes: A structural perspective, *Arch. Biochem. Biophys. 500*, 13-20.

105. Casella, L., Gullotti, M., Selvaggini, C., Poli, S., Beringhelli, T., and Marchesini, A. (1994) The chloroperoxidase-catalyzed oxidation of phenols. Mechanism, selectivity, and characterization of enzyme-substrate complexes, *Biochemistry. 33*, 6377-6386.

106. Heinecke, J. W., Li, W., Daehnke, H. L., and Goldstein, J. A. (1993) Dityrosine, a specific marker of oxidation, is synthesized by the myeloperoxidase-hydrogen peroxide system of human neutrophils and macrophages, *J. Biol. Chem. 268*, 4069-4077.

107. Matsunaga, I., Sumimoto, T., Ayata, M., and Ogura, H. (2002) Functional modulation of a peroxygenase cytochrome P450: novel insight into the mechanisms of peroxygenase and peroxidase enzymes, *FEBS Letters 528*, 90-94.

108. Kluge, M., Ullrich, R., Dolge, C., Scheibner, K., and Hofrichter, M. (2009) Hydroxylation of naphthalene by aromatic peroxygenase from *Agrocybe aegerita* proceeds via oxygen transfer from H_2O_2 and intermediary epoxidation, *Appl. Microbiol. Biotechnol. 81*, 1071-1076.

109. de Visser, S. P., and Shaik, S. (2003) A proton-shuttle mechanism mediated by the porphyrin in benzene hydroxylation by cytochrome P450 enzymes, *J. Am. Chem. Soc. 125*, 7413-7424.

110. Tang, M.-C., Fu, C.-Y., and Tang, G.-L. (2012) Characterization of SfmD as a heme peroxidase that catalyzes the regioselective hydroxylation of 3-methyltyrosine to 3-hydroxy-5-methyltyrosine in saframycin A biosynthesis, *J. Biol. Chem. 287*, 5112-5121.